INTERNATIONAL SCIENTIFIC JOURNAL

"MATERIAL SCIENCE"

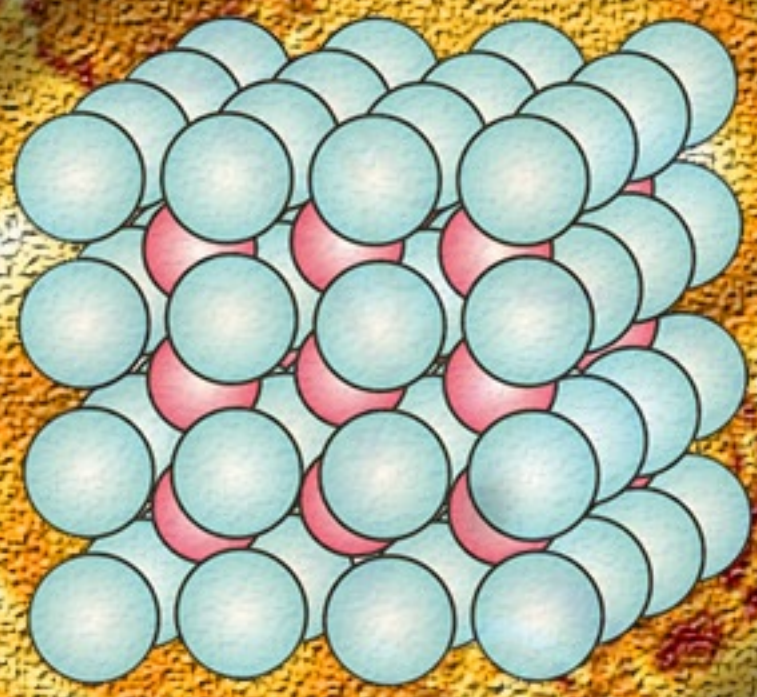

„NONEQUILIBRIUM PHASE TRANSFORMATIONS"

YEAR XII, ISSUE 1/2026

ISSN PRINT 2367-749X
ISSN WEB 2534-8477

PUBLISHER: SCIENTICIC TECHNICAL UNION OF MECHANICAL ENGINEERING INDUSTRY 4.0

108 Rakovski str., 1000 Sofia, Bulgaria
tel./fax (+359 2) 986 22 40, tel. (+359 2) 987 72 90,
office@stumejournals.com, www.stumejournals.com

INTERNATIONAL SCIENTIFIC JOURNAL

MATERIALS SCIENCE. NON-EQUILIBRIUM PHASE TRANSFORMATIONS

PUBLISHER:

SCIENTIFIC TECHNICAL UNION OF MECHANICAL ENGINEERING "INDUSTRY 4.0"

108, Rakovski Str., 1000 Sofia, Bulgaria
tel. (+359 2) 987 72 90,
tel./fax (+359 2) 986 22 40,
office@stumejournals.com
www.stumejournals.com

YEAR XII, ISSUE 1/2026
PRINT ISSN: 2367-749X
ONLINE ISSN: 2534-8477

All articles are published after peer review by two independent reviewers.

CHIEF EDITOR

Prof. Tsanka Dikova, Bulgaria

DEPUTY EDITOR IN CHIEF

Prof. Anna Dobrzańska-Danikiewicz, Poland
Prof. Rasa Kandrotaite Janutiene, Lithuania
Prof. Satoru Iwamori, Japan

MEMBERS:

Prof. Adel Mahmud, Iraq
Prof. Angel Anchev, Bulgaria
Prof. Gennagiy Bagluk, Ukraine
Prof. Dipten Misra, India
Prof. Eugeniy Grigoriev, Russia
Prof. Ibrahim E. Saklakoglu, Turkey
Prof. Irina Charnyak, Belarus
Dr. Lech B. Dobrzanski, Poland
Prof. Leszek Dobrzanski, Poland,
Prof. Maria Nikolova, Bulgaria
Prof. Masaki Hashida, Japan
Prof. Neli Mintcheva, Bulgaria
Prof. Nikolay Dolgov, Ukraine
Prof. Ruslan Kusin, Belarus
Prof. Sergei Kulinich, Japan
Prof. Sergey Dobatkin, Russia
Prof. Sergey Nikulin, Russia
Prof. Sonya Vachinska, Bulgaria
Prof. Svetlana Gubenko, Ukraine
Prof. Sveto Cvetkovski, North Macedonia
Prof. Souren Mitra, India
PhD Tomasz Matula, Poland
Prof. Vladimir Dunchev, Bulgaria
Prof. Vladimir Todorov, Bulgaria

C O N T E N T S

Artificial intelligence-assisted WDM multiplexing in multicore plastic optical fibers
Dror Malka 3

Deepening oxidation of metal crystals by laser radiation
Arturs Medvids, Yuliy Bludov, Sergiy Lavrys, Iuriy Nasieka, Aleksands Michko, Volodymir Lozinskii 13

Application potential of lubricants for bearings and gears in space mechanisms – analysis of properties and limitations
Leszek Pawlicki 15

Modern methods of manufacturing long tubular porous powder filter elements
Aliaksandr Ilyushchanka, Iryna Charniak, Aleksej Kusin, Anastasia Astapenka, Margaruta Kuntsevich, Ruslan Kusin 18

Surface treatment of copper using a plasma from a helicon source
E. Rudenko, I. Korotash, A. Novytska, D. Polotskiy, M. Dyakin 21

Influence of laser processing on the development peculiarities of cracks arising in the steels near non-metallic inclusions
Svetlana Gubenko 24

Complex-composition ceramics based on zirconium oxide for creating the latest thermal barrier coatings
Alina Makudera, Olena Dudnik, Serhii Lakyza 28

Nanostructuring of brass surface by helicon source plasma
E. Rudenko, I. Korotash, D. Polotskiy, A. Rudenko, V. Dekhtyarenko, M. Dyakin 30

Ultrafast bond softening and non-thermal phase dynamics in femtosecond-excited diamond
Tzveta Apostolova 33

Influence of microstructural modification of cement-based composites on transport processes and long-term reliability
Veis Šerifi, Nazim Manić, Emir Maslak, Vesnera Šerifi 39

Hot deformation processing of Ti–Zr–Nb biomedical alloys
Denys Oryshych, Oleksandr Stasiuk, Dmytro Savvakin 44

Effect of refining time on porosity and mechanical preperties of low-ressure casting made of ALSI7MG alloy
Jaroslaw Piatkowski, Tomasz Matula, Marco A. Reyna 47

Artificial intelligence-assisted WDM multiplexing in multicore plastic optical fibers

Dror Malka*
Faculty of Engineering, Holon Institute of Technology (HIT), Holon 5810201, Israel
*Corresponding author: drorm@hit.ac.il

ABSTRACT: *This work presents an artificial-intelligence-assisted design methodology for wavelength-division multiplexing (WDM) in multicore plastic optical fibers (MC-POFs) operating in the green visible spectrum. The device is based on polycarbonate (PC) guiding cores embedded in a CYTOP background and uses controlled inter-core coupling to combine four wavelength channels at 500, 520, 540, and 560 nm into one output core. The electromagnetic response is evaluated with the beam-propagation method (BPM) in RSoft Photonics CAD, while an external AI-assisted optimization layer is used to rank candidate geometries, refine the switching length, and search the coupled parameter space defined by the air-hole diameter, lattice pitch, inter-core gap, and channel separation. The physical simulator remains the source of the optical field solution; the AI layer is used as an optimization and decision-support mechanism rather than as a replacement for Maxwell-based propagation modeling. The optimized structure has a total active length of 20 mm, a pitch of 549.8 nm, an air-hole diameter of 241.6 nm, an inter-core gap of 1.099 µm, and a normalized diameter-to-pitch ratio of 0.4395. Simulated transmission reaches 88%, 91%, 95%, and 97% for the four channels, corresponding to insertion losses between 0.55 and 0.13 dB. The wavelength-dependent coupling lengths decrease from 395.33 µm at 500 nm to 153.52 µm at 560 nm, allowing a common switching-length condition to be approached with near-integer coupling ratios. Thermal drift analysis indicates stable operation for a worst-case ±3 nm wavelength displacement. A two-channel experimental demonstration at 500 and 540 nm provides additional support for the spatial multiplexing concept. The resulting platform combines compact WDM routing with AI-assisted photonic optimization and offers a pathway toward low-complexity visible-light links, sensing networks, and photonic neural interconnects.*

KEYWORDS: *ARTIFICIAL INTELLIGENCE; MACHINE LEARNING; WDM; MULTICORE PLASTIC OPTICAL FIBER; POLYCARBONATE; RSOFT; BPM; VISIBLE-LIGHT COMMUNICATION; PHOTONIC OPTIMIZATION.*

1. INTRODUCTION

Polymer optical fibers are attractive for short-range photonic systems because they are lightweight, mechanically flexible, comparatively inexpensive, and compatible with large-core or microstructured geometries. These characteristics are especially useful in visible-light communication, sensing, automotive networks, robotic platforms, and compact instrumentation, where the mechanical requirements can be as important as propagation loss. Multicore plastic optical fibers extend this concept by embedding several guiding regions inside a shared cladding. The resulting structure can support parallel transmission, spatial routing, power exchange between neighboring cores, and wavelength-selective coupling within a single fiber body [1-6]. Unlike conventional free-space multiplexers, an in-fiber device can reduce alignment sensitivity and eliminate part of the connector, grating, and lens overhead normally associated with combining several optical channels.

Wavelength-division multiplexing increases information capacity by assigning separate data streams to different optical wavelengths. In the visible spectrum, a compact WDM unit can support illumination-based communication, distributed sensors, spectroscopy, and multi-source photonic computing. Earlier multicore-fiber and integrated-waveguide studies have demonstrated RGB multiplexers, demultiplexers, MMI devices, and wavelength routers with increasingly compact footprints [7-16]. The challenge is that the coupling length between adjacent cores depends simultaneously on wavelength, refractive-index contrast, geometric separation, and modal overlap. A design that is optimal for one channel is therefore not automatically optimal for a neighboring channel. Searching the complete multidimensional space manually or by independent one-variable sweeps becomes inefficient as the number of wavelength channels and fabrication constraints increases.

Artificial intelligence and machine-learning methods provide a useful optimization layer for this type of photonic design problem. In the present framework, RSoft Photonics CAD and the beam-propagation method generate the electromagnetic response, while AI/ML routines guide parameter selection, surrogate-based screening, and multi-objective ranking. Recent work by Malka and co-authors spans AI-driven photonic optimization, neural-network processing, O-band photonic components, thermo-optic phase control, and machine-learning analysis, illustrating the broader convergence of photonics and data-driven optimization [17-24].

The study focuses on a four-channel green-light multiplexer with channel wavelengths of 500, 520, 540, and 560 nm. The structure contains nine PC coupling regions placed inside a hexagonal microstructured POF. Four separated input channels are progressively transferred through wavelength-dependent coupling paths and merged into a common output core. A single nominal switching length is used for all channels, which simplifies the geometry and improves manufacturability compared with architectures requiring a different interaction length for each wavelength. The selected green band is useful because PC and CYTOP provide suitable refractive-index contrast and because green-spectrum sources are relevant to visible-light links, biomedical sensing, Raman-related systems, and compact optical instrumentation [25-30].

The contribution of this paper is threefold. First, it reformulates the multicore POF multiplexer as an AI-assisted constrained optimization problem in which geometrical variables, coupling ratios, insertion loss, and fabrication tolerances are treated jointly. Second, it preserves the original electromagnetic design logic and experimentally supported numerical performance while presenting the simulation workflow as an RSoft-BPM engine coupled to an external machine-learning optimization layer. Third, it consolidates the discussion around WDM multiplexing, eliminating the separate splitter treatment so that the title, abstract, theory, simulations, experiment, and conclusions describe one consistent device. The resulting manuscript is shorter and more focused while retaining the principal numerical results and the physical interpretation of wavelength-selective coupling.

2. DEVICE ARCHITECTURE AND AI-ASSISTED OPTIMIZATION

2.1 Multicore POF geometry

The proposed device uses a three-dimensional hexagonal lattice in which polycarbonate guiding regions are embedded in a CYTOP background together with air holes that define the microstructured cladding. Four optical inputs are positioned symmetrically and are assigned to 500, 520, 540, and 560 nm. Nine PC regions, denoted PC1-PC9, form the coupling network. The outer input cores transfer optical power toward intermediate PC regions and finally toward PC9, which acts as the common output. The geometry is intentionally symmetric so that the same longitudinal interaction windows can be reused for the wavelength channels. This architecture supports passive routing without external gratings or bulk combining optics and is closely related to previously demonstrated multicore POF and multicore PCF wavelength devices [7-12].

The principal geometric variables are the air-hole diameter d, lattice pitch Λ, inter-core gap, input-channel separation S, and total device length LTotal. The optimized values are d = 241.6 nm, Λ = 549.8 nm, S = 2.198 µm, Gap = 1.099 µm, d/Λ = 0.4395, and LTotal = 20 mm. The refractive indices used in the simulations vary

with wavelength. For the PC core, nPC is 1.599, 1.594, 1.591, and 1.589 at 500, 520, 540, and 560 nm, respectively. The corresponding CYTOP indices are 1.342, 1.341, 1.341, and 1.340. These values create strong confinement in the PC regions while still allowing controlled evanescent overlap between neighboring cores.

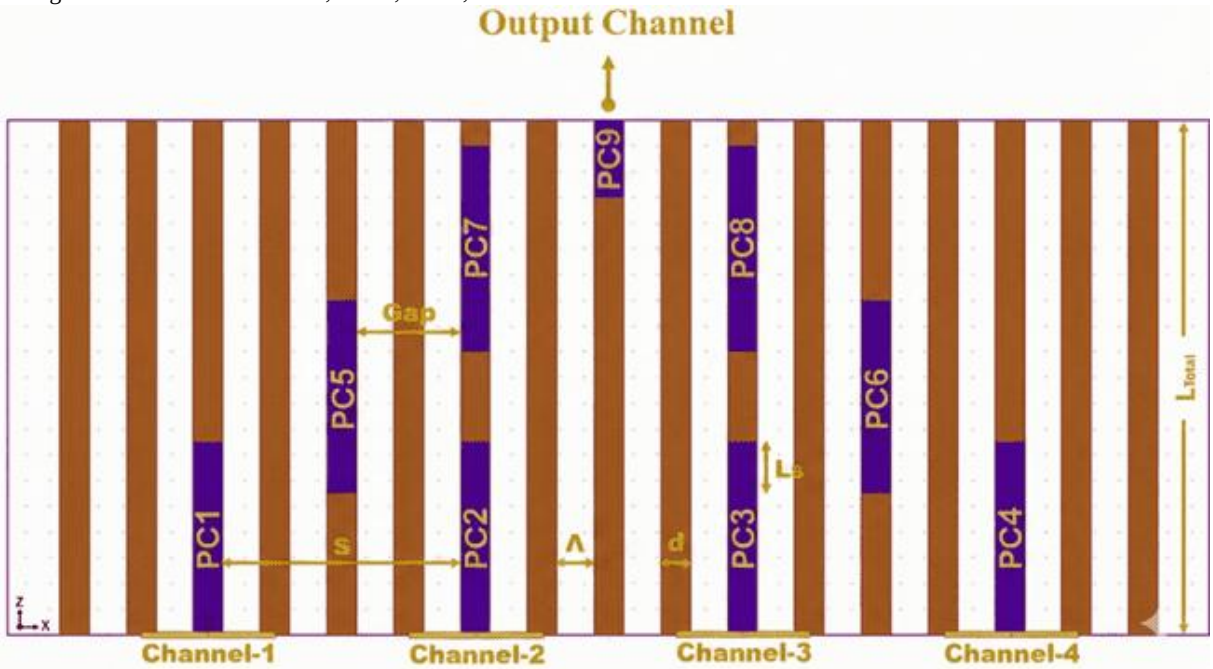

Fig. 1. *Longitudinal cross-sectional architecture of the four-channel PC-MC-POF WDM multiplexer, showing four input channels, intermediate PC coupling regions, and the common output channel.*

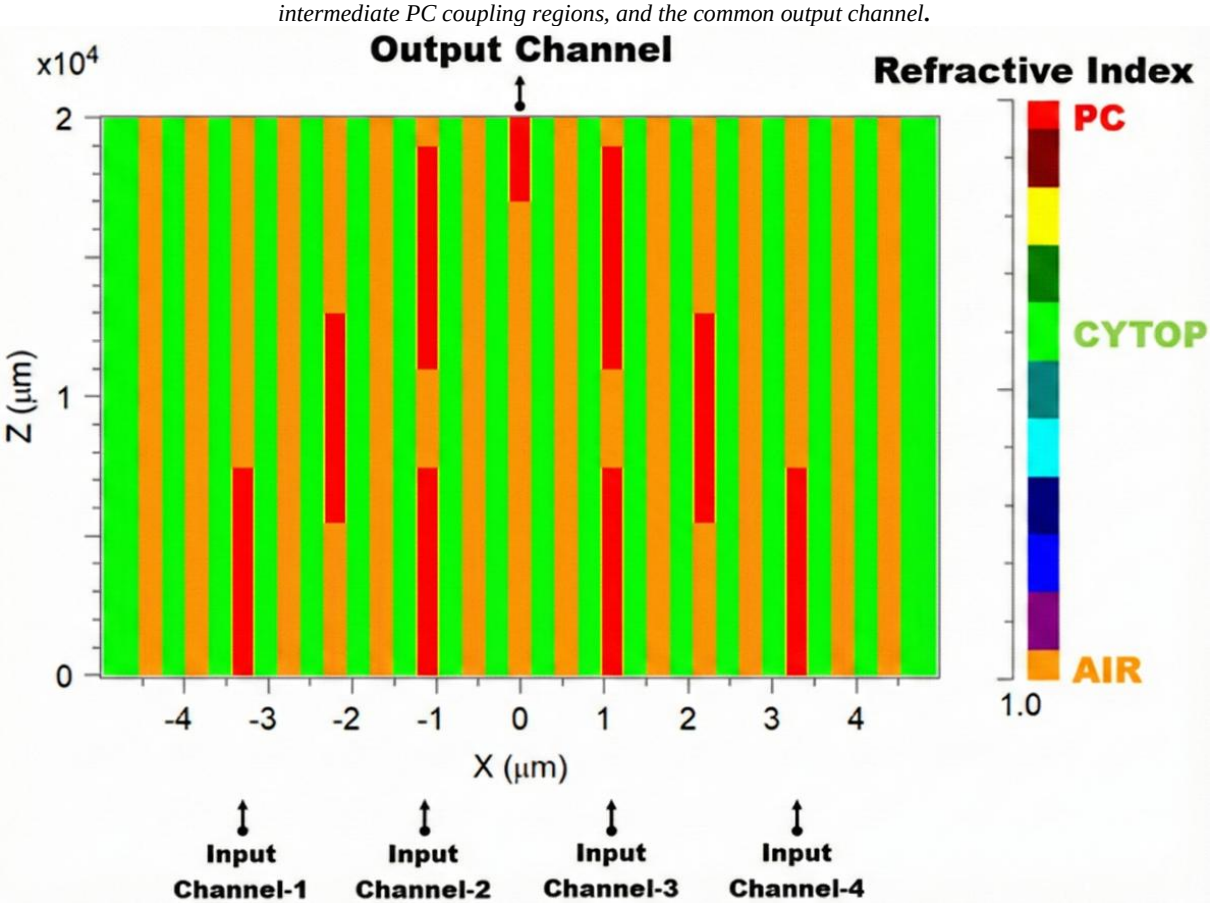

Fig. 2. *Refractive-index distribution in the longitudinal x-z plane for the multicore POF multiplexer.*

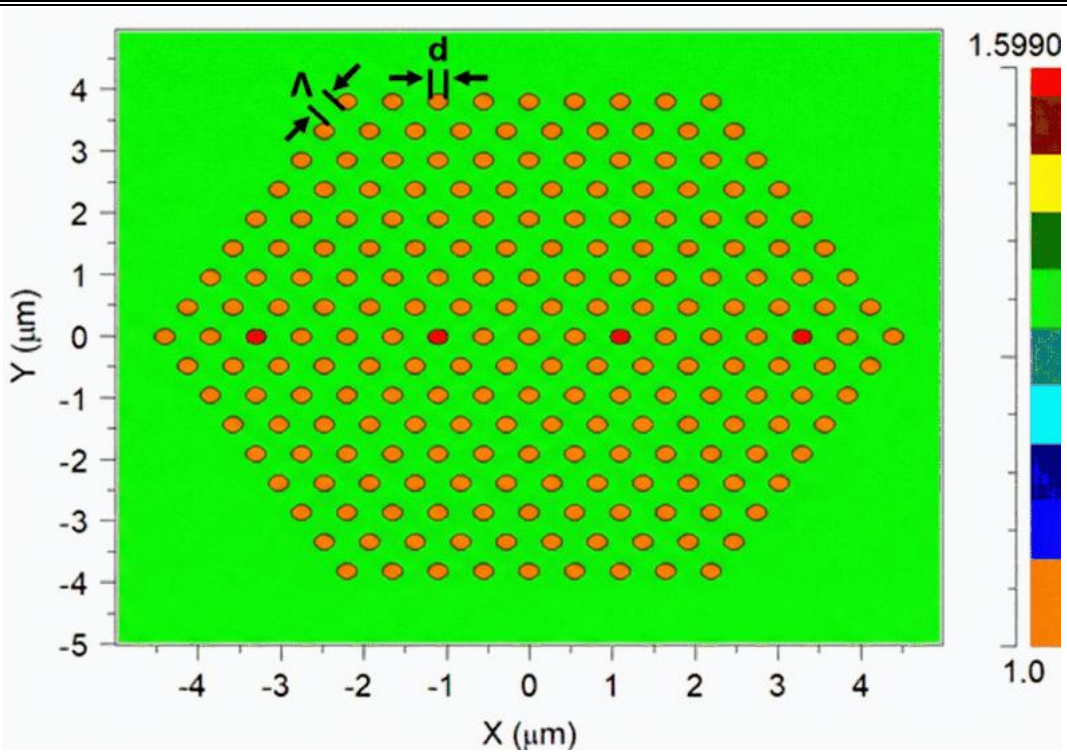

Fig. 3. Input *cross-section of the PC-MC-POF showing the hexagonal air-hole lattice and PC guiding regions.*

2.2 Coupling model and switching-length condition

The multiplexer is evaluated with the same mathematical definitions used in the original manuscript. The equations below are retained exactly in their original Word equation format; only the surrounding discussion is adapted to the AI-assisted RSoft optimization workflow.

The insertion loss (IL) is defined as:

$$IL = -10\mathrm{Log}\left(\frac{P_{out}}{P_{in}}\right) \quad (1)$$

where Pout and Pin are the output and input optical powers, respectively. The coupling length between adjacent PC cores is:

$$L^{\lambda}_{Coupling} = \frac{\pi}{k_0\left(n_{symmetric}\left(d,\Lambda,\lambda,Gap\right) - n_{anti-symmertric}\left(d,\Lambda,\lambda,Gap\right)\right)} \quad (2)$$

For simultaneous multiplexing of all four wavelengths, the switching length is constrained by the same integer-compatibility relation used in the original paper:

$$L_S \approx P_1 L^{\lambda_1}_{Coupling} \approx P_2 L^{\lambda_2}_{Coupling} \approx P_3 L^{\lambda_3}_{Coupling} \approx P_4 L^{\lambda_4}_{Coupling} \quad (3)$$

The corresponding Ratio Value used to evaluate near-integer compatibility is retained as:

$$\text{Ratio Value } (\lambda_{1-4}) = \frac{L_S}{L^{\lambda_{1-4}}_{Coupling}} \quad (4)$$

In the AI-assisted workflow, these equations are not modified by machine learning. RSoft BPM remains the physics solver, while the AI/ML layer searches the permitted geometry space and ranks candidate designs using the original coupling, switching-length, insertion-loss, and Ratio-Value definitions.

Insertion loss, coupling-ratio error, normalized output power, and fabrication tolerance are evaluated directly from the RSoft BPM results using the unchanged definitions above. The AI-assisted layer uses these physics-based outputs only to compare and rank candidate geometries; it does not alter the governing equations or replace the BPM electromagnetic solver.

2.3 AI-assisted RSoft workflow

The computational workflow is organized as a closed design loop between an AI or machine-learning optimizer and RSoft Photonics CAD. The optimizer proposes a candidate set of geometric variables within fabrication-feasible bounds. RSoft then constructs the multicore POF model and executes BPM propagation at the four wavelengths. Output quantities include modal confinement, coupling length, normalized power transfer, output transmission, and insertion loss. These quantities are returned to the optimization layer, which updates the candidate ranking and proposes the next geometry. The process continues until the objective improvement becomes small or the simulation budget is reached. This architecture is compatible with Bayesian optimization, Gaussian-process surrogate models, tree-based regressors, neural-network surrogates, or evolutionary search, but the electromagnetic results remain directly traceable to RSoft simulations.

For reproducibility, the AI stage should be viewed as an accelerator of the parameter search rather than as a substitute for optical physics. Candidate designs that are predicted by a surrogate model are re-evaluated in RSoft before being accepted. The use of a physics-in-the-loop strategy is particularly important in multicore fibers because small geometric changes can alter modal overlap nonlinearly. The final parameters reported in this paper therefore correspond to BPM-validated solutions. The AI layer is most valuable when it identifies interactions between d, Λ, Gap, and LS that would be difficult to detect through isolated sweeps. It also naturally supports robustness analysis by evaluating the local neighborhood of the optimum and rejecting solutions that depend on unrealistically narrow dimensions.

The same workflow can be extended to include thermal uncertainty, source wavelength drift, manufacturing tolerances, and application-specific channel weights. For example, if a photonic-computing application requires unequal optical weights, the target output powers can be modified in the loss function instead of forcing equal channel transfer. In that case the multicore coupler acts as a wavelength-selective passive summation element, connecting WDM routing with in-fiber neuromorphic concepts previously studied in multicore optical networks [17-20].

3. SIMULATION RESULTS

3.1 Modal confinement and wavelength-dependent coupling

RSoft BPM simulations were performed for the four operating wavelengths using the optimized PC-MC-POF geometry. The fundamental transverse-electric input modes remain strongly localized in the selected PC cores, confirming that the refractive-index contrast is sufficient to support controlled launch conditions

across the green band. The mode centroids shift according to the selected input location, while the overall confinement remains similar. These launch fields are used consistently in the coupling and full-device simulations so that differences in channel behavior are dominated by wavelength-dependent coupling rather than inconsistent source profiles.

The coupling analysis confirms a monotonic reduction in coupling length as wavelength increases. The extracted values are 395.33 μm at 500 nm, 282.21 μm at 520 nm, 201.23 μm at 540 nm, and 153.52 μm at 560 nm. The shorter coupling length at longer wavelengths is consistent with the stronger effective overlap of the guided fields in this geometry. When mapped to the common switching-length criterion, the corresponding ratios are 5.06, 7.08, 9.93, and 13.02. The near-integer values explain why a single longitudinal interaction length can be used for all four channels without a large efficiency penalty. This property is central to the compactness of the device and is one of the quantities emphasized by the AI-assisted objective function.

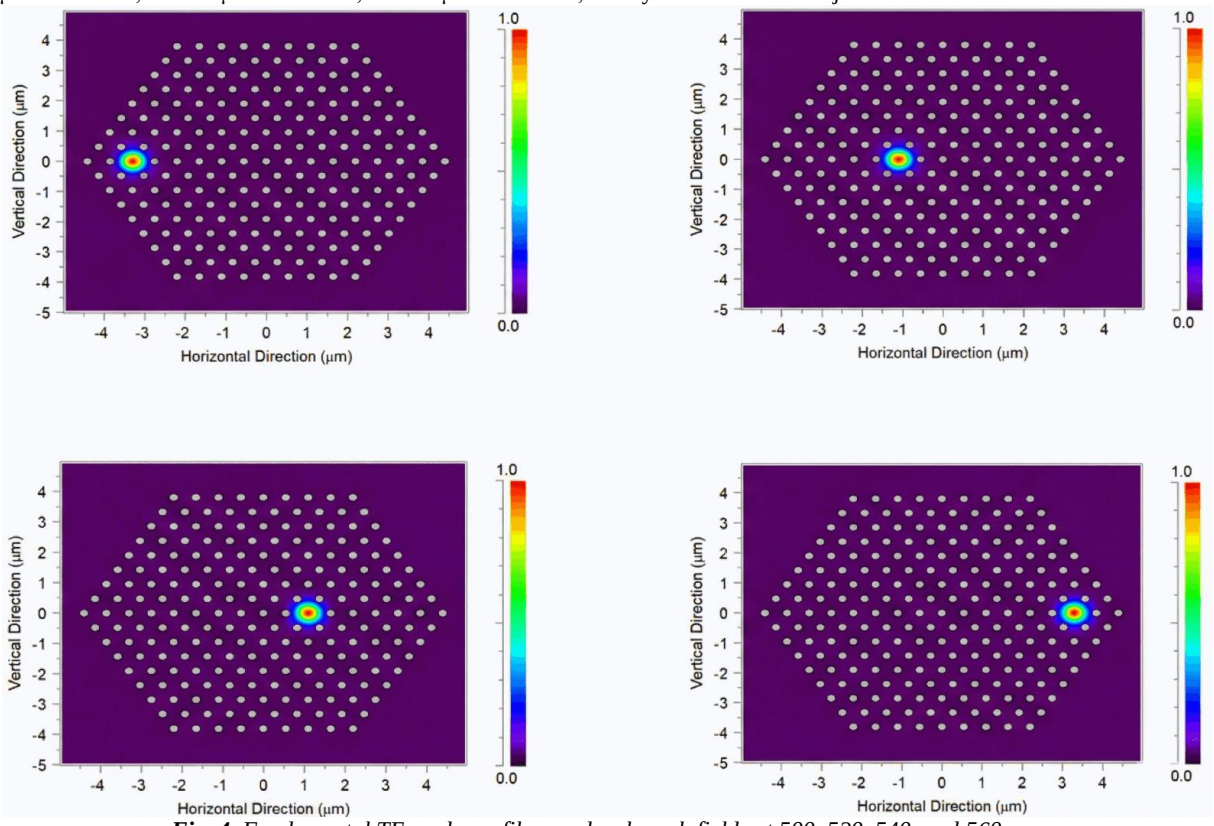

Fig. 4. *Fundamental TE mode profiles used as launch fields at 500, 520, 540, and 560 nm.*

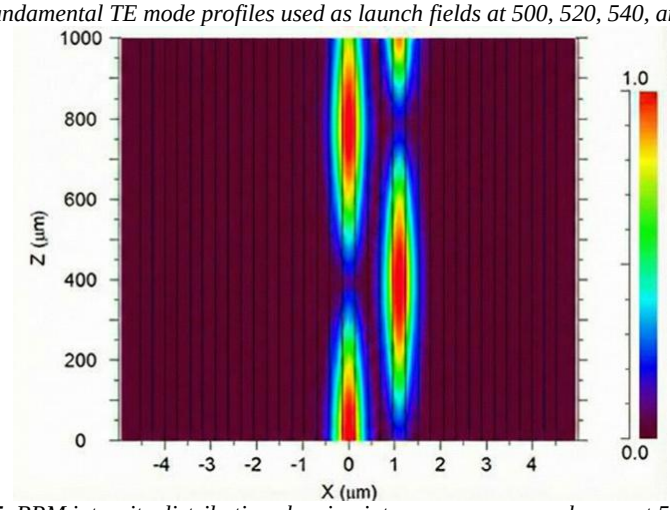

Fig. 5. *BPM intensity distribution showing inter-core energy exchange at 540 nm.*

3.2 Geometric optimization and fabrication tolerance

The diameter-to-pitch ratio d/Λ provides a compact indicator of how strongly the microstructured geometry influences confinement and coupling. Joint optimization of the four channels yields a tolerance interval from approximately 0.4385 to 0.4408 in which the normalized output power remains above 80% for all channels. The global optimum is 0.4395. The important feature is not only the peak response but also the existence of an overlapping four-channel region. An optimum that maximized one channel at the expense of the others would be unsuitable for WDM. The AI-assisted ranking therefore rewards common performance rather than the best single-wavelength value.

The final geometry also balances optical performance against fabrication sensitivity. A modest penalty is assigned to candidate solutions that require extremely narrow tolerances in d, Λ, or Gap. This makes the search more practical because microstructured polymer fibers inevitably exhibit dimensional deviations during preform preparation and drawing. The selected design keeps coupling losses below approximately 2 dB within the reported tolerance window and preserves a useful common operating region. In a production-oriented version of the workflow, measured dimensional statistics from fabricated fibers could be included directly in the optimization loop so that the resulting design maximizes expected performance rather than ideal nominal performance.

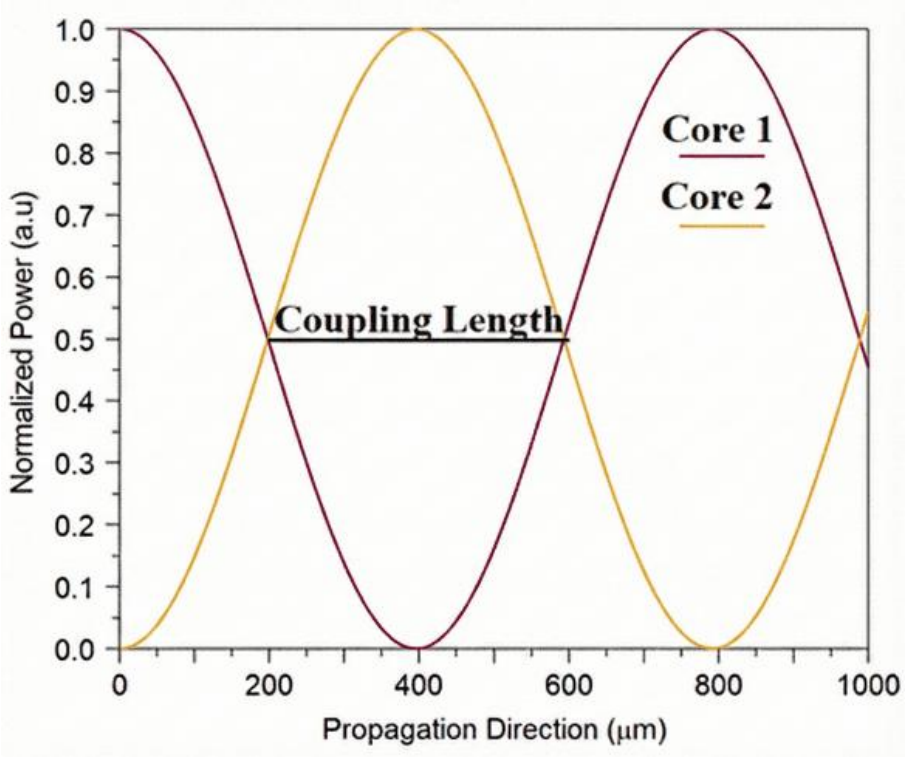

Fig. 6. *Normalized power exchange between two adjacent PC cores at 540 nm; the coupling length is extracted from the first complete transfer.*

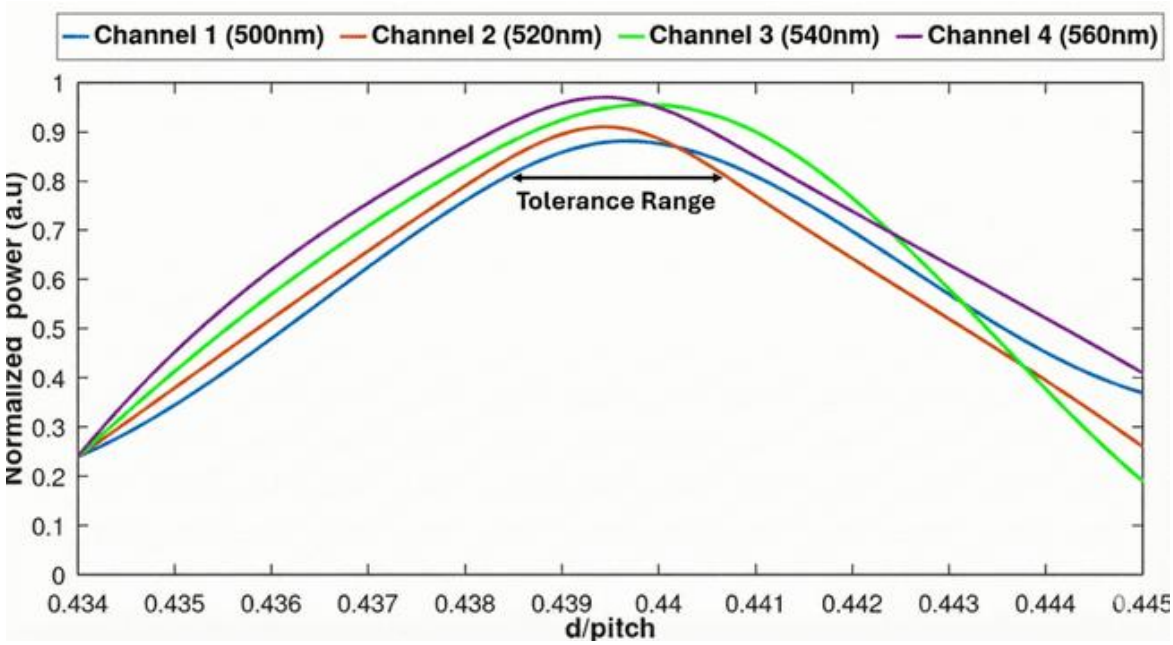

Fig. 7. *Four-channel normalized output power versus d/Λ. The common tolerance region is centered near the optimized value 0.4395.*

3.3 Full-device WDM routing

The complete 20 mm structure was then simulated with each wavelength launched into its assigned input core. The 500 nm channel follows the sequence PC1 to PC5, PC5 to PC7, and PC7 to PC9. The 520 nm channel begins at PC2 and then proceeds through PC5, PC7, and PC9. The 540 nm path uses PC3, PC6, PC8, and PC9, whereas the 560 nm path begins at PC4 and follows PC6, PC8, and PC9. The principal transfer windows occur near z = 5.5-7.5 mm, 11-13 mm, and 17-19 mm. Because the same longitudinal windows serve different wavelength paths, the device retains a symmetric structure and avoids multiple wavelength-specific switching sections.

The propagation maps show that optical energy remains localized around the intended route and converges into the common output core. The process is passive: wavelength selectivity comes from the different coupling lengths and the spatial placement of the PC regions. This is advantageous for visible-light systems because it reduces external alignment requirements. The total active length of 20 mm is sufficiently short for integration while remaining long enough to realize the required sequential transfers. For laboratory handling, a longer physical fiber section can be used outside the active region with only modest additional attenuation.

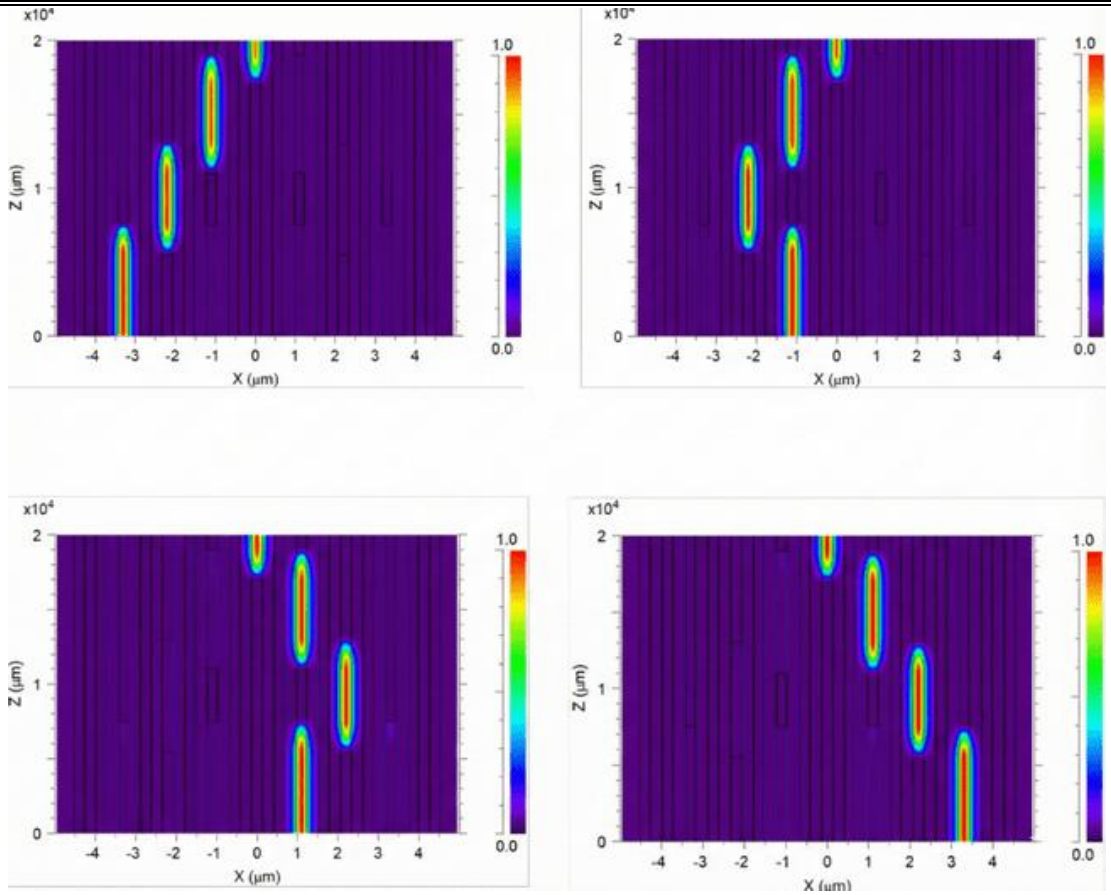

Fig. 8. *Simulated light-intensity trajectories for the four wavelength channels as they couple toward the common output core.*

3.4 Transmission, insertion loss, and thermal robustness

The simulated transmission peaks are 88% at 500 nm, 91% at 520 nm, 95% at 540 nm, and 97% at 560 nm. These values correspond to insertion losses that decrease from approximately 0.55 dB at 500 nm to 0.13 dB at 560 nm. The channel linewidths broaden from roughly 9.2 nm to 13.8 nm over the same wavelength range. The spectra are clearly separated, indicating that the optimized input spacing and coupling geometry provide useful channel isolation. The combined result is a compact WDM multiplexer in which all four channels reach the same spatial output while remaining spectrally distinguishable.

Thermal wavelength drift was evaluated for a temperature excursion from 25°C to 85°C using a representative source sensitivity of 50 pm/°C, corresponding to a worst-case displacement of about ±3 nm. Under this perturbation the additional loss ranges from approximately 0.61 dB at 500 nm to 0.27 dB at 560 nm. The structure therefore retains acceptable performance despite realistic source drift. In the AI-assisted framework, this test can be incorporated directly into the objective function by evaluating every promising geometry at the nominal wavelengths and at shifted wavelengths. Such robust optimization prevents the algorithm from selecting a narrow spectral optimum that would fail under temperature variation.

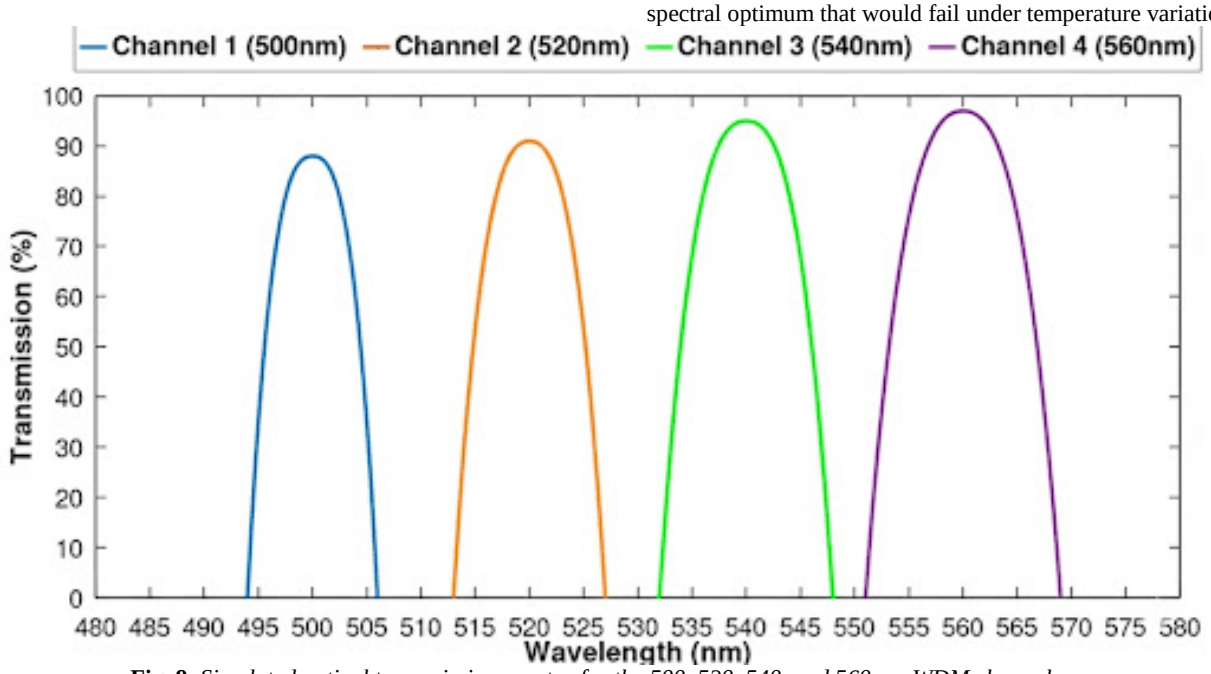

Fig. 9. *Simulated optical transmission spectra for the 500, 520, 540, and 560 nm WDM channels.*

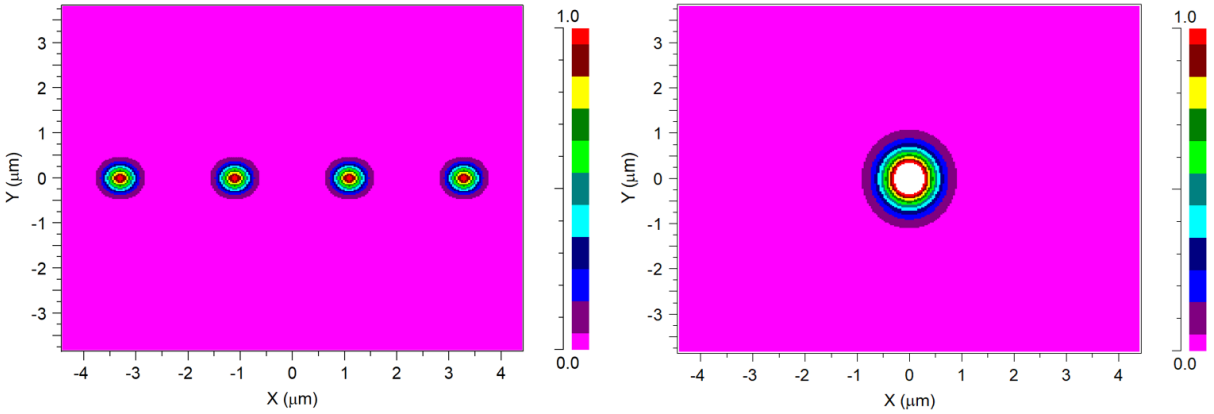

Fig. 10. *Simulated field profiles at the four inputs and the combined field at the central output core, illustrating passive wavelength-weighted optical summation.*

4. EXPERIMENTAL VALIDATION

A two-channel experiment was used to evaluate the underlying spatial multiplexing principle with commercially available multicore polymer fiber. Narrow-linewidth sources near 500 and 540 nm were coupled into separate input cores through aspheric collimating optics and precision positioning stages. A fiber section of approximately 50 mm was used to provide a mechanically convenient experimental length while retaining the required inter-core interaction. At the output, the combined field was imaged with a microscope objective and CMOS camera. The observed far-field distribution exhibits a single dominant Gaussian-like spot with ring structure in the false-color representation, indicating that optical power from the two launched wavelengths converges spatially at the output.

The measured total insertion loss was approximately 2.03 dB for a combined 50 mW input, corresponding to about 31.4 mW at the output. The experimental loss is higher than the idealized four-channel BPM values because the laboratory arrangement includes coupling, alignment, facet, and propagation penalties that are not all represented in the simplified simulation model. Even so, the measurement supports the central physical premise of the architecture: distinct visible wavelengths can be launched into separate cores and spatially merged inside a multicore polymer fiber without external wavelength-combining optics at the output. This validation is also useful for the AI-assisted design strategy because it identifies which simulation outputs should be calibrated against real measurements in future closed-loop optimization.

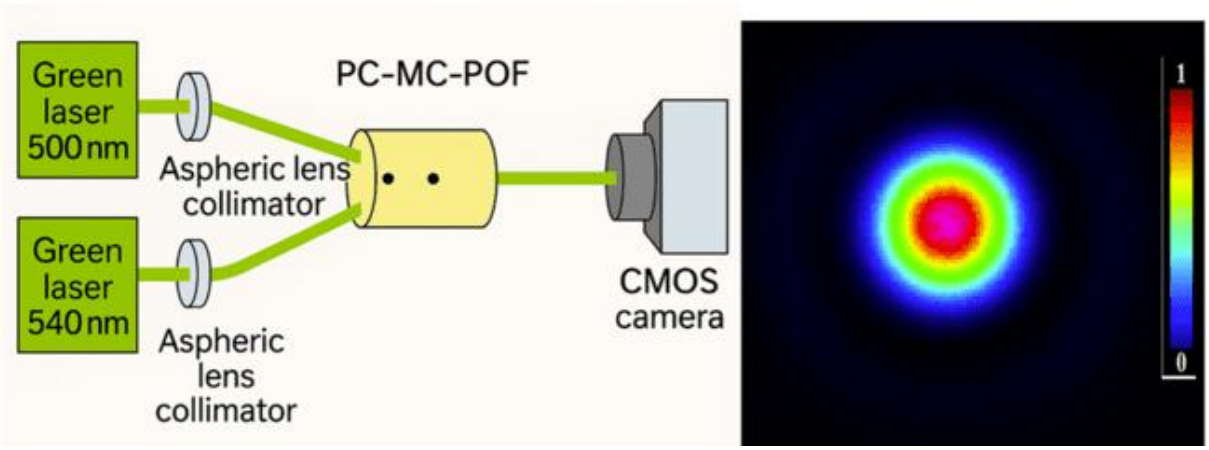

Fig. 11. *Two-channel experimental multiplexing arrangement using 500 and 540 nm green sources and the measured output spot profile.*

5. DISCUSSION

The proposed approach combines three ideas that are usually treated separately: multicore polymer-fiber routing, wavelength-selective coupling, and AI-assisted photonic optimization. The multicore geometry provides the physical platform, the wavelength dependence of the coupling length provides the WDM mechanism, and the AI layer makes it practical to search a design space containing several interacting dimensions. This separation of roles is useful because it avoids overstating the function of machine learning. RSoft BPM remains responsible for the field solution and therefore for the reported coupling, transmission, and loss values. AI contributes by choosing where to evaluate the physics and by recognizing tradeoffs among competing objectives.

The architecture is particularly attractive for visible-light systems in which size, flexibility, and low component count are important. A conventional four-channel combiner can require multiple discrete optics, alignment points, or cascaded waveguide sections. In the PC-MC-POF structure, the wavelength routing is embedded along the fiber axis. The resulting 20 mm interaction region can be packaged as part of a lightweight fiber assembly. Potential applications include short-range WDM links, robotic sensor networks, multicolor biomedical probes, distributed spectroscopy, and compact signal-routing modules. The same coupling concept can also support reverse operation as a demultiplexer if the optical direction and collection geometry are changed, subject to reciprocity and port design. Related integrated-waveguide studies have also demonstrated green/red demultiplexing, angled MMI demultiplexers, and O-band grating coupling, complementing the wavelength-routing functionality considered here [31-33]. Multicore-PCF and MMI-based splitters, combiners, and low-reflection couplers further show that engineered modal coupling can support compact power division and recombination across diverse fiber and waveguide platforms [34-41]. Beyond communications, PCF/POF sensing studies span pathogen and multi-analyte detection, low-index and cancer-cell sensing, refractive-index and liquid-level measurement, and space-division fiber splitting, illustrating the breadth of structured-fiber functionality [42-49]. Related PCF research on dispersion-engineered fiber lasers and wavelength-tunable parametric amplification also highlights the importance of wavelength-dependent modal control in advanced fiber systems [50-51]. Fabrication and application studies on polymer splitters,

polycarbonate/ITO structures, rehabilitation instrumentation, adaptive and photonic-crystal splitters, and corrosion monitoring provide additional context for manufacturability and sensing-oriented use of polymer optical platforms [52-59]. At the integrated-photonics level, SOI multi-racetrack resonator filters offer another example of compact geometry-controlled spectral processing, reinforcing the wider role of structural optimization in wavelength-selective photonic devices [60].

The connection to photonic computing arises because several wavelength channels are physically summed into one optical output. In a conventional WDM link this is simply multiplexing. In a neuromorphic interpretation, the input wavelengths can encode separate signals and the coupling efficiencies can act as fixed optical weights. Earlier work on neural networks in multicore fibers and multimode-fiber neural processing shows that fiber platforms can support distributed optical interactions [17-20]. An AI-assisted design loop could therefore be extended beyond equal-throughput WDM and used to synthesize a target output-weight vector. The present device should be regarded as a passive hardware primitive rather than a trained neural network by itself, but its geometry is compatible with that broader direction.

There are also limitations. First, the four-channel performance reported here is based primarily on numerical BPM modeling, while the experiment validates a two-channel spatial-combination case rather than the complete fabricated four-channel microstructured device. Second, an external machine-learning optimization layer requires a clearly documented training or surrogate-validation protocol if quantitative claims about speedup are to be made. The present paper therefore does not assign an artificial percentage improvement to AI, nor does it claim that RSoft itself is a machine-learning solver. Third, manufacturing tolerances, bending, connector interfaces, surface roughness, and material dispersion should be included more comprehensively in a future fabrication-calibrated model. These limitations define a practical next step: couple measured fiber geometry and optical data back into the optimizer and use the combined data set to refine the surrogate model.

6. CONCLUSIONS

An artificial-intelligence-assisted WDM multiplexer based on multicore plastic optical fiber has been presented for the 500-560 nm green spectral range. The device uses nine polycarbonate coupling regions embedded in a CYTOP-based microstructured fiber to transfer four input wavelengths toward a common output. RSoft BPM provides the electromagnetic propagation solution, while an external AI-assisted optimization stage coordinates the search over geometric parameters and the common switching-length condition. This physics-in-the-loop formulation preserves interpretability and avoids replacing the optical model with an unverified black-box predictor.

The optimized 20 mm structure operates at 500, 520, 540, and 560 nm with simulated transmissions of 88%, 91%, 95%, and 97% and insertion losses from 0.55 to 0.13 dB. The extracted coupling lengths are 395.33, 282.21, 201.23, and 153.52 µm, producing near-integer switching ratios that enable a shared interaction length. The selected d/Λ value of 0.4395 lies inside a common four-channel tolerance region, and the design remains stable for a representative ±3 nm thermal wavelength drift. A two-channel experiment at 500 and 540 nm further supports the spatial multiplexing concept. Overall, the results indicate that AI-assisted RSoft optimization can provide a practical route to compact visible-band WDM components in multicore polymer fibers, with future extensions toward fabrication-aware optimization, adaptive channel weighting, and neuromorphic photonic interconnects.

5.1 Practical AI optimization protocol

A practical implementation of the AI-assisted workflow begins with a bounded design space defined from optical constraints and fabrication limits. The initial population should cover the allowed ranges of d, Λ, Gap, S, and LS rather than concentrating immediately around the nominal optimum. Each candidate is evaluated in RSoft at all four wavelengths, and the resulting feature vector can include the effective index, peak coupled power, first transfer length, output power, insertion loss, and a measure of residual power in undesired cores. These data form a compact training set for a surrogate model. The surrogate does not need to predict the complete optical field; predicting the objective metrics is sufficient and is computationally more efficient. After training, the model proposes new candidates with the largest expected improvement or the best estimated tradeoff among loss, coupling-ratio error, and robustness. Every accepted candidate is then verified with a fresh BPM run, preventing surrogate extrapolation from being mistaken for a physical result.

For the present four-channel problem, a multi-stage strategy is appropriate. In the first stage, broad sampling identifies the parameter regions that preserve modal confinement. In the second stage, the optimizer focuses on the common switching-length condition and searches for designs in which the four coupling ratios are simultaneously close to integers. In the third stage, the best candidates are re-simulated under geometric and spectral perturbations. This final robustness stage is essential because an apparently excellent nominal point may be unusable if a small variation in pitch or wavelength causes a large increase in insertion loss. The reported d/Λ tolerance region from approximately 0.4385 to 0.4408 provides a direct example of the type of common operating window that the optimizer should prioritize. A design is accepted only when the four channels remain inside the selected power and loss limits across the perturbation set.

The optimization loop can also be adapted to experimental calibration. After a prototype is fabricated, measured core locations, core diameters, refractive indices, and output powers can be used to update the simulation model. A data-driven correction term may then learn the systematic difference between the idealized RSoft geometry and the fabricated device. In this way, the AI layer becomes increasingly useful over successive fabrication cycles without obscuring the underlying physics. The workflow is therefore compatible with a digital-twin interpretation: the BPM model supplies the deterministic optical structure, experimental data reveal manufacturing and alignment deviations, and machine learning provides a statistical correction and search policy. Such a strategy is more defensible than assigning the complete field calculation to a neural network because it preserves a direct connection between design decisions and physically interpretable parameters.

5.2 System-level implications for WDM links

At the system level, the multicore POF multiplexer can be placed between wavelength-specific transmitters and a shared downstream optical path. Each source is coupled into its designated input core, and the internal sequence of coupling regions transfers the channels to the common output. Because the wavelengths remain spectrally separated, downstream detection can use wavelength-selective photodiodes, filters, or a reciprocal demultiplexing structure. The measured and simulated losses indicate that the fiber device itself can be a relatively small part of the link budget, particularly at the longer wavelengths where the calculated insertion loss approaches 0.13 dB. In a practical communication system the total penalty will also include source-to-fiber coupling, facet reflections, connector losses, bending, detector responsivity, and any wavelength-selective filtering. The low intrinsic multiplexer loss therefore provides useful margin for these external terms.

The 20 nm channel spacing used here is deliberately large enough to provide clear separation in the green visible band and to simplify the proof-of-concept coupling design. A future design could target smaller spacing if the fiber dispersion, fabrication tolerance, and coupling sensitivity permit it. The AI-assisted workflow is particularly valuable for such scaling because the feasible region is expected to become narrower as channel spacing decreases. Instead of relying on repeated manual scans, the optimizer can treat spacing itself as a design variable and search jointly over wavelength allocation and geometry. Additional objectives could include crosstalk, minimum spectral guard band, total device length, and tolerance to laser linewidth. This would

allow the same physical platform to be adapted to different transmitter technologies and link-capacity requirements.

The green spectral region is also relevant outside conventional data transmission. Multiple wavelengths can interrogate different fluorescent labels, absorption features, or scattering responses in a sensing probe. By combining several source wavelengths into one multicore POF path, the multiplexer can reduce the number of external optical components and support compact distributed probes. In these cases, the optimization objective may not be equal transmission. One channel may be intentionally stronger to serve as a reference or excitation source, while another may be attenuated to match a sensitive detector. The same AI-assisted geometry search can synthesize these unequal target powers by changing the desired output vector. This flexibility links the WDM function to passive optical weighting and makes the architecture relevant to both sensing and photonic-computing applications.

Finally, the present design demonstrates why the phrase AI-assisted should be interpreted as a design methodology rather than a material or propagation mechanism. Polycarbonate, CYTOP, the air-hole lattice, and wavelength-dependent modal coupling determine the physical behavior. RSoft BPM calculates that behavior. Machine learning organizes the search over possible structures and can reduce the number of simulations required to reach a robust solution. Keeping these roles explicit makes the methodology reproducible and allows later studies to compare optimizers fairly. A future experimental campaign should therefore report the optimizer type, parameter bounds, number of RSoft evaluations, surrogate validation error, stopping rule, and the performance of the final BPM-verified design. Those additions would make it possible to quantify the computational benefit of AI while retaining the optical performance metrics used throughout this work.

REFERENCES

1. Leal-Junior, A.G.; Diaz, C.A.; Avellar, L.M.; et al. Polymer Optical Fiber Sensors in Healthcare Applications: A Comprehensive Review. Sensors 19 (2019).
2. Panchuk, M.; Panchuk, A.; Szkodo, M.; et al. Polymer Optic Fibers: Potential of Development and Application in Networks. 3ICT (2022).
3. Wang, Y.; Huang, Y.; Bai, H.; et al. Biocompatible and Biodegradable Polymer Optical Fiber for Biomedical Application: A Review. Biosensors 11 (2021).
4. Sokolowski, P.; Lubinski, J.; Wierzba, P.; et al. Polymer Materials for U-Shaped Optic Fiber Sensors: A Review. Photonics 12 (2025).
5. Sanchez Montero, D.; Perez Garcilopez, I.; Vazquez Garcia, C.; et al. Recent advances in wavelength-division-multiplexing plastic optical fiber technologies. Advances in Optical Fiber Technology 10 (2015).
6. Lethien, C.; Loyez, C.; Vilcot, J.P.; et al. Exploit the Bandwidth Capacities of the Perfluorinated Graded Index Polymer Optical Fiber for Multi-Services Distribution. Polymers 3, 1006-1028 (2011).
7. Gelkop, B.; Malka, D. Design of a four channel green-wavelength multiplexer based on multicore polymer optical fiber. Optics & Laser Technology (2025).
8. Gelkop, B.; Aichnboim, L.; Malka, D. RGB wavelength multiplexer based on polycarbonate multicore polymer optical fiber. Optical Fiber Technology 61, 102441 (2021).
9. Dadabayev, R.; Malka, D. A visible light RGB wavelength demultiplexer based on polycarbonate multicore polymer optical fiber. Optics & Laser Technology 116, 239-245 (2019).
10. Dadabayev, R.; Malka, D.; Shabairou, N.; Zalevsky, Z. A visible light RGB wavelength demultiplexer based on silicon-nitride multicore PCF. Optics & Laser Technology 111, 411-416 (2019).
11. Malka, D.; Katz, G. An Eight-Channel C-Band Demux Based on Multicore Photonic Crystal Fiber. Nanomaterials 8(10), 845 (2018).
12. Malka, D.; Gelkop, B.; Aichnboim, L. RGB multiplexer using polycarbonate MC-POF technology. Proc. SPIE 11773, 1177311 (2021).
13. Dadabayev, R.; Malka, D. RGB wavelength demultiplexer based on PCF/POF structure. Proc. SPIE, Micro-structured and Specialty Optical Fibres VI (2019).
14. Malka, D.; Gindi, M.; Melamed, A. 1x4 VLC wavelength demultiplexer based on multislot waveguide structures. Proc. SPIE 11062, 110620A (2019).
15. Ben Zaken, B.B.; Zanzury, T.; Malka, D. An 8-channel wavelength MMI demultiplexer in slot waveguide structures. Materials 9(11), 881 (2016).
16. Malka, D.; Sintov, Y.; Zalevsky, Z. Design of a 1x4 silicon-alumina wavelength demultiplexer based on multimode interference in slot waveguide structures. Journal of Optics 17(12), 125702 (2015).
17. Malka, D. AI-driven optimization of a compact four-channel SiN MMI WDM for efficient O-band data transmission. Proc. SPIE 13530, 1353007 (2025).
18. Shabairou, N.; Cohen, E.; Wagner, O.; Malka, D.; Zalevsky, Z. Color image identification and reconstruction using artificial neural networks on multimode fiber images. Optics Letters 43(22), 5603-5606 (2018).
19. Cohen, E.; Malka, D.; Shemer, A.; Shahmoon, A.; Zalevsky, Z.; London, M. Neural networks within multi-core optic fibers. Scientific Reports 6, 29080 (2016).
20. Cohen, E.; Malka, D.; Shemer, A.; et al. Micro mirrors based coupling of light to multi-core fiber realizing in-fiber photonic neural network processor. Proc. SPIE 10117 (2017).
21. Smolanski, S.S.; Malka, D. O-Band 4 x 1 Combiner Based on Silicon MMI Cascaded Tree Configuration. Micromachines 17(1), 31 (2026). https://doi.org/10.3390/mi17010031.
22. Frishman, A.; Malka, D. Optimization of titanium nitride thermo-optic phase shifter for O-band applications using silicon nitride waveguides. Optical and Quantum Electronics 58(9), 378 (2026). https://doi.org/10.1007/s11082-026-08975-1.
23. Avital, N.; Sadan, D.; Shikly, M.; Malka, D. Real-Time Prediction of Reading Comprehension Levels from Beta-Band EEG Signals Using Kernel Ridge Regression and Principal Component Analysis. Machine Learning and Knowledge Extraction 8(7), 171 (2026). https://doi.org/10.3390/make8070171.
24. Isakov, O.; Frishman, A.; Malka, D. Data center four-channel multimode interference multiplexer using silicon nitride technology. Nanomaterials 14(6), 486 (2024).
25. Lanziano, L.; Sherf, I.; Malka, D. A 1x8 Optical Splitter Based on Polycarbonate Multicore Polymer Optical Fibers. Sensors 24(15), 5063 (2024).
26. Kuang, R.; Ye, Y.; Chen, Z.; et al. Low-cost plastic optical fiber integrated with smartphone for human physiological monitoring. Optical Fiber Technology 71, 102947 (2022).
27. Xiang, P. A Cost-Efficient RGB Laser-Based Visible Light Communication System by Incorporating Hybrid Wavelength and Polarization Division Multiplexing Schemes. Optics and Photonics 9 (2021).
28. Wang, Y.; Tao, L.; Huang, X.; et al. Enhanced Performance of a High-Speed WDM CAP64 VLC System Employing Volterra Series-Based Nonlinear Equalizer. IEEE Photonics Journal 7(3) (2015).
29. Kumari, M.; Arya, V. Integrated long reach and energy-efficient NGPON-VLC system with OCDM/WDM for smart green buildings. Optik 289, 171280 (2023).
30. Wang, C.; Zhang, D.; Zhang, X.; et al. Bottom-metal-printed thermo-optic waveguide switches based on low-loss fluorinated polycarbonate materials. Optics Express 28, 20773-20784 (2020).
31. Malka, D. A Four Green TM/Red TE Demultiplexer Based on Multi Slot-Waveguide Structures. Materials 13(14), 3219 (2020).

32. Ioudashkin, E.; Malka, D. A Three Demultiplexer C-Band Using Angled Multimode Interference in GaN-SiO2 Slot Waveguide Structures. Nanomaterials 10(12), 2338 (2020).
33. Ohana, E.; Malka, D. O-band grating couplers using silicon nitride structures. Applied Sciences 13(17), 9951 (2023).
34. Elbaz, D.; Malka, D.; Zalevsky, Z. Photonic Crystal Fiber Based 1xN Intensity and Wavelength Splitters/Couplers. Electromagnetics 32(4), 209-220 (2012).
35. Malka, D.; Zalevsky, Z. Multicore Photonic Crystal Fiber Based 1x8 Two-Dimensional Intensity Splitters/Couplers. Electromagnetics 33(5), 413-420 (2013).
36. Malka, D.; Peled, A. Power splitting of 1x16 in multicore photonic crystal fibers. Applied Surface Science 417, 34-39 (2017).
37. Malka, D.; Cohen, E.; Zalevsky, Z. Design of 4x1 power beam combiner based on multicore photonic crystal fiber. Applied Sciences 7(7), 695 (2017).
38. Malka, D.; Danan, Y.; Ramon, Y.; Zalevsky, Z. A photonic 1x4 power splitter based on multimode interference in silicon-gallium-nitride slot waveguide structures. Materials 9(7), 516 (2016).
39. Samoi, E.; Benezra, Y.; Malka, D. An ultracompact 3x1 MMI power-combiner based on Si slot-waveguide structures. Photonics and Nanostructures 39, 100780 (2020).
40. Menahem, J.; Malka, D. A Two-Channel Silicon Nitride Multimode Interference Coupler with Low Back Reflection. Applied Sciences 12, 11812 (2022).
41. Khateeb, S.; Katash, N.; Malka, D. O-band multimode interference coupler power combiner using slot-waveguide structures. Applied Sciences 12, 6444 (2022).
42. Haque, E.; Al Noman, A.; Ahmed, F.; et al. Numerical Investigation of Photonic Crystal Fiber-Based Biosensor for Pathogens Detection in Water. IEEE Access 10, 88885-88893 (2022).
43. Yasli, A.; Ademgil, H.; Haxha, S.; et al. Multi-Channel Photonic Crystal Fiber Based Surface Plasmon Resonance Sensor for Multi-Analyte Sensing. IEEE Photonics Journal 12 (2019).
44. Wang, F.; Liu, C.; Sun, Z.; et al. A Highly Sensitive SPR Sensor Based on Two Parallel PCFs for Low Refractive Index Detection. IEEE Photonics Journal 10 (2018).
45. Sardar, M.R.; Faisal, M.; et al. Dual-Core Dual-Polished PCF-SPR Sensor for Cancer Cell Detection. IEEE Sensors Journal (2024).
46. Teng, C.; Deng, H.; Liu, H.; et al. Refractive Index Sensor Based on Twisted Tapered Plastic Optical Fibers. Photonics 6, 40 (2019).
47. Tavoletta, I.; Arcadio, F.; Renzullo, L.P.; et al. Splitter-Based Sensors Realized via POFs Coupled by a Micro-Trench Filled with a Molecularly Imprinted Polymer. Sensors 24, 3928 (2024).
48. Hou, Y.-L.; Liu, W.-Y.; Su, S.; et al. Polymer optical fiber twisted macro-bend coupling system for liquid level detection. Optics Express 22, 23231-23241 (2014).
49. Wood, A.; Jung, Y.; Richardson, D.J.; et al. Multiport Fiber Optic Beam Splitters for Space Division Multiplexed Systems. IEEE Photonics Technology Letters 32, 795-798 (2020).
50. Gao, Y.; Li, J.F.; Wang, Y.Z.; et al. Design of Ultra Large Normal Dispersion ZBLAN Photonic Crystal Fiber and Its Application in Mid-IR Ultra Short Fiber Lasers. IEEE Photonics Journal 10 (2018).
51. Zhang, L.; Yang, S.; Wang, X.; et al. Photonic Crystal Fiber Based Wavelength-Tunable Optical Parametric Amplifier and Picosecond Pulse Generation. IEEE Photonics Journal 6 (2014).
52. Prajzler, V.; Mastera, R.; Jerabek, V.; et al. Design, Fabrication and Properties of Optical Large Core Polymer Planar 1x2 Splitter. CLEO Pacific Rim (2013).
53. Mohamed-Kassim, N.S.; Abd-Rahman, M.K.; et al. High resolution tunable POF multimode power splitter. Optics Communications 400, 136-143 (2017).
54. Eshaghi, A.; Graeli, A.; et al. Optical and electrical properties of ITO nanostructured thin films deposited on polycarbonate substrates. Optik 125, 1478-1481 (2014).
55. Leal-Junior, A.; Avellar, L.; Jaimes, J.; et al. Polymer Optical Fiber-Based Integrated Instrumentation in a Robot-Assisted Rehabilitation Smart Environment. Sensors 20, 11 (2020).
56. Mohamed-Kassim, N.S.; Ibrahim, A.B.M.; Abd-Rahman, M.K.; et al. Low Loss and Dynamically Tunable Power Splitter Based on Circular-to-Rectangular POF Converter. Journal of Lightwave Technology 34, 1306-1312 (2016).
57. Mustafa, H.A.B.; Xiao, F.; Alameh, K.; et al. A 1x2 adaptive optical splitter based on Opto-VLSI processor. International Symposium on High-capacity Optical Networks (2010).
58. Shukla, A.K.; Gandhi, B.; Pandey, G.N.; et al. A Novel Design of 1x3 Optical Splitter Based on 2D Photonic Crystal. Macromolecular Symposia 407, 2100517 (2023).
59. Hou, L.; Akutagawa, S. Corrosion Monitoring by Plastic Optic Fiber Sensor Using Bi-Directional Light Transmission. Sensors 24, 3229 (2024).
60. Malka, D.; Cohen, M.; Turkiewicz, J.; Zalevsky, Z. "Optical micro-multi-racetrack resonator filter based on SOI waveguides." Photonics and Nanostructures – Fundamentals and Applications, 16, 16–23 (2015).

Deepening oxidation of metal crystals by laser radiation

Arturs Medvids[1], Yuliy Bludov[2], Sergiy Lavrys[1], Iuriy Nasieka[3], Aleksands Michko[1], Volodymir Lozinskii[3]
[1] Riga Technical University, Riga, Latvia
[2] University of Minho, Braga, Portugal.
[2] V.Ye. Lashkaryov Institute of Semiconductor Physics of NAS of Ukraine
E-mail: medvids@latnet.lv

Abstract: The theory of laser-induced oxidation of metals, namely Ti, was developed. The theory accounts for the action of the strong temperature gradient due to laser irradiation as well as the oxygen concentration gradient. This theory is based on the Wagner differential oxidation equation and determines the oxide film thickness depending on the number of laser pulses. Theoretical calculations were confirmed experimentally using a YAG:Nd laser beam at 1.06 µm, a pulse duration of 15 nm and an intensity of 2 MW/cm², which is 10% less than the ablation threshold. Raman and SEM studies show the formation of a TiO_2 film of mixing structural phase (anatase and rutile). It was found that the volume fraction of these phases depends on the intensity of the laser irradiation.

KEYWORDS: LASER OXIDATION, TEMPERATURE GRADIENT, TITANIUM, OXIDE FILM THICKNESS

1. Introduction

Oxidation of metal crystals is very often used in technologies and experiments, for example, thermal oxidation in a furnace, electrochemical oxidation, or plasma-electrolytic oxidation [1-3]. Such methods have limitations in oxidation depth and the formation of a high-quality metal oxide crystal due to the low diffusion length of oxygen in metals; it is less than one micron. Moreover, depending on the oxidation conditions - the phase state of the metal, the environment, and the laser parameters - different phase structures of the oxide can be formed, for example, anatase, rutile, or brookite in a TiO_2 crystal [4], which have different crystal lattice constants, leading to the formation of mechanical stresses and the destruction of the metal oxide. But in modern technologies, deeper oxidation is necessary for various purposes, for example, the formation of an optical window in a vacuum chamber for monitoring and controlling the process or using a laser beam to process the sample. It is proposed to consider laser oxidation as an alternative method, which has the following advantages: locality, process speed, and, most importantly, larger depth of oxidation due to strong heating of the oxide and temperature gradient. Oxygen is supplied to the metal/oxide interface not only due to its diffusion, but also due to the generation of interstitial oxygen in the oxide and its drift in the thermal gradient field [5]. Such technology allows control of a metal-oxide thickness and the possibility to reach the Fabry-Perot resonance modes for lasing in the material.

2. Theoretical model

Theoretically, such a metal oxidation process is described by a modified Wagner differential oxidation equation [6], where a field term proportional to the temperature gradient is added, namely

$$\frac{dH}{dt} = \exp\left(-\frac{T_a}{T}\right)\left(\frac{B_0}{H} - \frac{G_0}{T^2}\frac{\partial T}{\partial x}\right),$$

where $B_0 = D_0\,(c_g - c_m)/N_O$, $G_0 = D_0CQ/(k_B\,N_O)$, D_0 is the diffusion coefficient at $T \to \infty$, T_a is the activation energy of the diffusion process, c_g and c_m are oxygen concentrations at gas and metal sides, respectively, $c = (c_g + c_m)/2$, Q is the heat of transport (thermomigration coefficient) for particle, N_O is the concentration of oxygen bound in the crystal lattice.

The temperature in the gradient term can be approximated by the maximal temperature, while the temperature gradient can be approximated via heat flux q_0, namely

$$K_0\frac{\partial T}{\partial x} + q_0 = 0.$$

Here K_0 is the thermal conductivity. In this case, the differential equation will have the form

$$\frac{dH}{dt} = \exp\left(-\frac{T_a}{T_{max}}\right)\exp\left(-\frac{T_a\left|T''(t_0)\right.}{2T_{max}^2}\ t - t_0)^2\right)\left(\frac{B_0}{H} + \frac{G_0}{T_{max}^2}\frac{q_0}{K_0}\right)$$

where $T''(t_0)$ is the second derivative at time t_0, where maximal temperature T_{max} is achieved. If we consider that

$$\frac{B_0}{H} \gg \frac{G_0}{T_{max}^2}\frac{q_0}{K_0}$$

we can treat the equation perturbatively. We represent $H = H_0 + H_1$, where $H_1 \ll H_0$, and separating orders obtain two differential equations

$$\frac{dH_0}{dt} = \exp\left(-\frac{T_a}{T_{max}}\right)\exp\left(-\frac{T_a\left|T''(t_0)\right.}{2T_{max}^2}\ t - t_0)^2\right)\frac{B_0}{H_0}$$

$$\frac{dH_1}{dt} = -\exp\left(-\frac{T_a}{T_{max}}\right)\exp\left(-\frac{T_a\left|T''(t_0)\right.}{2T_{max}^2}\ t - t_0)^2\right)\frac{B_0}{H_0^2}H_1 - \frac{G_0}{T_{max}^2}\frac{q_0}{K_0}$$

which solutions can be represented as

$$H_0(t) = \frac{}{H_0^2(-\infty) + 2B_0\exp\left(-\frac{T_a}{T_{max}}\ \int_{-\infty}^{t}\exp\left(-\frac{T_a\left|T''(t_0)\right.}{2T_{max}^2}(t' - t_0)^2\right)dt'\right.}$$

$$H_1(t) = \frac{G_0}{T_{max}^2}\frac{q_0}{K_0H_0(t)}\left(\frac{H_0^3(t}{3B_0} - \frac{H_0^3(-\infty}{3B_0}\right].$$

The results are shown on Fig. 1. As one can see, the presence of temperature gradient (green line) increases the growth of oxide, if compared with the case without temperature gradient (red line).

1

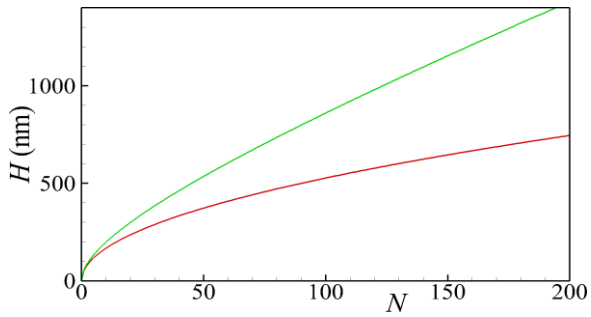

Fig. 1. *Dependence of oxide film thickness H upon number of pulses N for TiO_2 with and without temperature gradient (green and red lines, respectively) for the heat flux q_0 = 52.8 MW/cm^2 and pulse duration τ = 6 ns.*

3. Experimental part

Laser oxidation of Ti plates with a thickness of 1 mm was experimentally investigated. The Ti plate was irradiated with a YAG:Nd laser beam with a diameter of 1.5 mm, a wavelength of 1.06 µm, a pulse duration of 15 nm and an intensity of 52 MW/cm², which is 10% less than the ablation threshold. 5 points were irradiated with different irradiation doses (number of laser pulses), located on one line, each at a distance of 3 mm. Optical microscope studies showed that the color of the irradiated spot changes: the spot darkens with increasing dose. Next, the sample was cut with an ion beam in the middle of the laser spots to measure the thickness of the oxide layer. Measurements showed that the thickness of the TiO_2 layer increases with the irradiation dose and reaches 300 nm, but this layer is opaque and brittle. Additionally, SEM study shows that the surface of the oxide layer is covered with microcracks; see Fig. 2.

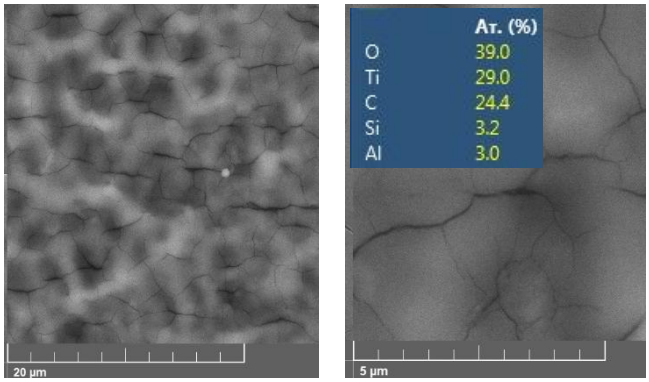

(a) (b)

Fig. 2. *SEM micrographs of the surface of Ti plates with TiO_2 layer before γ-irradiation made at different magnifications. In the insertion – the component composition.*

We explain these properties by the relaxation of mechanical strain caused by the mixing of TiO_2 phases due to lattice mismatch between them. The presence of mixed TiO_2 phases in the oxide layer was demonstrated by Raman spectra; see Fig. 3.

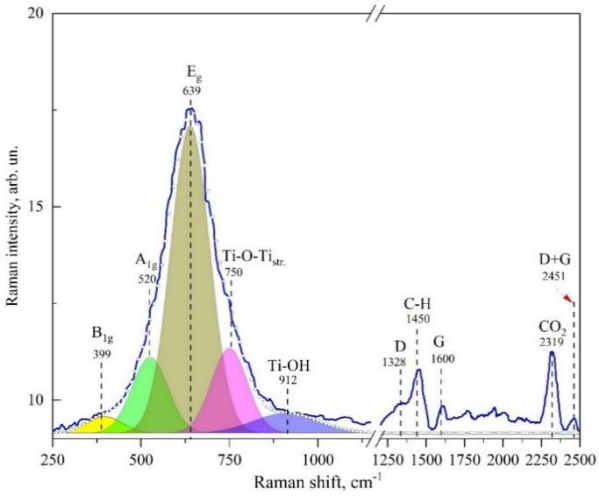

Fig. 3. *Raman spectrum of the laser-formed oxide film on the surface of Ti plate.*

Fig. 3 demonstrates the presence of the typical vibrational bands attributed to both anatase and rutile phases. Additional bands within the range 1250...2500 cm^{-1} are caused by the presence of carbon impurities, which are the residual uncontrolled contamination after mechanical treatment of the Ti plates before laser irradiation. These carbon contaminations can be removed using an ultrasonic bath.

4. Conclusions

The method for laser-induced deep oxidation of metals was developed. Experimental modelling predicted the effective process of oxide film formation. The oxidation rate and the phase composition of the resulted oxide film depend on the conditions of the laser irradiation. Using Ti plates and YAG:Nd laser we obtained the TiO_2 films with the thicnesses up to 300 nm consisting of the mixed rutile and anatase phases. The method is cheap, non-vacuum, and perspective for the formation of the optical windows and other technical purposes, including formation of the radiation-resistant and protective coatings.

5. Acknowledgments

This work was supported by the Ministry of Education and Science of Ukraine under the Ukrainian–Latvian joint research project No. 0225U004570, “Formation of TiO_2 Layers on Ti Substrates Using a Neodymium Laser under Different Radiation Conditions: Scanning Time and Radiation Power.” The project was implemented within the framework of the Ukrainian–Latvian bilateral scientific and technological cooperation programme, with the participation and support of the Latvian side.

The authors acknowledge the financial support from the Latvian Council of Science’’Controllable formation of TiO2 nanolayer on Ti substrate heterostructure by laser radiation for space applications’’, (Programme Latvia-Ukraine/2025/1).

6. References

[1] K. Aniołek, The influence of thermal oxidation parameters on the growth of oxide layers on titanium, Vacuum 144 (2017) 94–100. https://doi.org/10.1016/j.vacuum.2017.07.023.

[2] B. Makurat-Kasprolewicz, A. Ossowska, Recent advances in electrochemically surface treated titanium and its alloys for biomedical applications: A review of anodic and plasma electrolytic oxidation methods, Mater. Today Commun. 34 (2023) 105425. https://doi.org/10.1016/j.mtcomm.2023.105425.

[3] Y. Choi, C. Jeong, Correlation of oxide film thickness with interference coloration and corrosion resistance in anodized titanium, Electrochim. Acta 545 (2026) 147737. https://doi.org/10.1016/j.electacta.2025.147737.

[4]Arturs Medvids , Pavels Onufrijevs, Jevgenis Kaupužs, Raivis E glitis, Juozas Padgurskas, Audrius Zunda, Hidenori Mimura, Ingus Skadins, Sarunas Varnagiris. Anatase or rutile TiO_2 nanolayer formation on Ti substrates by laser radiation: Mechanical, photocatalytic and antibacterial properties, Optics and Laser Technology, **128**, (1221), pp.106898-106916. 10.1016/j.optlastec.2020.106898.

[5] A. Medvids. (2002). Redistribution of the Point Defects in Crystalline Lattice of Semiconductor in Nonhomogeneous Temperature Field. Defects and Diffusion Forum, 210-212, pp.89-102.

6] H. Schmalzried, A.T. Fromhold, jr.: Theory of Metal Oxidation. Vol. 1: Fundamentals. North Holland Publishing Co. 1976. 547 Seiten, Preis: $ 63.50., Berichte Der Bunsengesellschaft Für Phys. Chemie. **81** (1977) 353–354. https://doi.org/10.1002/bbpc.19770810328.

Application potential of lubricants for bearings and gears in space mechanisms – analysis of properties and limitations

Leszek Pawlicki
Warsaw University of Technology, Faculty of Physics ul. Koszykowa 75, 00-662 Warszawa POLAND, contact e-mail: leszek.pawlicki@pw.edu.pl

Abstract: *The reliability of mechanisms used in satellites, interplanetary probes, and planetary rovers largely depends on choosing the right lubricant. Unlike devices used on Earth, space mechanisms operate in conditions of high vacuum, extreme temperature changes, and intense radiation, without any possibility of performing maintenance. This means that conventional lubricants used on Earth don't provide the necessary durability or reliability. The article presents an analysis of the main environmental factors affecting the lubrication process and discusses the properties of the most commonly used types of lubricants in space mechanisms. Special attention is given to perfluoropolyether (PFPE) based greases, multiply alkylated cyclopentanes (MAC), and solid lubricants based on molybdenum disulfide and DLC-type coatings.*
KEYWORDS: *SPACE TRIBOLOGY, SPACE LUBRICANTS, PFPE, MAC, BEARINGS, GEARS, VACUUM.*

1. Introduction

The rapid development of space technologies is increasing demands on the durability and reliability of mechanisms responsible for satellite orientation, solar panel drive systems, antenna positioning, and the operation of scientific instruments. In most of these systems, operational durability is directly linked to the quality of the lubrication system used.

On the ground, effective friction reduction is ensured by a lubricant film separating the surfaces in contact. In space, maintaining such a film is much harder due to the effects of high vacuum, extreme temperatures, and radiation.

Choosing a lubricant is one of the most important steps in designing space mechanisms. A wrong choice can lead to increased friction, faster wear of parts, and loss of functionality of the entire system, so the selection process should take into account both tribological requirements and the impact of the space environment [1].

2. The impact of the space environment on the properties of lubricants

The space environment is quite different from the conditions for which most traditional lubricants were designed. The mix of high vacuum, a wide range of temperatures, and radiation leads to effects that hardly ever happen on Earth, and it requires the use of specialized tribological materials.

Degassing products that settle on optical components, detectors, and photovoltaic panels can cause permanent deterioration of their performance. For this reason, in the design of space mechanisms, special attention is paid to reducing the phenomenon of molecular contamination.

Extreme temperature changes affect viscosity, the ability to form an oil film, and the resistance of moving parts. The lubricant should maintain stable properties both during long periods of cooling and occasional heating of the components.

It's worth noting that vacuum alone doesn't determine the state of a lubricant. What really matters are its physicochemical properties and operating temperature, while vacuum mainly just speeds up the degassing process.

3. Requirements for lubricants intended for space applications

Choosing a lubricant for space applications requires taking into account a lot more factors than in regular industrial systems. Besides tribological properties, long-term physicochemical stability and the ability to operate for many years without maintenance are crucial.

One of the basic criteria for selecting lubricants is their volatility. Due to the high vacuum, materials with very low vapor pressure are preferred, which limits outgassing and the risk of contaminating optical and electronic components.

Equally important is viscosity stability across a wide range of temperatures. Too much of a viscosity increase makes it harder to start the mechanism, while a drop in viscosity leads to a thinner lubricating film.

The lubricant should have high chemical and radiation resistance, limiting the degradation of its molecular structure from ultraviolet and ionizing radiation, and keeping its properties stable throughout its entire service life.

A key requirement remains material compatibility with metals, polymers, and elastomers used in space mechanisms, which helps avoid chemical reactions, material swelling, and deterioration of tribological properties.

In mechanisms that perform small oscillating movements, it's especially important to limit the stick-slip phenomenon, which can worsen the positioning accuracy of optical instruments and actuating systems.

An important requirement is also limiting the risk of adhesive welding (cold welding), which under high vacuum conditions can lead to permanent damage to the surfaces in contact.

In summary, a lubricant meant for space applications should combine low volatility, high physicochemical stability, radiation resistance, proper tribological properties, and full material compatibility. In practice, the optimal choice is always a compromise based on the mission's nature and the mechanism's design.

4. Analysis of selected groups of lubricants (liquid)

4.1. Mineral oils

Mineral oils played an important role in the development of classical tribology, but their physicochemical properties don't meet the requirements for mechanisms working in space.

Unfortunately, most mineral oils are practically unsuitable for space applications. The main limitation is their relatively high vapor pressure, which leads to significant outgassing in a vacuum. This process causes a gradual loss of the lightest fractions, changes in viscosity, and the possibility of contaminating optical components. Additionally, mineral oils have limited resistance to radiation and relatively rapid thermal aging [2, 6, 9].

For this reason, mineral oils are nowadays hardly used as primary lubricants in mechanisms intended for long-term work in space. However, they can be used in laboratory research and in selected short-term technological experiments, but they are not a solution for long-term space missions.

4.2. Polyalphaolefin oils (PAO)

Polyalphaolefins (PAO) are synthetic hydrocarbons with favorable viscosity- temperature properties and high operational stability.

Compared to mineral oils, they also have much lower volatility, which allows them to operate in moderate vacuum conditions for a much longer time. However, they don't completely eliminate the problem of outgassing, so their use in long-term space missions is still limited [7, 9–12].

The advantage of PAO oils, on the other hand, is their very good lubricating properties and the ability to work with a wide range of anti-wear and antioxidant additives. For this reason, they are mainly used in equipment operating under controlled conditions or as a reference point during tests of new lubricants.

4.3. Ester oils

Synthetic ester oils provide good lubricating properties and a favorable change in viscosity with temperature.

However, their use in space is limited. The main problem remains the relatively high volatility of some esters and the possibility of gradual chemical degradation over years of use. High-energy radiation can break ester bonds, leading to changes in viscosity and worsening wear-resistant properties.

Despite the mentioned limitations, certain synthetic ester oils are still used in specific auxiliary mechanisms, especially where good low-temperature properties and low starting resistance are a priority.

4.4. Silicone oils

Silicone oils maintain stable viscosity properties over a wide range of temperatures, which is their main practical advantage.

Their main drawback, however, is the relatively easy migration across the surfaces of construction materials. In high-vacuum conditions, this can lead to contamination of optical surfaces and electronic components, even if the evaporation process itself is relatively slow. This phenomenon is particularly important in space telescopes and observation satellites, where even a small amount of deposited contaminants can degrade the quality of the data obtained [4, 8, 12].

For this reason, silicone oils are mainly used in selected auxiliary mechanisms, while they are avoided in systems that require the highest optical purity and minimal risk of contamination.

4.5. Perfluoropolyethers (PFPE)

The most practically important lubricants in space tribology nowadays are those based on perfluoropolyethers (PFPE).

The chemical structure of PFPE, based on carbon–fluorine bonds, provides exceptionally high chemical stability, low vapor pressure, and resistance to oxidation. These properties limit lubricant loss from outgassing and help maintain stable performance over many years of operation in high vacuum.

PFPEs maintain favorable viscosity-temperature properties over a wide range of temperatures, which is why they are used in precision mechanisms that require high reliability and consistent movement.

PFPEs are mainly used in mechanisms where long-term, maintenance-free operation is required while maintaining high precision of movement.

The main limitations of PFPE are the high cost and the limited load-carrying capacity of the lubricant film under very high contact pressures. For this reason, they often work together with self-lubricating or protective coatings.

PFPEs are currently the most commonly used group of liquid lubricants in space mechanisms, which comes from a favorable compromise between low volatility, high chemical stability, and long-lasting operational durability.

4.6. Multiply alkylated cyclopentanes (MAC)

Multiple-alkylated cyclopentanes (MACs) are among the most important synthetic lubricants used in space technology, especially in mechanisms exposed to high contact pressures.

MAC oils are known for their very good resistance to evaporation, high thermal stability, and beneficial anti-wear properties. Many studies have shown that they lead to less wear on rolling elements and higher fatigue life of bearings compared to conventional fluorine-based lubricants [9–15].

A key advantage of MAC oils is that you can effectively use anti-wear and antioxidant additives, which lets you tailor their properties to the specific requirements of a given mechanism.

As a result, MAC lubricants are now considered one of the main solutions for heavily loaded bearings and space gearboxes, complementing PFPE applications where a higher load-bearing lubricant film is needed.

4.7. Ionic liquids

Ionic liquids are one of the most promising groups of lubricants for future space applications. Their practically zero vapor pressure and the ability to tailor their properties by choosing different cations and anions make them an attractive alternative to traditional synthetic oils.

Their biggest advantage is practically zero vapor pressure, which means the degassing process is almost completely eliminated. This characteristic makes them particularly interesting candidates for space applications, where the loss of lubricant is one of the main operational limitations [15–20].

Additionally, ionic liquids show very good anti-wear properties and the ability to form durable boundary layers that limit direct contact between interacting surfaces.

Despite their very promising properties, the use of ionic liquids is currently still limited to the research stage. The main challenges include assessing their stability under long-term radiation exposure, material compatibility, and the durability of boundary layers under real operating conditions.

5. Solid lubricants and tribological coatings

Despite the rapid development of liquid lubricants, many space mechanisms still use solid greases and tribological coatings. These solutions effectively eliminate the outgassing problem and reduce the risk of losing lubricating properties during years of operation in a vacuum.

Their use is especially beneficial in mechanisms performing small oscillating movements, in parts working at low speeds, and in systems where even slight contamination of optics or electronics is unacceptable.

5.1. Molybdenum disulfide (MoS_2)

The most commonly used self-lubricating material remains molybdenum disulfide (MoS_2), which, thanks to its layered crystal structure, shows a very low friction coefficient, especially in high vacuum conditions.

The biggest advantage of MoS_2 coatings is that they maintain a very low friction coefficient in high vacuum conditions. Unlike working in Earth's atmosphere, the absence of oxygen and moisture limits surface degradation processes, which is why the material has remained a standard in satellite mechanisms and scientific instruments for many years.

MoS_2 coatings are mainly applied using PVD and magnetron sputtering methods, which allows for obtaining uniform layers with high adhesion and consistent tribological properties.

5.2. Tungsten disulfide (WS_2)

An alternative to MoS_2 is tungsten disulfide (WS_2), which is known for its high wear resistance and good stability at elevated temperatures.

WS_2 shows tribological properties similar to MoS_2, while in many applications it has higher thermal resistance and better operational stability. For this reason, it is being considered as a material for mechanisms working in especially demanding conditions of interplanetary missions.

5.3. Polytetrafluoroethylene (PTFE)

Polytetrafluoroethylene (PTFE) is a material with a very low friction coefficient and high chemical resistance. It's most often used as a component in composites or lubricants designed to work in a vacuum.

PTFE is mainly used as a component in self-lubricating composites and bearing materials. Because it has limited creep resistance and lower load capacity, it doesn't replace MoS_2 or WS_2 coatings in heavily loaded friction pairs, but it effectively complements them in selected applications.

5.4. DLC Coatings

Diamond-Like Carbon (DLC) coatings are currently one of the most rapidly developing types of protective and tribological coatings. They combine high hardness, excellent wear resistance, and a low friction coefficient.

DLC coatings can be applied to steel as well as light structural alloys, providing high wear resistance and protection in case of local breakdown of the lubricant film. The biggest benefits are seen in hybrid systems where they work together with a liquid lubricant.

5.5. Graphite greases

Graphite is a classic lubricating material with a layered crystal structure. However, in high vacuum, its tribological properties deteriorate due to the desorption of molecules adsorbed on the surface.

In industrial applications, graphite has been used for many years as a component in greases, a self-lubricating material, and an additive for tribological composites. It works especially well at high temperatures and in environments where using conventional oils is difficult.

It might seem that graphite's layered structure makes it an ideal material for use in space. However, tribological studies have shown that its properties strongly depend on the presence of water molecules and gases adsorbed on the surface of the graphene layers. In Earth's atmosphere, these molecules help layers slide over each other and reduce their mutual interaction. In high vacuum conditions, these molecules desorb, which leads to an increase in the friction coefficient and faster wear of the contacting surfaces. This phenomenon makes graphite less capable of maintaining its favorable tribological properties compared to working in the atmosphere.

Classic graphite lubricants have limited use in space technology. In practice, they have largely been replaced by layered materials like MoS_2 and WS_2, which maintain favorable tribological properties even in high vacuum.

6. Comparison of the properties of the analyzed lubricants

The analysis shows that choosing a lubricant for space mechanisms is a multi-criteria issue. The choice depends at the same time on the type of load, thermal conditions, working environment, required durability, and the acceptable level of contamination risk for sensitive components. For this reason, there isn't a universal lubricant that optimally meets all operational requirements.

Classical mineral oils are the least useful in space applications. PAOs and esters can be used in certain cases, but in terms of durability and resistance to the space environment, they fall short compared to PFPEs and MACs.

PFPE and MAC are currently considered the most technologically advanced liquid lubricants. PFPEs stand out for their low volatility, while MACs provide a higher load-bearing capacity of the lubricant film.

Hybrid systems that combine liquid lubricants with tribological coatings are becoming increasingly important. This solution boosts resistance to local lubricant film loss and improves the reliability of mechanisms over years of use.

Some of the most promising areas of development include ionic liquids and hybrid systems that combine liquid lubricants with modern tribological coatings. However, their widespread use still requires more research on long-term durability, radiation resistance, and material compatibility.

7. Conclusions

The analysis confirms that the effectiveness of lubrication in space mechanisms depends on properly matching the lubricant to the working conditions, not on choosing a one-size-fits-all solution.

Currently, PFPE and MAC lubricants, as well as MoS_2, WS_2, and DLC coatings, have reached the highest level of technological maturity and are reference solutions for modern space mechanisms.

The most promising directions for further development include hybrid systems, ionic liquids, and new functional materials that allow for longer-lasting mechanisms and increased reliability of future missions.

8. References

[1] Conley P.L., Space Vehicle Mechanisms: Elements of Successful Design, John Wiley & Sons, New York, 1998.

[2] Jones W.R. Jr., Jansen M.J., Space Tribology, NASA/TM-2000-209924, NASA Glenn Research Center, Cleveland, OH, USA, 2000.

[3] Roberts E.W., Todd M.J., Space Tribology, Elsevier, Amsterdam, 1990.

[4] Bhushan B. (Ed.), Modern Tribology Handbook, CRC Press, Boca Raton, 2001.

[5] Bhushan B., Introduction to Tribology, 2nd ed., John Wiley & Sons, 2013.

[6] Mang T., Dresel W., Lubricants and Lubrication, 3rd ed., Wiley-VCH, Weinheim, 2017.

[7] Totten G.E. (Ed.), Handbook of Lubrication and Tribology, 2nd ed., CRC Press, Boca Raton, 2006.

[8] Hamrock B.J., Schmid S.R., Jacobson B.O., Fundamentals of Fluid Film Lubrication, 2nd ed., CRC Press, Boca Raton, 2004.

[9] Fusaro R.L., Khonsari M.M. (Eds.), Tribology and Lubrication for Extreme Environments, STLE, Park Ridge, IL.

[10] Campbell M.E., Spacecraft Mechanisms Handbook, Aerospace Press, El Segundo, CA.

[11] Spalvins T., "Frictional and Wear Characteristics of Sputtered MoS_2 Films", NASA Technical Report.

[12] Hilton M.R., Fleischauer P.D., "Applications of Solid Lubricant Films in Spacecraft Mechanisms", Proceedings of the Aerospace Mechanisms Symposium.

[13] Fleischauer P.D., "Effects of Environment on the Tribological Performance of MoS_2 Coatings", Tribology International.

[14] Lansdown A.R., Lubrication and Lubricant Selection, 3rd ed., ASME Press, New York, 2004.

[15] Masuko M., Miyoshi K., Spalvins T. (Eds.), Tribology for Space Applications, Elsevier, Amsterdam, 1993.

[16] Roberts E.W., Eiden M., A Space Tribology Handbook, ESA Bulletin, No. 94, European Space Agency, 1998.

[17] Fusaro R.L., Khonsari M.M., Liquid Lubrication for Space Applications, NASA Technical Memorandum NASA-TM-105198, NASA Lewis Research Center, Cleveland, OH, 1992.

[18] Blau P.J., Friction Science and Technology, CRC Press, Boca Raton, 2008.

[19] Hutchings I.M., Shipway P., Tribology: Friction and Wear of Engineering Materials, 2nd ed., Butterworth-Heinemann, Oxford, 2017.

[20] Williams J.A., Engineering Tribology, Cambridge University Press, Cambridge.

Modern methods of manufacturing long tubular porous powder filter elements

Aliaksandr Ilyushchanka [1, 2], Iryna Charniak [2*], Aleksej Kusin [2], Anastasia Astapenka [2], Margaruta Kuntsevich [2], Ruslan Kusin [2]

State research and production powder metallurgy association, Minsk, Republic of Belarus [1]
State Scientific Institution "O.V. Roman Powder Metallurgy Institute", Minsk, Republic of Belarus [2]
E-mail: alexil@mail.belpak.by, charniakirynanik@gmail.com, 2312444@mail.ru, anasnasiy2012@gmail.com, kunczkvich@gmail.com, 19081877@mail.ru

Abstract: *This article presents information on modern methods for manufacturing long-length tubular porous powder filter elements, including hydrostatic and dry radial isostatic pressing, mold pressing, sintering of loosely formed powder in a mold, and roller deformation of flat porous sintered blanks. The advantages and disadvantages of these methods are described. Photos of typical products manufactured using these methods are presented.*
Keywords: *TUBULAR FILTER ELEMENT, POROUS, POWDER, PRESSING, SINTERING*

1. Introduction

Porous materials with through pores are widely used in various science and technology fields, and products made from them are most often used as filter elements (FE) in filters for purifying liquids and gases from various types of contaminants [1,2]. Among the porous materials used for the manufacture of filter elements, powder filter materials based on metal powders (PFM) are at an important place. They have a good combination of throughput and filtration fineness, are durable, resistant to thermal shock, can be welded, soldered and mechanically processed, and can be repeatedly regenerated using various methods; the choice of an appropriate material ensures the necessary corrosion resistance, heat resistance and thermal conductivity, which makes it possible to use products made from them at high temperatures and in aggressive environments, including, for example, working with acids, alkalis, aggressive and hot gases [3,4]. When choosing the design of filter elements, preference is often given to long tubular products: compared to filter elements of a plate (lenticular) or flat shape, there is no need to seal a large number of joints between the "lenticulars" and between the elements in the lenticular itself during installation [5]. Examples of these designs are shown in Figure 1.

Fig. 1. FE for oil purification in the form of lentils and tubes.

This paper presents information on the authors' experience in using methods for manufacturing long-length tubular porous powder filter elements.

2. Materials and research methods

It's known [1-4] that the technology for producing porous powder materials consists of the process of powder preparation, shaping, and sintering. It's the shaping stage that ensures the production of blanks (moldings) of the required shapes, sizes, porosity, and the necessary porosity for subsequent processing (and transportation) [6]. Shaping can occur with or without the pressure application.

Pressure-free molding is typically performed using spherical powders (when pressure activation of interparticle contacts isn't required and binders are used) by sintering the powder loosely poured into the mold. However, the manufacture of molds for long filter elements (length to diameter ratio greater than 4) requires large amounts of expensive metal and is time-consuming; in addition, difficulties arise with removing the sintered material from the rod. In this regard, the rolling method of sintered powder sheet blanks is generally preferred [5]. As noted in [5], this technology can be used to manufacture various sizes of long tubular porous powder filter elements with outside diameters from 40 to 500 and lengths up to 1500 mm or more, since the increase in product dimensions is achieved by welding (gluing or soldering is also possible); moreover, the developed technology allows for the manufacture of two-layer materials, ensuring increased product efficiency. Figure 2 shows, as an example, large-sized filter elements for air purification (two filter elements contain layers of polymer pre-filtration fabric.

Fig. 2. Large filter elements for air purification.

Among the various methods for forming metal powders with applied pressure, mold pressing is the most widely used [7]. However, due to the uneven density distribution across the press height, mold pressing doesn't allow the production of long products (with a press length to diameter ratio greater than 4) [7,8]; this is additionally accompanied by the formation of a narrowing along the outer diameter in the central part of the workpiece during sintering. Increasing the length of filter elements is possible by soldering, welding, gluing, tightening, or by threading several parts obtained by mold pressing, but the requirements for tightness, reduction in filtration area, and additional labor costs make the creation of such designs impractical. Exceptions are cases where the required product length significantly exceeds technological capabilities. Therefore, this method is rarely used by the authors.

Dry isostatic pressing has been adopted as the primary method for forming metal powders with applied pressure in the manufacture of long

tubular porous powder filter elements [9]. The basic design diagram of the device for implementing this method is shown in Figure 3.

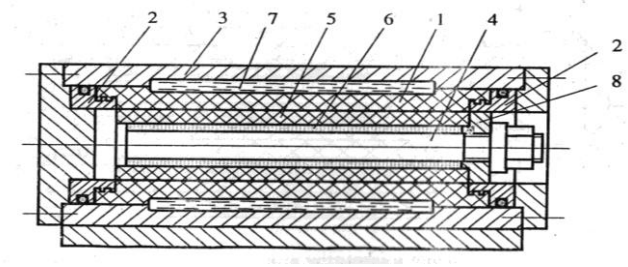

Fig. 3. Large-sized filter elements for air purification: elastic insert made of elastic material (1); reinforcing elements (2); corps (3); rod (shaping element) (4); elastic shell (shaping element) (5); powder charge (6); working fluid transmitting pressure (oil) (7); shut-off flange (8).

The dry isostatic pressing method was chosen because it eliminates contact friction between the powder and the elastic shell, ensuring uniform density distribution throughout the compact. There is no problem with mold tightness, as it is not in contact with the pressure-generating area (oil in hydrostatic pressing or water in hydrodynamic pressing). There is no need for enhanced labor protection requirements, and the addition of plasticizers isn't required. Figure 4 shows filter elements made from titanium powder for air sterilization in a microbiological production facility.

Fig. 4. Titanium filter elements for air sterilization.

In cases where the equipment used doesn't allow for the production of a compact of the required length, the filter element is manufactured by joining sintered blanks of shorter length. Figure 5 shows a long filter element designed for filtering gaseous melamine.

Fig. 5. Titanium filter element for filtering gaseous melamine.

The filter element design, with a total length of 3675 mm, consists of nine long tubular titanium powder porous elements with an outer diameter of 80 mm and a length of 360 mm. Corrosion-resistant steel flanges are hermetically sealed at the ends of the porous elements using high-temperature adhesive. These flanges are used for welding connections to adjacent elements (with the exception of the flanges on the two outer porous elements, one of which has an outer flange for connection to a plug with a centering protrusion (designed to adjust the orientation of the product in space relative to other process elements), and the other for connection to the filter element nozzle, designed for installation of the last filter element in the process line). In special cases, when the use of the method described above is impractical (for example, small sizes and quantities of manufactured products), the hydrostatic pressing method in a hydrostat of the LG-3 type is used. Figure 5 shows filter elements for filtering liquids: the outer ones are made of electrolytic nickel powder, the one in the center is made of knitted steel (grade 12X18N) mesh.

a)

b)

Fig. 6. Filter elements for liquids filtration: external appearance (a) and view from the hole side (b).

The filter elements are 138 mm long, with an outer diameter of 6 mm and an inner bore diameter of 2 mm. It's worth noting that polyurethane was used for the outer shell, which facilitated the powder loading process and sealed it from the pressure-transmitting medium.

3. Conclusion

This article presents information on modern methods for manufacturing long-length tubular porous powder filter elements, including hydrostatic and dry radial isostatic pressing, mold pressing, sintering, and rolling deformation of porous sintered blanks. The disadvantages and traditional methods are described. Photos of various manufacturing methods used are presented.

4. Reference

1. F.V. Pelevin, Technology of porous materials production, Bulletin of the Association of Universities of Tourism and Service, **3** (2007).
2. A.Ph. Ilyushchanka, R.A. Kusin, I.V. Zakreysky, N.N. Yakimovich, I.M. Charniak, A.R. Kusin A., D.I. Zhegzdryn, *Powder filter materials: control of structure and properties and application in agriculture* (Minsk, BSATU, 2018).
3. S.V. Belov, *Porous Metals in Mechanical Engineering* (Moscow, Mashinostroenie, 1981).
4. S.V. Belov, P.A. Vityaz, V.K. Sheleg, V.M. Kaptsevich, V.A. Pavlov and et., *Porous permeable materials* (Moscow, Metallurgy, 1987).
5. A.Ph. Ilyushchanka, I.M. Charniak, A.K. Kusin, A.A. Astapenka, M.D. Kuntsevich, R.A. Kusin. Dimensional limitations in the manufacture of tubular filter elements from flat porous powder blanks. Inter. Sc. J. Innovations, Sofia, Bulgaria, **14**, 2 (2026).
6. B.F. Shibryaev, *Porous permeable sintered materials* (Moscow, Metallurgy, 1982).
7. *Powder Metallurgy. Sintered and Composite Materials / Translated from German*. Ed. by V. Shatt (Moscow, Metallurgy, 1983).
8. S.V. Belov, *Porous metals in mechanical engineering* (Moscow, Mashinostroenie, 1976).
9. V.M. Kaptsevich, L.S. Boginsky, R.A. Kusin, O.P. Reut, Filter materials: promising areas of application in the agro-industrial complex and modern production technologies, (Minsk, BSATU, 2006).

Surface treatment of copper using a plasma from a helicon source

E. Rudenko[1], I. Korotash[1], A. Novytska[1], D. Polotskiy[1], M. Dyakin[1]
G. V. Kurdyumov Institute for Metal Physics of the N.A.S. of Ukraine[1]
novanna99@gmail.com

Abstract *It has been shown that high-density helicon plasma flows (up to 10^{12} cm^{-3}) are effective for nanostructuring copper surfaces and creating the necessary nanointerfaces, which allow for a significant reduction in interfacial thermal resistance. The technical parameters of helicon plasma processes for forming interface nanostructures with reduced thermal resistances have been experimentally determined.*
Keywords*: HELICON PLASMA, COPPER SURFACE, NANOSTRUCTURES, THERMAL RESISTANCE AT THE INTERFACE*

1. Introduction

Nanostructured materials form the basis for the creation of next-generation functional devices, including highly sensitive sensors, energy storage and conversion devices, photodetectors, optoelectronic components, catalysts, and protective coatings. Reducing the characteristic dimensions of structures to the nanometer range increases the specific surface area and enables targeted control of the electrical, optical, and chemical properties of materials. [1–2].

The surface treatment of solids using concentrated energy beams—in particular, laser, electron, and ion radiation—can lead to the self-organized formation of hierarchical structures spanning the micro-, submicron, and nanometer scales. The morphology of the resulting surface relief is determined by the properties of the material and the irradiation parameters and results from the interaction of processes such as energy release, melting, evaporation, sputtering, mass transfer, surface diffusion, and solidification. [3–4].

In modern micro- and nanoelectronics, one of the most important parameters is the thermal resistance of interfaces [5-6]. Many studies have shown that an increase in the roughness of an interface leads to an increase in its thermal resistance [7]. At the same time, the authors [8] In 2017, they showed that nanointerfaces—whose structure contains regions smaller than 1 μm—can, in fact, reduce thermal resistance by a factor of two or more.

There are many methods for nanostructuring surfaces [9] one of which is plasma-based methods [10]. Helicon plasma is one of the radio frequency plasma source that can generate high-density and low-temperature plasmas by utilizing the helicon wave, i.e., the electromagnetic whistler wave in a bounded geometry. It is characterized by a high concentration of charged particles and high ionization efficiency [11].

This study shows that the use of plasma from a helicon source for the nanostructuring of copper surfaces makes it possible to create the desired nanointerfaces, which significantly reduce the specific thermal resistance compared to an untreated surface.

The goal of this work was to experimentally investigate the microstructure of a copper surface after treatment in a high-density helicon discharge plasma and to determine the parameters of the helicon plasma process that ensure a significant reduction in the thermal resistance of the interface.

2. Materials and experimental procedure

Sample surface treatment in helicon plasma flows was performed in unique ion-plasma vacuum processing equipment (Fig. 1). It comprises a Helicon plasma source, in which the Helicon discharge is excited by a RF generator operating at 13.56 MHz [12–21]. The nanostructuring of copper sample surfaces in ion-plasma flows of ultra-high-density.

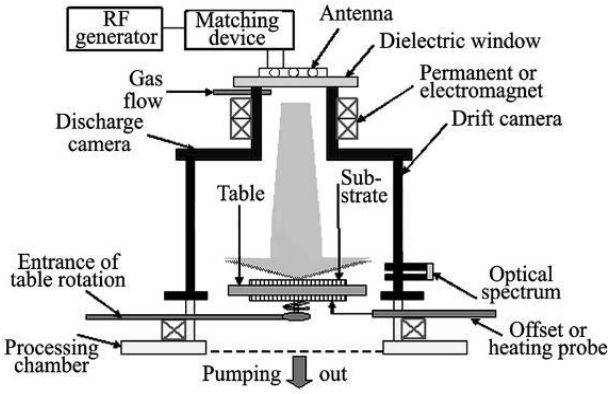

Fig. 1 *Schematic image of the construction of the ion-plasma vacuum-technological equipment with a helicon plasma source with separated discharge and drift cham-bers It comprises a Helicon plasma source, in which the Helicon discharge is excited by a high-frequency generator operating at 13.56 MHz.*

The nanostructuring of copper sample surfaces in ion-plasma flows of ultra-high-density Helicon plasma was carried out in the highly efficient "Plasma Column" mode (Fig. 2).

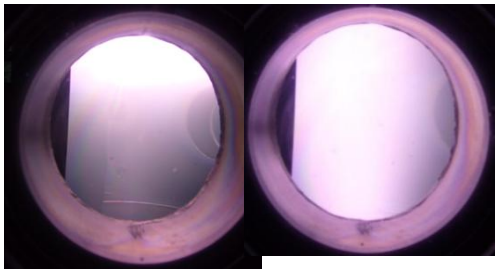

a) ***b)***

Fig. 2 *A typical volumetric helicon discharge (a) and the newly discovered highly efficient "Plasma Column" helicon discharge (b).*

The processing chamber, which houses the substrate stage, is connected directly to the flange of the vacuum system. Above the processing chamber is the drift chamber, to which vacuum-arc accelerators are connected. The drift chamber is connected to the discharge chamber of the Helicon source. This chamber is sealed at the top with quartz glass, through which RF energy is introduced into the discharge via an antenna connected to an RF generator through a matching network.

Monitoring of the ion-plasma processes within the system is performed using a compact optical spectrometer and an electrical probe, with data displayed on a computer monitor.

Technical specifications of the system:

Substrate diameter: 100 mm

Helicon discharge excitation frequency: 13.56 MHz;

Operating pressure: 1–100 mTorr;

Maximum substrate temperature: 600 °C.

Operating gas - Argon; sample size - 20 × 30 mm; diameter of the sample holder D = 48 mm; area of the sample holder S_{st} = 18.1 cm².

Sample treatment was performed for 10 and 20 minutes at a constant pressure of $5 \cdot 10^{-3}$ Torr; and voltages applied to the substrate-holder stage of U_{st} = -200 V and -400 V. The ion current density was approximately 5.52 mA/cm². The processing parameters for the samples listed in the table 1.

Table 1: *The processing parameters for surface treatment of copper using a Helicon discharge plasma.*

Sample	U_t, W	$I_{ст}$, mA	P, t	i, mA/cm^2	t, min
Cu_n$_1$	unprocessed	-	-	-	-
Cu_n$_2$	200	160	32	8,8	10
Cu_n$_3$	400	190	76	10,5	10
Cu_n$_4$	400	190	76	10,5	20

The morphology of the copper samples was investigated using atomic force microscopy (AFM). A “FemtoScan” scanning probe microscope was used in contact mode at a constant probe-surface interaction force.

The resulting AFM images, which reflect the topography of various surface areas of the copper samples, are shown in (Fig. 3 – 6). Lighter colors indicate higher surface areas, while darker tones correspond to lower areas of the relief. The height scale is shown to the right of the 2D image (a). The figures labeled (b) show 3D images rotated 90 degrees counterclockwise relative to their corresponding 2D images. The letter (c) denotes cross-sections along the line shown in the 2D images.

Figure 3 shows AFM images of a section of a Cu sample that was not treated with a Helicon plasma source. Its surface has the following parameters: root mean square roughness R_q =40,2 nm, arithmetic mean roughness R_a = 32,6 nm That is, the surface of the Cu_n$_1$ sample is relatively smooth, and the AFM profile does not show any nanoscale structures.

For the Cu_n$_3$ sample, the ion energy was increased to 400 eV and the current density to 10 A/cm^2. The AFM images obtained from surface treatment under these conditions are shown in Fig. 5. Under these treatment conditions, the surface topography began to smooth out. The roughness parameters decreased, specifically to R_q = 61,1 nm i R_a = 40,5 nm. The number of nanostructures on the surface also decreased.

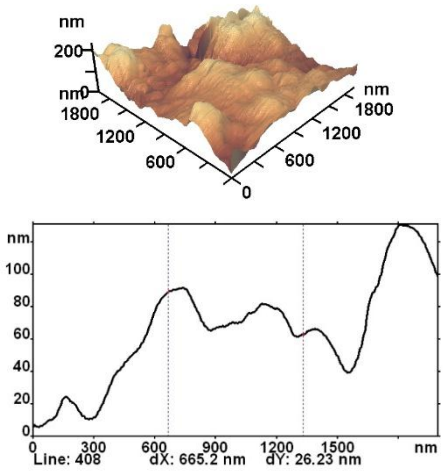

Fig. 3 *AFM images of the topography (a), a cross-sectional profile along the line (c), and a three-dimensional image (b) of the surface of the Cu_n$_1$ copper sample, which was not treated in a helicon discharge plasma.*

Fig. 4 shows ASM images of a section of a sample that was treated with plasma from a Helicon source (Cu_n2 sample). Its surface has the following parameters: root mean square roughness R_q =206,5 nm, arithmetic mean roughness R_a = 220,4 nm. The surface roughness of the Cu_n$_2$ sample is nearly five times greater than that of the untreated Cu, sample, but its AFM profile exhibits a large number of nanoscale structures. These nanoscale structures were formed by a helicon plasma, whose charge energy was only 200 eV, and the surface was treated for only 10 minutes. The current density on the substrate was 8.8 A/cm².

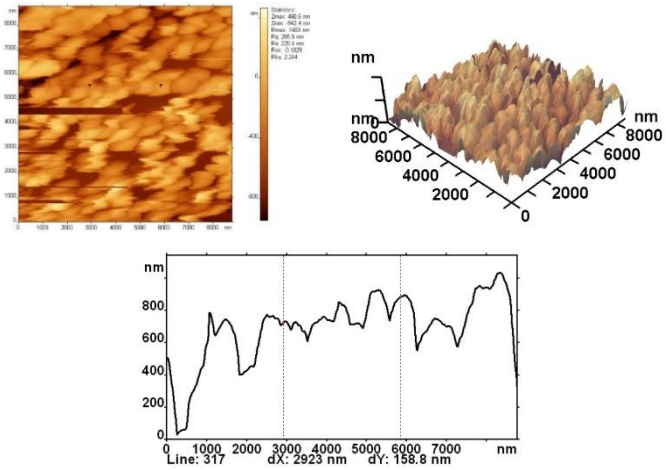

Fig. 4 *AFM images of the topography (a), a cross-sectional profile along the line (c), and a three-dimensional image (b) of the surface of a Cu_n$_2$ copper sample that was treated in a helicon discharge plasma.*

For the Cu_n$_3$ sample, the ion energy was increased to 400 eV and the current density to 10 A/cm². The AFM images obtained from surface treatment under these conditions are shown in (Fig. 5). Under these treatment conditions, the surface topography began to smooth out. The roughness parameters decreased, specifically to R_q = 61.1 nm and R_a = 40.5 nm. The number of nanostructures on the surface also decreased.

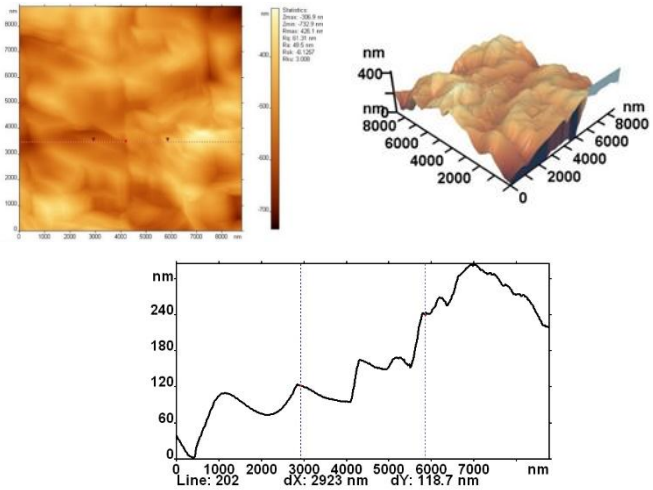

Fig. 5 *AFM images of the topography (a), a cross-sectional profile along the line (c), and a three-dimensional image (b) of the surface of the specimen, characterizing the surface of the Cu_n3 samples after their treatment in a helicon discharge plasma.*

In the latter mode, the processing time was increased to 20 minutes (Cu_n$_4$ sample). In this mode, not only did the nanostructures disappear (see Fig. 6), but the cross-sectional profile also showed no signs that could be attributed to nanostructures. Conversely, for the Cu_n$_4$ sample, surface erosion began, and its roughness increased to values of R_q = 281.4 nm and R_a = 234.3 nm.

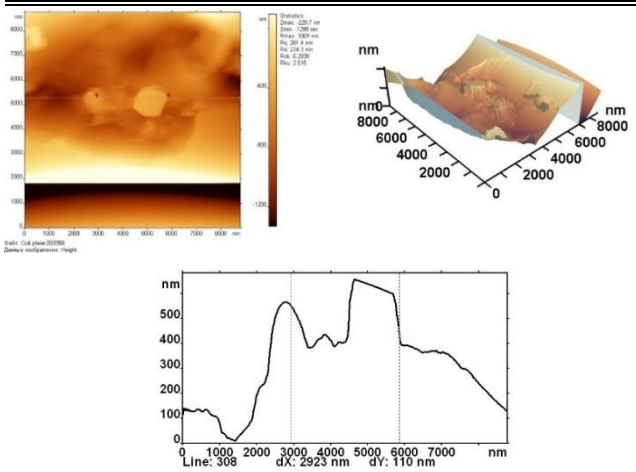

***Fig. 6**- AFM images of the topography (a), a cross-sectional profile along the line (c), and a three-dimensional image (b) of the surface of the specimen, characterizing the surface of the Cu_n$_4$ samples after their treatment in a helicon discharge plasma.*

How did this plasma treatment of the surface of a Helicon source affect its thermal resistance?

The study of heat transport through nanostructured interfaces was conducted using the steady-state heat flux method. A high-power (LED 3W Warm white 120 Lm BIN2 Thermocouple thermometers were used to obtain data on the temperature of the heat source (T_1) and the interface (T_2). When calculating the thermal resistance of the sample, R_{th}, we assumed that 75% of the power supplied to the LED is converted into heat: $Q=P_{th}= 0{,}75P$. The thermal resistance R_{th} of the interface is determined according to Fourier's law using the formula $R_{th} = (T_1 - T_2)/P_{th}$.

Table 2 lists the technical parameters of the experiments and the calculated thermal resistances R_{th} of the corresponding structures.

***Table 2:** Technical parameters of the experiments and thermal resistances R_{th} of the corresponding interface structures*

Sample	*t*, min	*Pth*, W	T_1, ºC	T_2, ºC	ΔT, ºC	R_{th}, K/W
Cu_n$_1$	-	1,07	37,9	33,9	4	3,74
Cu_n$_2$	10	1,07	41,9	38,6	3,3	3,08
Cu_n$_3$	10	1,08	37,2	33,3	3,9	3,6
Cu_n$_4$	20	1,08	41,9	37,2	4,7	4,4

From Table 2, which shows the thermal resistance measurements, we can see that as a result of plasma treatment of the surface using a Helicon source, the thermal resistance of the interface of the Cu_n$_2$ sample with nanostructures was 20% lower than that of the untreated sample. The Cu_n$_3$ sample, whose surface was treated with a higher-energy plasma, showed a reduction in thermal resistance of only 10%. The thermal resistance of the Cu_n$_4$ sample, whose surface was treated with the same plasma as the Cu_n$_3$ sample but for twice as long, became even higher than that of the untreated Cu_n$_1$ sample.

3. Conclusions

Experiments conducted to study the effect of plasma treatment of copper using a Helicon source have established the following;

•There are copper treatment modes that allow nanostructures to be created on its surface;

•The nanostructures created on the copper surface reduce the thermal resistance of nanointerfaces;

•The surface roughness index cannot be unambiguously linked to the thermal resistance of the interface.

Acknowledgements

The research was partially supported by project No. 4.2/26-Р of the budget program of the NAS of Ukraine (КПКВК 6541230).

4. References

1. L. Vázquez, A. Redondo-Cubero, K. Lorenz, F. J. Palomares, R. Cuerno, J. Phys. Condens. Matter., **34** (33) (2022)
2. D. Pochan, O. Scherman, Chem. Rev. **121** (22): 13699 (2021)
3. W. Li, X. Zhan, X. Song, S. Si, R. Chen, J. Liu, Z. Wang, J. He, X. Xiao, Small, **15**, 31 (2019)
4. Jörn Bonse, Stephan Gräf, L. Photon. Rev. **14**, 10 (2020)
5. D. G. Cahill, P. V. Braun, G. Chen, D. R. Clarke, S. Fan, K. E. Goodson, P. Keblinski, W. P. King, G. D. Mahan, A. Majumdar, H. J. Maris, S. R. Phillpot, E. Pop, and L. Shi, Appl. Phys. Rev. **1**(1), 011305 (2014).
6. L. Shi, C. Dames, J. R. Lukes, P. Reddy, J. Duda, D. Cahill, J. Lee, A. Marconnet, K. E. Goodson, J.-H. Bahk, A. Shakouri, R. S. Prasher, J. Felts, W. P. King, B. Han, and J. C. Bischof, Nanoscale Microscale Thermophys. Eng. **19** (2), 127–165 (2015).
7. H. Fischer, Thermochim. Acta **425** (1–2), 69–74 (2005).
8. W. Park, A. Sooda, J. Park, M. Asheghi, R. Sinclair, K.E. Goodson, NANOSC MICROSC THERM, (2017)
9. F. Derya Ince, T. Özel, Surf. Coat. Technol., **498**, 131818 (2025)
10. F.F Chen, Plasma Sources Sci. Technol., **24** (2015)
11. S. Isayama, S. Shinohara, T. Hada, Plasma and Fusion Res., **13** (2018)
12. V.F. Semenyuk, V.F. Virko, I.V. Korotash, L.S. Osipov, D.Yu. Polotsky, E.M. Rudenko, V.M. Slobodyan, K.P.Shamrai, Probl. Atomic Sci. Technol. **179** (2013).
13. I.V. Korotash, V.V. Odinokov, G.Ya. Pavlov, D.Yu. Polotsky, E.M. Rudenko, V.F. Semenyuk, V.A. Sologub, K.P. Shamray. Nanoengineering,**4** (2012)
14. I.V. Korotash, V. Odinokov, G. Pavlov, D. Polotsky, E.M. Rudenko, V. Semenyuk, V. Sologub. Nanoindustry. **1** (2011)
15. BF. Semenyuk, E.M. Rudenko, I.V. Korotash, L.S. Osipov, et al. Metal Physics and Cutting-Edge Technologies. **33** (2011)
16. I.V. Korotash, V. Odynokov, G. Pavlov, et al. Nanoindustry, **4** (2010)
17. E.M. Rudenko, I.V. Korotash, et al. Science and Innovation, **6** (2010)
18. A. Shpak, E.M. Rudenko, I.V. Korotash, et al. Nanoindustry, **4** (2009)
19. E.M. Rudenko, I.V. Korotash, V. Semenyuk, K. Shamray. Science and Innovation, **5** (2009)
20. G.O. Veremeichenko, I.V. Korotash, E.M. Rudenko, et al. Ukrainian Patent № a 2010 15237 від 10.12.2010р.
21. I.V. Korotash, E.M. Rudenko, V.F. Semenyuk, and others. Ukrainian Patent № a 09554 (2010)

Influence of laser processing on the development peculiarities of cracks arising in the steels near non-metallic inclusions

Svetlana Gubenko
[1]Iron and Steel Institute of National Academy of Science of Ukraine,
[2]Ukrainian State University of Science and Technologies: Prydniprovska State Academy of Civil Engineering and Architecture; Aerospace Institute
Dnepr, Ukraine
sigubenko@gmail.com

Abstract. *The characteristics of crack growth near non-metallic inclusions under various loading conditions and the influence of laser treatment of steel on these processes are discussed. It is shown that crack development is accompanied by branching within fractured inclusions and in their clusters, as well as upon encountering structural defects in the steel matrix and dispersed second-phase particles. Conditions for crack growth inhibition associated with crack inhibition by plastic sulfides, the development of local relaxation processes in the steel matrix, and changes in the stress state are established. The influence of local microcomposite structures of the steel matrix, obtained under laser irradiation, on the inhibition of crack growth near non-metallic inclusions is demonstrated. The nature of crack growth near non-metallic inclusions was studied under various types of loading without laser irradiation and after preliminary laser treatment. Specimens of hot-rolled steel grades 08Al, 08Ti, 08, 08Cr18Ni10Ti, R7, M76, and GCr15 were subjected to tension and compression in vacuum at temperatures of 20…1200 °C using Instron-1195 and IMASH-9 units (grip movement speed of 1680 mm/min). Some steel specimens with polished surfaces were subjected to laser irradiation before deformation using GOS-30M and CVANT-16 units at pulse energy W_{imp} of 10…30 J. The heating rate was 10^5 °C/s, the pulse action time was (1.0…6.0).10^{-3} s, the cooling rate was 106 °C/s, and the radiation power density was 4 ·10^4 kW/cm^2.*

KEYWORDS: *LASER PROCESSING, STEEL, NON-METALLIC INCLUSIONS, PLASTIC DEFORMATION, CRACKS, DESTRUCTION.*

1.Introduction

It is known that non-metallic inclusions contribute to the embrittlement of steels, which leads to a decrease in their technological and operational properties [1 - 5]. The study of the conditions for the development of destructive cracks that occur near inclusions is relevant due to the need to improve the crack resistance of steels, as well as to increase the service life and reliability of structures and machine parts. Real steel products almost always operate with microcracks that occur for various reasons, including those near non-metallic inclusions. At a certain stage of the operation of structures and machine parts, subcritical growth of microcracks occurs near the inclusions (this stage of crack development is not dangerous). However, the second stage of uncontrolled avalanche crack growth (supercritical) is catastrophic. The transition from the first to the second stage is characterized by mechanical criteria [1, 2, 6]), while the physical processes underlying them are not entirely clear. Models of microcrack nucleation are described in works [1, 2, 4, 6]. It has been shown that the mechanism of crack initiation associated with non-metallic inclusions depends on the type of inclusions, their degree of plasticity, the level of cohesive strength of the inclusion-matrix boundaries, as well as the temperature, degree and rate of deformation [1, 2]. The transition to the second stage is associated with the nature of the stability of the system containing multiple microcracks associated with the inclusions, as well as the growth of one of the multiple microcracks by combining with others.

The goal of this study was to analyze the effect of laser treatment on the growth characteristics of cracks occurring in steels near non-metallic inclusions, as well as possible methods for inhibiting their growth.

2. Materials and Procedures.

The growth pattern of cracks occurring near non-metallic inclusions was studied under different types of loading without laser irradiation and after preliminary laser treatment. Specimens of hot-rolled steel grades 08Al, 08Ti, 08, 08Cr18Ni10Ti, R7, M76, and GCr15 were subjected to tension and compression in a vacuum at temperatures of 20–1200 °C using Instron-1195 and IMASH-9 units (grips moving at a speed of 1680 mm/min). Some steel specimens with polished surfaces were subjected to laser irradiation before deformation using GOS-30M and KVANT-16 units at pulse energy W of 10…30 J. The heating rate was 10^5 °C/s, the pulse action time was (1.0…6.0) 10^{-3} s, the cooling rate was 10^6 °C/s, and the radiation power density was 4 · 10^4 kW/cm^2. Metallographic studies were performed using a Neophot-31 microscope, a JSM-35 scanning electron microscope, and a Tesla transmission electron microscope. The phase composition of inclusions was determined by metallographic (Neophot–31) and petrographic methods [1], as well as by micro-X-ray spectral analysis using an MS-46 Cameca unit.

3. Results and discussion.

During plastic deformation at different temperatures, rates and deformation methods, defects arise near non-metallic inclusions: cracks in the steel matrix near the inclusion (Fig. 1, a); cavities (Fig. 1, b) or brittle delaminations along the inclusion-matrix interphase boundaries (corundum, spinels, some sulfides, Fig. 1, c); cracks in the inclusions themselves (titanium nitrides and carbonitrides, silicates, some sulfides, Fig. 1, d). The

Relaxation processes prolong the time interval of the subcritical stage of crack development near inclusions. The mechanism and parameters of defect nucleation near non-metallic inclusions can be influenced by the following methods: obtaining inclusions of a specific chemical and mineralogical composition features of crack initiation near inclusions are determined by the possibility of relaxation processes in the steel matrix or along the inclusion-matrix interphase boundaries, designed to reduce the level of stress concentration [1, 2, 7, 8]. The nature of the relaxation processes depends on the temperature and rate conditions of loading, the degree of plasticity of the non-metallic inclusions and the steel matrix, etc. [1, 2, 7, 8].

in the steel; changing the loading scheme and temperature-rate parameters; and the influence of preliminary treatment (annealing, laser irradiation) on the cohesive strength of inclusion-matrix interphase boundaries [1, 2, 9-13].

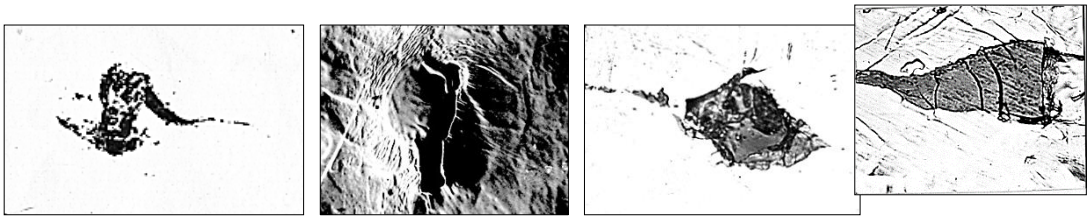

a b c d

Fig. 1. *Defects near inclusions (a - 08Ti, TiCN, hot rolling), (b - MnO. Al_2O_3, 08Al, tension, 900 °C, c - Al_2O_3, MnO. Al_2O_3, compression, 08Al, 900 °C), (d - 08, MnO SiO_2, tension, 25 °C); a - x500, b, c - x1000, d - x1200.*

The kinetics of crack development from inclusions in a steel matrix depends on loading conditions (temperature, degree and rate of deformation, stress pattern, cyclicity of the stress, crack initiation mechanism, chemical and phase composition of the steel, etc.). A crack from an inclusion can move intermittently, continuously (monotonically), or in an avalanche-like manner, depending on these conditions. Obviously, crack development can be affected by processes such as changes in the stress state, crack branching, and crack coalescence. It is necessary to ensure the ability to slow, arrest, and branch cracks associated with inclusions.

We will consider the processes that alter the conditions for crack development from non-metallic inclusions during steel deformation without preliminary laser irradiation. Important issues include identifying the conditions that suppress the continuous growth of these cracks (Fig. 2, a). A so-called "non-developming" crack can be inhibited by a ductile sulfide inclusion encountered along its growth path (Fig. 2, b) or by localized plastic relaxation processes in the steel matrix near the inclusion. A crack from an inclusion can develops into a nearby grain boundary, and depending on the deformation temperature, this process is either unaccompanied or accompanied by slipping along the grain boundary (Fig. 2, c, d). Stresses present in the developing crack bed relax into the grain boundaries. Slipping along the grain boundary is a relaxation process that ensures crack arrest. By the time the critical stage of fracture associated with the growth of the main crack occurs, the steel contains numerous microcracks associated with non-metallic inclusions.

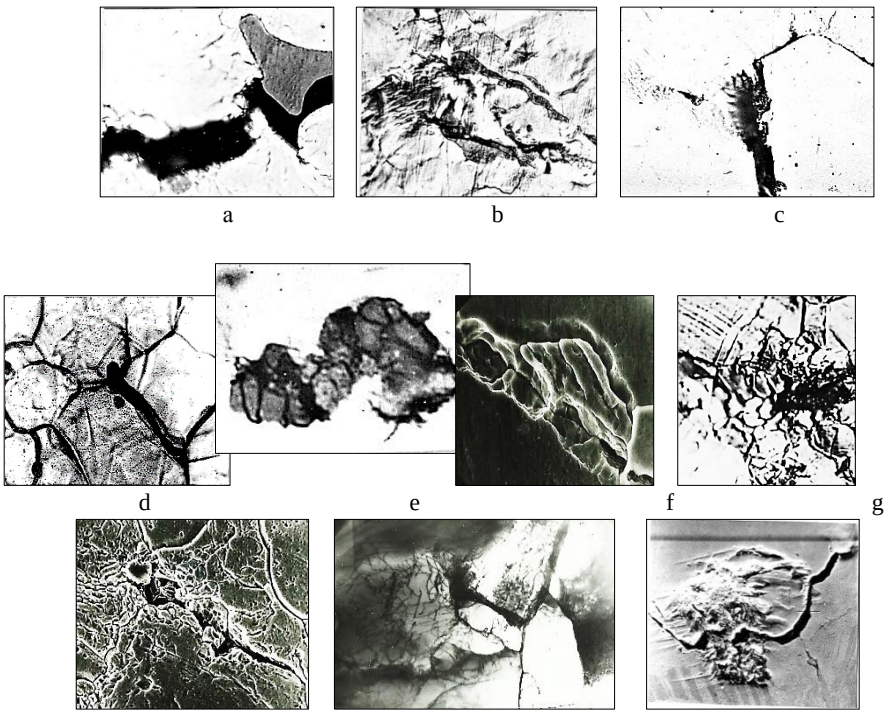

a b c

d e f g

h i j

Fig. 2. *Development of cracks from non-metallic inclusions in the steel matrix in different steels under different loading conditions without preliminary laser exposure: a – M76, FeS-(Fe, Mn)S, tensile stress 900 °C, ε = 25%; b, f – R7, (Fe,Mn)S, tensile stress 900 °C, ε = 22%; c – 08Ti, TiCN, tensile stress 600 °C, ε = 27%; d – 08Al, (Fe,Mn)S, tensile stress 1100 °C, ε = 25%; e – 08, MnO SiO_2, compression, 600 °C, ε = 27%; g, h – 08Cr18Ni10Ti, MnO SiO_2, tension 900 °C, ε = 21%; i - 08Cr18Ni10Ti, MnO SiO_2, tension 25 °C, ε = 11%; j – 08Al,.Al_2O_3, tension + compression, 1000 °C, ε = 15%; x900, and -x2000.*

The development of the main crack is accompanied by its branching and merging with other microcracks. Crack branching within the destroyed inclusions facilitates the localization of the fracture process without growth into the steel matrix (Fig. 2, e).

Branching of a growing crack leads to its inhibition and localization of the fracture process (Fig. 2, f). Crack branching is possible in a cluster of inclusions, when it encounters the grain boundary of the steel matrix, subboundaries of the cellular structure, and dispersed particles of the second phase (Fig. 2, g - i). When loading conditions change as a result of a change in the stress state pattern near the inclusion, various situations related to crack development are possible (branching, merging with other cracks, bending around inclusions, inhibition, change in growth direction, arrest) (Fig. 2, j). Crack branching is possible at high

development rates and in the presence of internal stresses (a growing crack "discharges" residual internal stresses, which disrupt its steady-state motion and alter its trajectory, determined by the external stress field) [6]. Internal stresses in steel can have various origins, including the presence of inclusions that cause instability in crack growth, which occurs when a certain critical growth rate is reached. Crack branching is associated with the breakdown of its elastic stress field.

Cracks coalesce when they develop from several non-metallic inclusions that merge by breaking the bridges between them. The main crack develops abruptly in zones of inclusion accumulation, where the elastic stress fields around individual particles and their microcracks disintegrate. If, prior to the appearance of the main crack, a balanced stress field existed from multiple inclusions, then with the appearance of a destructive crack, the stress system loses its equilibrium and additional energy is transferred to the growing crack [6]. Apparently, during the implementation of brittle fracture of steel, the release of elastic energy from each inclusion and its microcrack occurs and its transfer to the tip of the main crack has the characteristics of a chain process, in which the zone of stress equilibration from multiple inclusions that have lost their equilibrium plays an important role [6]. When plastic stress relaxation fields appear along the path of the main crack, the chain process of its development is interrupted and the nature of the steel fracture changes. The rate and mechanism of deformation of the steel matrix between microcracks, in so-called bridges [1, 2], play a key role, determining the moment of rupture and the nature of steel fracture. Bridges are located in zones of stress concentrators (inclusions, crack tips), where sharp localization of deformation occurs. Clearly, plastic processes slow the coalescence of microcracks and the growth of the main crack.

Uneven development (activity and depression) is observed both at the subcritical stage of microcrack growth and at the postcritical stage of main crack growth, depending on loading conditions, the number of non-metallic inclusions, and the structure of the steel matrix. The inhibition and cessation of microcrack growth near inclusions and the main crack are accompanied by localized plastic shear near these defects.

Branching and inhibition of cracks development from non-metallic inclusions is possible by creating special local structures in the steel matrix under preliminary laser irradiation. This irradiation results in interaction between the inclusions and the steel matrix, resulting in the formation of microcomposite zones of various types, characterized by chemical and phase heterogeneity [1, 9–12]. Alloying of localized areas of the steel matrix under conditions of anomalous mass transfer near the inclusions creates liquation-strengthened zones, which represent gradient and composite layers of various types: layered with cascade and "spotted" distribution of elements; spotted; dispersed with different types of strengthening phases; combined zones (Fig. 3, a, b).

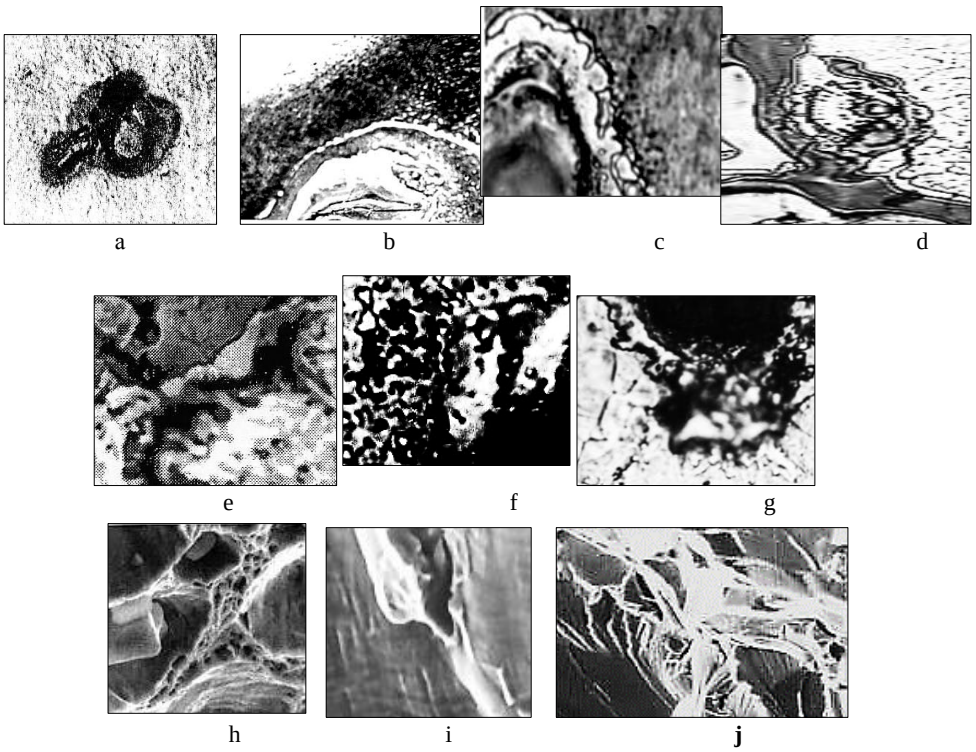

Fig. 3. *Microcomposite zones of the steel matrix near inclusions after laser treatment (a - R7, (Fe,Mn)O, b - M76, FeS–(Fe,Mn)S), and development of cracks from non-metallic inclusions in the steel matrix in various steels under different tensile deformation conditions after laser irradiation: c - R7, Al_2O_3, 1100 °C, ε = 8 %; d, e – 08Al, MnO SiO_2-FeO SiO_2, 600 °C. ε = 12 %; i - GCr15, MnO. Al_2O_3, 25 °C, ε = 15 %; f, j – 08Al, MnO SiO_2-FeO SiO_2, 1100 °C, ε = 12 %; g, h – 08Al, MnO. Al_2O_3, 1100 °C, ε = 16%; a, b -x900, c - j - x500x4.*

During subsequent deformation, these microcomposite zones facilitate changes in crack growth conditions due to a change in the direction of crack development associated with the transition from one layer to another or from one saturation ызще to another, which have different chemical compositions and, consequently, different strength and plastic properties. Crack growth from inclusions is slowed in zones of plastic stress relaxation, as well as due to the refinement of the grain structure of the steel matrix due to the development of high-speed laser recrystallization [1, 14].

In the areas of saturation of the gradient (cascade) type of steel matrix, a change in the direction of crack development occurred, associated with the transition from one layer to another (Fig. 3, c). This contributed to the bending and stepwise development of cracks, as well as the inhibition of their growth. In the areas of saturation of the spotted type of steel matrix, crack bending and even inhibition of their propagation were also observed (Fig. 3, d), which is associated with the different chemical composition, and, consequently, different strength and plastic properties of individual saturation "spots". In the areas of

saturation of the steel matrix with a dispersed composite structure, crack bending and inhibition of their growth were observed upon encountering dispersed "satellite" particles or inclusions crushed during high-speed laser melting [15, 16] (Fig. 3, e, f). Clearly, in these cases, the influence of stress fields near the dispersed particles is evident, interacting with the stress field in the bed of the growing crack. Finally, in areas of saturation of the steel matrix, which have a combined structure, crack bending and inhibition of their growth were also observed (Fig. 3, g). In these cases, the action of several factors is evident, related to the influence of stress distribution and differences in the chemical and phase composition of individual saturation zones [1, 9, 17].

Thus, it is possible to ensure the possibility of branching and changing the direction of crack growth, as well as slowing down or stopping their growth by creating special local structures of the steel matrix near inclusions as a result of preliminary laser treatment. Microcomposite liquation zones (cascade layered, spotted, dispersed, mixed type), which arise near inclusions, contribute to a change in the conditions of crack growth due to a change in the direction of their development associated with the transition from one section to another, having different chemical composition, strength and plastic properties. At the sites of such transitions along the path of crack development, zones of localized deformation and plastic relaxation arise (Fig. 3, h - j), slowing down their development. Obviously, relaxation processes are also facilitated by stresses in the indicated zones of saturation of the steel matrix, associated with the high-speed nature of mass transfer during laser exposure.

4. Conclusions.

The growth characteristics of cracks that occur near non-metallic inclusions are determined by the temperature conditions of loading, as well as the structure, phase composition, degree of ductility of the steel matrix, and the type of inclusion. Crack development is accompanied by branching within the fractured inclusions, in their clusters, upon encountering grain boundaries and subboundaries of the cellular structure of the steel matrix, and dispersed particles of the second phase. This ensures instability of crack growth, helps inhibit their development, and localizes the fracture process. Crack growth can be slowed by inhibition by ductile sulfide inclusions and the development of localized plastic relaxation processes in the steel matrix. Crack branching, crack direction change, and the inhibition or arrest of crack growth can be achieved by creating special localized structures in the steel matrix near non-metallic inclusions through preliminary laser irradiation. Microcomposite liquation zones (cascade layered, spotted, dispersed, mixed type), which arise near inclusions, contribute to a change in the conditions of crack growth due to a change in the direction of their development associated with the transition from one area to another, having different chemical composition, strength and plastic properties.

5. Literature.

1. Gubenko S.I., Oshkadepov S.P., Non-metallic inclusions in steel, Kiev, Naukova dumka, 2016. – 528 p.
2. Gubenko S.I. Non-metallic inclusions and strength of steel. – Saarbrücken: LAP LAMBERT. Palmarium academic publishing, 2015. - 476 p.
3. Sága M., Blatnická M., Blatnický M., Dižo J., Gerlici J., Research of the Fatigue Life of Welded Joints of High Strength Steel S960 QL Created Using Laser and Electron Beams. Materials (Basel, Switzerland), 2020, 03 Jun. 13(11).
4. André Luiz Vasconcellos daCosta e Silva, The effects of non-metallic inclusions on properties relevant to the performance of steel in structural and mechanical applications, Journal of Materials Research and Technology, 8 (2019), p. 2408-2422.
5. Qayyum F., Umar M., Elagin V., Kirschner M., Hoffmann F., Guk S., Prahl U. Influence of non-metallic inclusions on local deformation and damage behavior of modified 16MnCrS5 steel. Crystals, 2022, v. 12, No 2, p. 281-288.
6. Finkel V.M. Physics of Destruction. - M.: Metallurgy, 1970. - 376 p.
7. Gubenko Svetlana. Role of Inclusion – Matrix Steel Interphase Boundaries in the Development of Relaxation Processes near Nonmetallic Inclusions. Metal Science and Heat Treatment, 2020, v. 62, No 5, p. 299-305.
8. Gubenko S. Strucrural Effects near Nonmetallic Inclusions in Laser Treatment of Steels. Materials Science, 2000, v. 35, No 6, p. 818-827.
9. Gubenko S.I. Zones of contact interaction in steel matrix near inclusions under the laser action. Materials science. Jan 2011, 46 (4), p. 448-454 https://link.springer.com/article/ DOI:10.1007/s11003-011-9311-y
10. Gubenko SI. Analysis of the effect of nonmetallic inclusions on steel strengthening upon laser treatment. Steel in Translation, 2021, v.51, No 3, p. 217–228.
11. Gubenko S. Transformation of inclusions during laser processing of steels. v.1. Local strengthening. London - UK, Republic of Moldova - EU, Dodo Books abd OmniScriptum S.R.I. publishing group – Indian, LAP LAMBERT academic publishing, 2023. - 317 p.
12. Gubenko SI. Possibilities of transformation of non-metallic inclusions and interphase inclusion-matrix boundaries under high-energy treatments. Metal Physics. New Technologies, 2014. v. 36. No 3. p. 287-315.
13. Gubenko S. The Effect of High-Temperature Annealing on Microscopic Failure near Nonmetallic Inclusions in a Steel. The Physics of Metals and Metallography, 1995, v. 80, No 5, p.545-549.
14. Gubenko S. Specific features of stresses relaxation and recrystallization of steel under laser heating. Materials Science, 2023, v. 59, No 3, p. 267-74.
15. Gubenko S. I., Nikul'chenko I. A. Fragmentation of Nonmetallic Inclusions During Local Remelting upon Laser Steel Processing . Steel in Translation, 2020, v. 50, No. 3, p. 203-208.
16. Gubenko S. Melting and Crystallization of Nonmetallic Inclusions and Steel Matrix in the Course of Laser Treatment. Material Science, 2010, v. 46, issue 3, p. 365-371.
17. Gubenko S. Wave nature of the processes of high-speed mass transfer and local microalloying of laser-hardened steels. Material science. Nonequilibrium phase transformations, 2025, YEAR IX, issue 1(8), p. 14-17.

Complex-composition ceramics based on zirconium oxide for creating the latest thermal barrier coatings

Alina Makudera[1], Olena Dudnik[1], Serhii Lakyza[2]
Physical-chemistry and technology of refractory oxides department – Frantsevich Institute for Problems of Materials Science NAS of Ukraine[1]
ENSEMBLE3 Centre of Excellence, Warsaw, Poland[2]
a.makudera@ipms.kyiv.ua

Abstract: *For development of new materials with lower thermal conductivity and higher thermal stability than YSZ for the ceramic layer of thermal barrier coatings (TBC) was used hydrothermal nanodispersed ZrO_2 powder obtained at our Department and powder mixture of REE oxides of the yttrium subgroup (HC – heavy concentrate) with the following composition (wt.%): Y_2O_3 – 13.3; Tb_4O_7 – 1.22; Dy_2O_3-33.2; Ho_2O_3-8.9; Er_2O_3-21.8; Tm_2O_3-1.86; Yb_2O_3-12.5; Lu_2O_3-0.57; total content of other oxides – 6.65 (including Al_2O_3 – 3.2), which was formed during the production of apatite ores. The phase composition of the samples did not change after heat treatment at 1400 °C for 12 to 20 hours. The samples were two-phase: monoclinic phase ZrO_2 and cubic phase of fluorite type based on ZrO_2. This indicates that the samples are characterized by phase stability and are promising for creating a ceramic layer of TBP.*
Keywords*: REE OXIDES, NANODISPERSED POWDERS, TBC, PHASE STABILITY*

1. Introduction

Thermal barrier coatings (TBCs) are used to ensure long-term operation of gas turbine engines (GTEs) above the melting temperature of the superalloys from which their hot zone structural elements are made. Modern TBCs, which are applied to blades, consist of an inner heat-resistant metal layer and an outer ceramic layer, between which a transition layer of thermally grown aluminum oxide (TGO) grows during operation. The ceramic top coating provides thermal insulation of the surface and is usually composed of an oxide material with minimal thermal conductivity. The requirements for this material are as follows: low thermal conductivity <2 W/(mK); matching of the coefficient of thermal expansion (CTE) with the metal surface; absence of phase transformations between room and operating temperatures; resistance to sintering at high temperatures; erosion resistance [1], [2].

The most extensively studied and used material for the top layer of TBP is a solid solution based on ZrO_2 stabilized by 6-8 (wt. %) Y_2O_3 (YSZ), which is characterized by low thermal conductivity (2.1 W/m.K) and relatively high CTE ($11\cdot10^{-6}$/K), lack of interaction with Al_2O_3, heat resistance, high fracture toughness, and phase stability up to 1200 °C [3]-[5].

The development of new materials with lower thermal conductivity and higher thermal stability than YSZ for the ceramic layer of TBP is necessary to increase the service life of stationery and aviation gas turbine engines, since the operating temperature of the next generation of high-power gas turbine engines is expected to increase to 1500–1600 °C [4]. The search for next-generation materials is focused on three-, four-component and more complex oxide systems containing ZrO_2 and oxides of rare earth elements, the creation of high-entropy or complex-composition oxide ceramics based on medium-entropy (non-equimolar) compositions. Nanostructured coatings of complex composition are also being studied. For the microstructural design of the complex-composition ceramic layer of TBP based on ZrO_2, concentrates of REE oxides of natural origin, which are formed during the processing of apatite ores, are of interest. The simultaneous use of REE oxides, the cations of which have different sizes and valences, leads to the formation of a solid solution with a high degree of structural defects, which, in turn, provides low thermal conductivity of materials. In addition, the use of unseparated REE oxide concentrates for stabilizing ZrO_2 can significantly reduce the cost of the technological process for manufacturing a ceramic layer of TBP [6].

2. Starting materials

The study used hydrothermal nanocrystalline ZrO_2 powder obtained at our Department [19] and powder mixture of REE oxides of the yttrium subgroup (HC – heavy concentrate) with the following composition (wt.%): Y_2O_3 – 13.3; Tb_4O_7 – 1.22; Dy_2O_3-33.2; Ho_2O_3-8.9; Er_2O_3-21.8; Tm_2O_3-1.86; Yb_2O_3-12.5; Lu_2O_3-0.57; total content of other oxides – 6.65 (including Al_2O_3 – 3.2), which was formed during the production from apatite ores.

3. Experimental part

The physicochemical properties of the starting ZrO_2 powder, mixtures of REE oxides (HC) were determined and the compositions (wt. %) of 90 ZrO_2–10 HC, 80 ZrO_2 – 20 HC) and 70 ZrO_2–30 HC were established.

To produce complex-composition mixtures, ZrO_2 powders and REE oxides concentrate were blended in a laboratory ball mill in an isopropyl alcohol for 8 hours with ZrO_2 grinding bodies. After mixing, powders were dried in air in a SNOL 58/350 drying furnace at 80 °C for 10 hours. The heat treatment of these mixtures were carried out in a Nabertherm 08/17 furnace at 1400 °C for 12, 16 and 20 h in corundum crucibles.

The phase composition of the initial and complex-composition powders after different heat treatment times were studied by XRD phase analysis (Rigaku SmartLab 3kW Diffractometer (Rigaku Corporation, Tokyo, Japan) equipped with high-speed 1D silicon strip detector D/teX Ultra 250 and Cu Kα radiation.) The powder diffraction patterns were measured in reflection Bragg-Brentano geometry (θ/2θ scanning mode). The specific surface area of the powder was determined by the thermal nitrogen desorption (BET method) using a sorbtometer “EMS-61” (Estonia).

4. Results and Discussion

According to X-ray diffraction data, after annealing samples 90 ZrO_2 –10 HC; 80 ZrO_2 –20 HC; 70 ZrO_2 –30 HC at 1400 °C, 12 h, the formation of a mixture of 3 phases based on ZrO_2 was observed: monoclinic phase ZrO_2 (M-ZrO_2), T-ZrO_2 and F-ZrO_2 (see Fig. 1 – 3).

With an increase in the number of HC, the content of M-ZrO_2 in the samples decreased from 9.1 to 0.5%, the content of T-ZrO_2 also decreased from 76.7 to 16.7%, and the content of F-ZrO_2 increased from 14.2 to 82.8% (Table 1).

Increasing the isothermal holding time of ZrO_2 –10 HC samples to 16 hours leads to the formation of a mixture of two ZrO_2-based phases in them: M-ZrO_2 and F– ZrO_2. The content of M-ZrO_2 in the samples decreases from 76.7 to 5%, and F– ZrO_2 increases from

23.3 to 95% with an increase in the number of HC (see Fig. 3, Table 1).

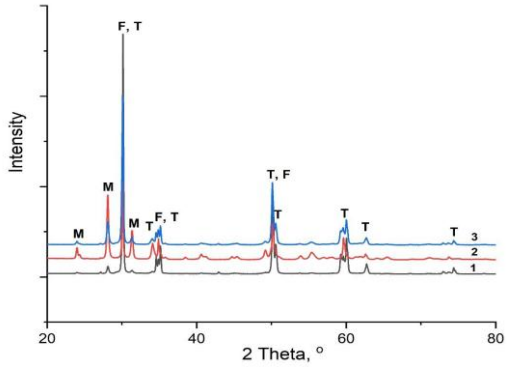

Fig. 1 *– X-ray diffraction patterns of 90 ZrO_2 –10 HC after heat treatment at 1400 °C: 1- 12 h., 2- 16 h., 3- 20 h.*

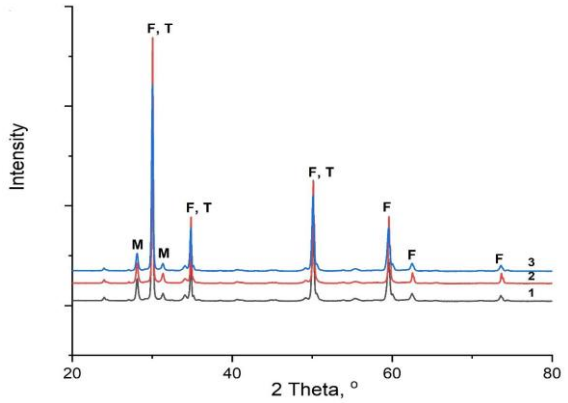

Fig. 2 *– X-ray diffraction patterns of 80 ZrO_2 –20 HC after heat treatment at 1400 °C: 1- 12 h., 2- 16 h., 3- 20 h.*

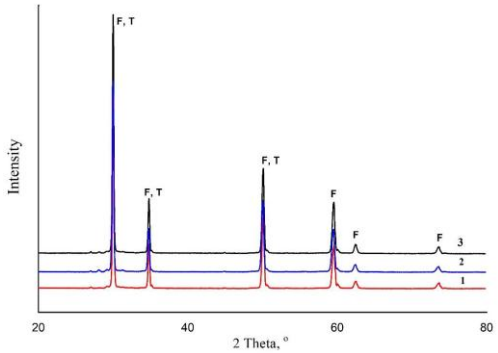

Fig. 3 *– X-ray diffraction patterns of 70 ZrO_2 –30 HC after heat treatment at 1400 °C: 1- 12 h., 2- 16 h., 3- 20 h.*

Table 1: *Quantitative analysis of crystalline phases of complex composite materials after heat treatment at 1400 °C.*

Composition, wt.%	Treatment time, h	M-ZrO_2	T-ZrO_2	F-ZrO_2
90 ZrO_2 – 10 HC	12	9,1	76,7	14,2
	16	76,7	-	24,05
	20	78,9	-	21,1
80 ZrO_2 – 20 HC	12	5,3	-	53,4
	16	33,4	-	70,7
	20	26,2	-	73,8
70 ZrO_2 – 30 HC	12	0,5	-	82,8
	16	5,0	-	95,0
	20	2,3	-	97,7

It is known that the parameters of ZrO_2-based substitutional solid solutions, which are the samples studied in this study, according to Vegard's rule, depend on the size of the substitutional cations. In our case, the sizes of the cations that are part of the alloying concentrate (HC) are larger than the size of the Zr^{4+} cation.

The average values of crystallites of the phases that make up the studied materials are given in Table 2. Data analysis shows that during the heat treatment of the ZrO_2 – HC samples at 1400 °C there is no significant increase in the crystallites size.

Table 2: *Quantitative analysis of crystalline phases of complex composite materials after heat treatment at 1400 °C.*

Composition, wt.%	Treatment time, h	M-ZrO_2	T-ZrO_2	F-ZrO_2
90 ZrO_2 – 10 HC	12	26	56	43
	16	27	-	42
	20	26	-	38
80 ZrO_2 – 20 HC	12	29	36	51
	16	36	-	41
	20	34	-	38
70 ZrO_2 – 30 HC	12	26	38	50
	16	15	-	40
	20	38	-	43

The relative density of materials after heat treatment at 1400 °C is shown in Fig. 4.

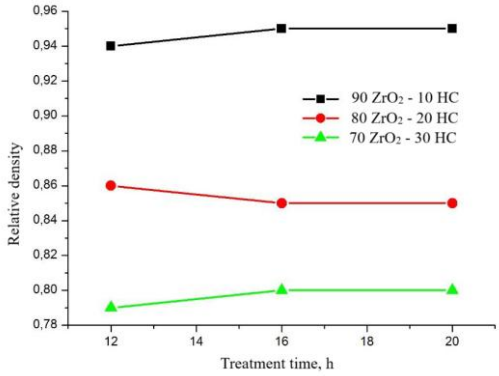

Fig. 2 *– Relative density of materials after heat treatment at 1400 °C.*

Increasing the isothermal holding time from 12 to 20 h causes almost no changes in the relative density values of material.

Thus, the holding time (12–20 h) at 1400 °C does not affect the sintering of complex composite materials ZrO_2–HC.

According to the results of X-ray diffraction, it can be concluded that the processes of phase formation in the ZrO_2 – HC materials are influenced by the HC content and the treatment time in isothermal conditions at 1400 °C.

Increasing the treatment time to 20 hours for all samples did not change the phase composition of the material. The samples were two-phase: monoclinic phase ZrO_2 and cubic phase of fluorite type based on ZrO_2. This indicates that the samples reached an equilibrium and stable state.

5. Conclusion

During heat treatment at 1400 °C, increasing the isothermal holding time practically does not affect the relative density of ZrO_2 – HC materials and the size of crystallites of individual phases. This indicates the absence of intensive sintering of complex – composite materials ZrO_2 – HC under experimental conditions, regardless of the HC content.

Thus, it is complex-composite ZrO_2 – HC materials at 1400 °C meet the requirements of phase stability and absence of sintering imposed on the ceramic layer of TBC.

6. References

1. Th. S. Hille, Th. J. Nijdam, A. S. J. Suiker, S. Turteltaub, W. G. Sloof, Acta Mater. **57**. 2624–2630. (2009)
2. V. Kumar, B. Kandasubramanian, Particuology. **27**. 1–28. (2016)
3. K. Masera, A. K. Hossain, J. of the Energy Inst. **92**. 783−80. (2019)
4. R. Vaßen, M. Ophelia Jarligo, T. Steinke, D. Em. Mack, D. Stöver, Surf. Coat. Technol. **205**. 938–942. (2010)
5. Az. D. Johari, The 3rd national graduate conference, universiti tenaga nasional, putrajaya campus. 8−9. (2015)
6. B. Liu, Y. Liu, Ch. Zhu, H. Xiang, H. Chen, L. Sun, Y. Gao, Y. Zhou, J. of Materials Science & Technology, **35(**5). 833−851. (2019)

Nanostructuring of brass surface by helicon source plasma

E. Rudenko[1], I. Korotash[1], D. Polotskiy[1], A. Rudenko[1], V. Dekhtyarenko[1], and M. Dyakin[1*]
G.V. Kurdyumov Institute for Metal Physics of the N.A.S. of Ukraine[1]
max@imp.kiev.ua

Abstract: *The influence of helicon discharge plasma flows on the surface of CuZn37 brass was investigated. Technological parameters of ion-plasma processes, in which the synthesis of zinc oxide ZnO nanocrystallites occurs, were determined. The synthesized hierarchical formations of ZnO can be a transitional gradient layer for the subsequent application of protective coatings on the surface of brass. The presence of such an intermediate ZnO layer will contribute to improving the matching of the physicochemical properties of the substrate and the coating, reducing interfacial stresses and increasing the adhesion strength of the formed multilayer system.*

Keywords: *HELICON SOURCE PLASMA, BRASS, ZnO, ADHESION RESISTANCE OF COATING*

Introduction

The controlled creation of ordered nanostructures on the surface of various types of materials, such as semiconductors, dielectrics, polymers, and especially metals, has long been of great interest to scientists [1–3]. This directed creation of relief and structures on the surface with characteristic dimensions from units to hundreds of nanometers has significantly expanded the functional capabilities of devices made from such materials [4–5]. The properties of micro- and nanoobjects with one- (1D), two- (2D) or three-dimensional (3D) nanostructures are determined by: chemical composition; dimensions; shape; ordering of molecules; nature of intermolecular interactions. Such nanoobjects have found wide application in many fields of science and technology, in particular, in various new electronic devices. This is due to the emergence of self-organization effects, which make it possible to create functional structures with predetermined electrical, optical, mechanical and chemical characteristics [6–8].

It is known that when treating the surface of a solid in energy flows (laser, electron, ion irradiation), the formation of hierarchical submicron structures with nanorelief is possible [9-11]. The nanostructural component is of crucial importance, since it determines the basic properties at the level of surface chemical bonds. The physical factors that determine the origin and development of ordered surface structures are very diverse, due to the competition of many destabilizing and stabilizing physical processes. That is why researchers are particularly interested in the physicochemical processes that create the corresponding nanostructures [12].

The **aim** of this work was to establish the effect of helicon discharge plasma flows on the surface of CuZn37 brass and to determine the technological parameters for the synthesis of hierarchical structures on it.

Materials and experimental procedure

The work used industrial sheet brass CuZn37 with a thickness of 1.5 mm, from which rectangular samples measuring 50 mm x 30 mm were made. The samples constituted a complex system of structures of hot and cold-deformed brass sheet with a complex stress field, an uneven texture in the rolling direction and perpendicular to it, with a non-uniform structure of the density of defects caused by plastic deformation [13,14].

To ensure surface cleanliness, the samples were first cleaned mechanically and then treated in an ultrasonic bath in gasoline and alcohol. The general scheme of the experimental setup is described in detail in [15,16].

The samples were placed in a vacuum chamber on a technological table-substrate holder, which was electrically insulated from the installation body. In most experiments, a bias potential of up to U_t= -(100–300) V, sometimes up to -400 V, was applied to the table. This made it possible to regulate the energy of ions bombarding the substrate surface. This made it possible to regulate the energy of ions bombarding the substrate surface. Pure argon or argon with the addition of oxygen were used as working gases to form the technological plasma. A substrate holder table with a diameter of Ø48 mm, on which a brass substrate was fixed, was placed in the center of the vacuum chamber. Accelerated argon plasma flows from a helicon-type plasma source were directed at it. The temperature of the substrate holder table was measured using a thermocouple. Since the sample was tightly pressed to the substrate-holding table and has a fairly high thermal conductivity, it can be assumed that the temperature of the processed surface of the CuZn37 sample is equal to that measured by the thermocouple.

During the experiment, such technological parameters as the value of the ion current on the substrate-holding table I_t and the power supplied to the high-frequency plasma generator P were constantly monitored. The uniformity of the plasma flux density of argon plasma from the source over the larger sample size i_t was no worse than ± 0.5%. The technological parameters of sample processing are given in Table 1. Where U_t is the voltage supplied to the substrate-holding table, I_t is the ion current supplied to the substrate-holding table, P is the power of the plasma generator supplied to the sample, i_t is the ion current density, t – is the plasma processing time.

Table 1: *Technological parameters of sample processing.*

Technological process	U_t, V	I_t, mA	P, W	I_t, mA/cm^2	t, *min.*	Pressure, Pa
CuZn-10	-100	100 - 105	10-10,5	5,50	10	$5\cdot10^{-2}$
CuZn-45	-100	100-110	10-10,1	5,52	45	$5\cdot10^{-2}$

The surface morphology of the substrate and its elemental composition were investigated using a TESCAN MIRA 3 scanning electron microscope equipped with an Oxford Instruments X-max 80 mm^2 energy dispersive spectrometer. The elemental composition was investigated integrally in the field of view of the microscope (300x300 μm) and locally with a corresponding reduction in the field of study.

Results and discussion

The samples were treated for 10 and 45 minutes at the same pressure of 0.67 Pa and voltage U_t on the substrate holder table of -100 V. The ion current density was about 5.52 mA/cm^2. After the samples were treated with helicon discharge plasma, their surface was analyzed using a scanning electron microscope. The microstructure of the surface of CuZn37 brass without helicon plasma treatment is shown in Fig. 1.

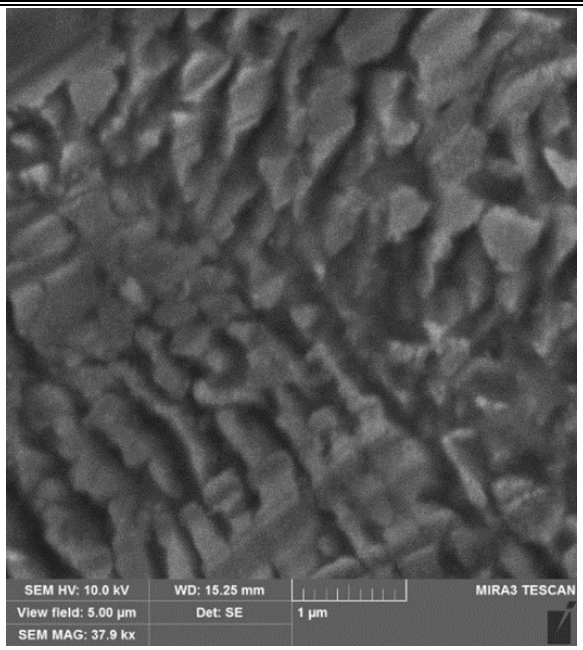

Fig. 1 *Surface microstructure of CuZn37 brass without helicon plasma treatment.*

Figure 1 shows that the classical initial state of the surface of CuZn37 brass without helicon plasma treatment has a pronounced three-dimensional relief with elongated, irregular, wrinkled and folded ridges. In addition, there are signs of texture in the rolling direction and shallow breaks in the surface layers, which may be a consequence of cold deformation of the last rolling passes during hot rolling of brass. The structures have a characteristic transverse size mainly in the range of 0.2–1 µm. The surface has a labyrinthine appearance with a folded, with clear protrusions and depressions on which there are residues of carbon and oxygen that are inevitably formed from rolling oils or emulsions during cold and hot rolling of brass.

A feature of the helicon discharge is the high density of the ion current and the energy of the ions, which leads to significant differences in the surface sputtering from other types of vacuum discharges (smoldering, magnetron, arc, high-frequency). When sputtering a metal surface with any ion current, two stages of this process can be distinguished. First, as a result of ion bombardment of the initial surface, the highest points of the relief (ridges) begin to be sputtered, on which the maximum density of the negative charge supplied to the brass substrate is concentrated. These ridges are subjected to the strongest sputtering due to the maximum plasma concentration at the peaks, as a result of which their height decreases, the degree of purity increases and the surface relief is smoothed, which corresponds to ~▼12, i.e. a high level of polishing. Thus, this ion treatment mode smoothes surface irregularities by sputtering the protruding peaks. This produces a large number of small, light nanoparticles with a predominantly rounded shape, evenly distributed over the surface with a size within 10–50 nm (some may be slightly larger or smaller). The results of the study of the brass surface after treatment in an ion stream for 10 min indicate a significant change in the elemental composition of the substrate surface. The amount of carbon and oxygen on the substrate surface decreased significantly, but the surface was not completely cleaned of impurities, which indicates insufficient bombardment time and energy.

The microstructure of the surface of CuZn37 brass after treatment with a helicon discharge plasma with an ion energy of about 100 eV is presented in Fig. 2.

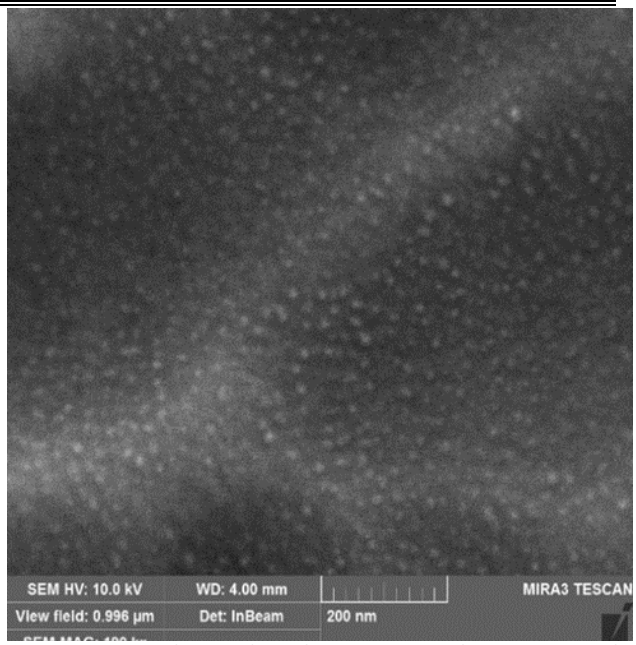

Fig. 2 *Microstructure of the surface of CuZn37 brass after 10 minutes of treatment with helicon discharge plasma with ion energy of about 100 eV.*

With further intensive processing of the brass surface (second stage) for 45 min, its appearance changed dramatically (Fig. 3). The surface became as smooth as possible as a result of spraying high ridges, as the process of selective local spraying began, the coefficient of which is determined by the characteristics of the phase components of the metal. Different phases have different spraying coefficients, due to which, over time, a relief begins to form on the surface again, which differs from the previous one. Figure 3 shows that the surface is almost completely covered with densely packed rounded (spheroidal) particles with a size of mainly 30-60 nm. The particles have an uneven, granular surface and are collected in large clusters. The boundaries of the sample grains are clearly visible between the clusters, which become more and more clearly visible with increasing annealing time (the sample temperature increases during longer processing), and even the sizes of the selected structural elements – fragmented islands – on the surface increase. The elemental composition of this surface also changed, namely, the amount of copper, zinc, and carbon on the surface decreased slightly, but the oxygen content increased approximately twice.

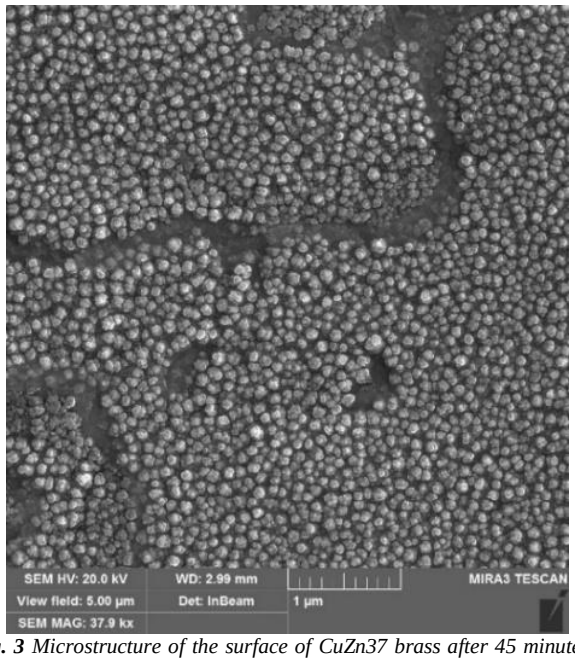

Fig. 3 *Microstructure of the surface of CuZn37 brass after 45 minutes of treatment with helicon discharge plasma with ion energy of about 100 eV.*

As a result of the treatment of the CuZn37 brass substrate with helicon plasma for 45 min. a developed, nanostructured, impurity-free surface was formed, on which three-dimensional hierarchical ZnO formations appeared. These hierarchical formations are randomly oriented nanorods up to several microns long, similar to the highly oriented 3D ZnO nanostructures obtained by the authors [17] as a result of solution deposition. Confirmation of the presence of nanostructured ZnO on the brass surface was made using Raman scattering spectra. The physics of the formation and growth of these nanostructures is complex and multilevel. Previously [18] their synthesis was carried out at relatively high oxygen pressures (~ 30 MPa) and without preliminary plasma preparation. When using the combined treatment modes proposed by us, it was possible to do this more easily. First of all, the brass surface was cleaned and activated by plasma argon flows. Secondly, by independent heating of the prepared samples in an oxygen atmosphere (pressure ~ 10^{-2} Pa). As a result, perfect ZnO nanorods were synthesized on the brass surface, due to the diffusion of zinc atoms from the inside of the lattice to its surface.

Thus, the resulting surface appearance of the brass substrate is determined by the entire complex set of physicochemical processes occurring under the action of helicon plasma. The formed ZnO nanocrystallites create a developed relief and can serve as a transitional gradient layer when applying protective coatings (metals, oxides, ceramics, polymers [19]) to brass, which flow around them and mechanically engage, which dramatically increases adhesion. In addition, many protective coatings differ greatly in thermal expansion coefficient, elastic modulus and chemical nature from brass, and the ZnO layer must compensate for the difference in properties, thereby smoothing this transition and reducing internal stresses.

The increase in the adhesion strength of the protective coating due to plasma treatment of the brass substrate was shown by us in previous studies [20], taking into account the entire set of theories developed so far.

So, the main advantage of the plasma helicon discharge is the ability to easily control its parameters, and therefore the ability to sputter. That is, it is possible to select the optimal sputtering mode, in which the surface relief will have a columnar nanostructure with dimensions of 50-200 nm.

Conclusions

As a result of the conducted research, the influence of ion treatment on the surface of CuZn37 brass in the plasma flow of a helicon discharge was established. Technological regimes were determined under which effective surface sputtering and formation of a developed nanostructured, impurity-free brass surface with ordered three-dimensional hierarchical formations of ZnO occur. Synthesized ZnO nanocrystallites can perform the function of a transitional gradient layer for the subsequent application of protective coatings to the surface of brass previously treated in a helicon discharge. The presence of such an intermediate layer can contribute to improving the matching of the physicochemical properties of the substrate and the coating, reducing interfacial stresses and increasing the adhesion strength of the formed multilayer system.

Acknowledgements

The research was partially supported by project No. 4.2/26-P of the budget program of the NAS of Ukraine (КПКВК 6541230).

Refrences

1. Frédéric Wiame, Thin Solid Films, **642** (2017), DOI:10.1016/j.tsf.2017.09.026
2. Hannah-Noa Barad, Hyunah Kwon, Mariana Alarcón-Correa, Peer Fischer, ACS Nano., **15** (2021), DOI: 10.1021/acsnano.0c09999
3. M.S. Jawad, W. Ur Rahman, M. Khan, A. M. Faysal, Next Materials, **10** (2026), https://doi.org/10.1016/j.nxmate.2025.101422
4. Naumih M. Noah, J. of Nanomat., **1** (2020), https://doi.org/10.1155/2020/8855321
5. Q. Zhang, E. Uchaker, S. L. Candelaria, G. Cao, Soc. Rev., **42** (2013), DOI:10.1039/c3cs00009e
6. L. Sosa-Vargas, E. Kim, A. André-Jean, Mater. Horiz., **4** (2017), DOI: 10.1039/C7MH00127D
7. D. Pochan, O. Scherman, Chem. Rev., **121** (2021), DOI:10.1021/acs.chemrev.1c00884
8. R. K. Joshi, J. J. Schneider, Chem. Soc. Rev., **41** (15): (2012), https://doi.org/10.1039/c2cs35089k
9. A. Keller, S. Facsko, Materials (Basel), **22** (2010), DOI:10.3390/ma3104811
10. L. Vázquez, A. Redondo-Cubero, K. Lorenz, F. J. Palomares, R. Cuerno, J. Phys. Condens. Matter., **34** (2022),), DOI 10.1088/1361-648X/ac75a1
11. W. Li, X. Zhan, X. Song, S. Si, R. Chen, J. Liu, Z. Wang, J. He, X. Xiao, Small, **15**, (2019), https://doi.org/10.1002/smll.201901820
12. Jörn Bonse, Stephan Gräf, L. Photon. Rev., **14** (2020), https://doi.org/10.1002/lpor.202000215
13. ISO 197-1:1983. Copper and copper alloys — Terms and definitions — Part 1: Materials
14. ISO 2624:1990. Copper and copper alloys — Estimation of average grain size
15. E. M. Rudenko, V. Ye. Panarin, P. O. Kyrychok, M. Ye. Svavilnyi, I. V. Korotash, O. O. Palyukh, D. Yu. Polotskyi, and R. L. Trishchuk, Progr. Phys. Met., **20** (2019), DOI: 10.15407/ufm.20.03.485
16. E.M. Rudenko, I.V. Korotash, M.V.Dyakin, D.Yu. Polotskiy, S.A. Bespalov, O.V. Hamalii, N.V.Hamalii, V.A. and Dekhtyarenko, Progr. Phys. Met., **27** (2026), DOI: 10.15407/ufm.27.02.194
17. L. Schmidt-Mende, J. L. MacManus-Driscoll, Materials Today, **10** (2007), DOI: 10.1016/S1369-7021(07)70078-0
18. Lu Yuan, C. Wang, R. Cai, Y. Wang, G. Zhou, J. Appl. Phys., **114** (2013), DOI: 10.1063/1.4812569
19. V.A. Dekhtyarenko, T.V. Pryadko, O.I. Boshko, V.V., Kirilchuk H.Yu. Mykhailova, and V.I. Bondarchuk, Progr. Phys. Met.,, **25** (2024), DOI:10.15407/ufm.25.02.276
20. E. Rudenko, M. Svavilnyi, T. Kyrychok, D. Polotsky, A. Novytska, V. Panarin, S. Bespalov, Vacuum, **238** (2025), DOI: 10.1016/j.vacuum.2025.11422

Ultrafast bond softening and non-thermal phase dynamics in femtosecond-excited diamond

Tzveta Apostolova[1,2]
[1]Institute for Nuclear Research and Nuclear Energy , Bulgarian Academy of Sciences, Bulgaria
[2]Institute for Advanced Physical Sciences, New Bulgarian University, Bulgaria
E-mail: tzveta.apostolova@nbu.bg

Abstract: *This work presents a first-principles theoretical investigation into the ultrafast non-equilibrium dynamics, optical breakdown, and structural response of bulk diamond irradiated by intense 12-fs laser pulses with 400 nm wavelength. By modeling transient electron density dynamics, energy deposition, internal electric fields, and transient dielectric functions, we map the microscopic pathways leading to ultrafast non-thermal phase transitions and surface patterning. For low intensities, photoinoziation of diamond follows the predictions of the perturbative non-linear optics, and a qualitative change of the electron dynamics occurs when the laser intensity increases above* $5 \times 10^{14}\ W/cm^2$. *We find that in this high intensity regime, laser energy absorption is enhanced due to excitation of bulk plasmon resonance. The electron density difference distribution shows the effect of softening of C-C bonds: the charge density in the binding region is not sufficient to balance the nuclear repulsion forces, resulting in instability of the diamond lattice.*

Keywords: DIAMOND, FEMTOSECOND LASER EXCITATION, BOND SOFTENING, NONTHERMAL STRUCTURING.

1. Introduction

The interaction of intense femtosecond laser pulses with wide-bandgap solids has revolutionized precision micro- and nano-fabrication, offering unprecedented control over surface morphology, optical properties, and local phase composition [1–3]. Among dielectric materials, diamond occupies a unique position owing to its ultra-wide bandgap (5.47 eV), high mechanical hardness, chemical inertness, and exceptional thermal conductivity [4]. These extreme physical properties make diamond notoriously difficult to machine via conventional thermal techniques. However, ultrashort laser irradiation bypasses traditional thermal processing, enabling localized, sub-diffraction surface nano structuring and sub-surface phase transformations [5, 6].

The hallmark of femtosecond laser-dielectric interactions is the complete temporal decoupling between electronic excitation and lattice motion. Because the laser pulse duration $\tau_p < 50\ fs$ is significantly shorter than the typical electron-phonon relaxation time (τ_e-ph ~ 1–10 ps), energy deposition is confined exclusively to the electronic subsystem [7]. In wide-bandgap materials, non-linear photoionization (multiphoton and tunnel ionization) promotes a significant number of electrons $N_e \sim 10^{21} cm^{-3} - 10^{22} cm^{-3}$ from localized bonding valence states into delocalized, antibonding conduction bands. This rapid redistribution of electronic charge drastically alters the interatomic potential energy surface (PES) on a sub-100 fs timescale, long before thermal energy can transfer to the lattice [8].

Historically, theoretical descriptions of ultrafast laser-dielectric phenomena have been fragmented into specialized, single-purpose models. On one hand, solid-to-solid non-thermal phase transitions such as the rapid sp³ → sp² graphitization of diamond have been treated using phenomenological potential surface flattening models or bond-charge depletion schemes [9, 10]. On the other hand, macroscopic surface nanostructuring, such as Laser-Induced Periodic Surface Structure (LIPSS) formation, has been analyzed predominantly via classical electromagnetic models incorporating empirical Drude parameters for free-carrier optical permittivity [11, 12]..

In this work 1) we establish the precise transition from multiphoton excitation to state-filling saturation for laser polarization along two crystal orientations, 2) we map transient dielectric properties and establish the criteria for surface plasmon polariton (SPP) format

ion, 3) we predict Laser induced periodic surface structure (LIPSS) periodicity and 4) we evaluate microscopic electronic pressure that soften interatomic force constants and drive non-thermal sp³ → sp² graphitization via Transverse Optical (TO) phonon instability.

2. Methodology

Because the position operator r̂ is unbounded across periodic crystal boundaries, we describe the non-perturbative excitation of the electronic subsystem using the Time-Dependent Schrödinger Equation (TDSE) formulated in the velocity gauge:

$$i\partial_t \left|\psi_{n\vec{k}}(\vec{r},t)\right\rangle = \frac{1}{2}\left(-i\vec{\nabla} + \vec{A}(t)\right)^2 \left|\psi_{n\vec{k}}(\vec{r},t)\right\rangle, \quad (1)$$

where the Bloch wavefunction is expressed via the cell-periodic Bloch function

$$\psi_{n\vec{k}}(\vec{r},t) = e^{i\vec{k}.\vec{r}} u_{n\vec{k}}(\vec{r},t)\ , \quad u_{n\vec{k}}(\vec{r}+\vec{R},t) = u_{n\vec{k}}(\vec{r},t) \text{ with}$$

$$|u_{n\vec{k}}(0)\rangle = |u_{n\vec{k}}\rangle = \sum_{\vec{G}} c_n(\vec{G}+\vec{k})|G+k\rangle$$

which are the initially occupied Bloch states in the valence band of the crystal, $\vec{G}$ label the reciprocal lattice wave-vectors, n is the band index, $\vec{k}$ is the crystal momentum in the first Brillouin zone (BZ) and $c_n(\vec{G}+\vec{k})$ are the plane-wave expansion coefficient of the electronic Bloch wave function in band n at crystal momentum $\vec{k}$ and reciprocal lattice vector $\vec{G}$ .The laser vector potential is $\vec{A}(t) = \vec{A}_{ext}(t) + \vec{A}_{ind}(t)$, $\vec{E}(t) = \partial\vec{A} / \partial t$ with

$$\frac{d^2}{dt^2} A_{ind}(t) = 4\pi J(t)$$

and crystal periodic potential

$$V(\vec{r}) = V(\vec{r}+\vec{R}), \quad V = V_{Hartree} + V_{xc} + V_{e-ion}, \quad V_{e-ion}(\vec{r}) = \sum_{G} V(\vec{G}) \cos\left(\vec{G}.\vec{\tau}\right) e^{i\vec{G}\cdot\vec{r}}$$

(2)

Here, $\vec{A}_{ext}$ is the applied laser vector potential, $\vec{A}_{ind}$ is the induced laser vector potential, $V(\vec{r})$ is the unperturbed periodic pseudopotential of the diamond latticeV_H, and V_{xc} are the exchange and correlation contributions respectively and atomic units are used ($e = \hbar = m_e = 1$) where e is the elementary charge, and m_e is the electron mass. In the empirical pseudopotential method used, the periodic ionic lattice potential is expressed by a plane wave-expansion in the basis of reciprocal lattice wave-vectors. In Eq. (2)

$\vec{\tau} = \frac{a_0}{8}(1,1,1)$, $V(G^2 = 3) = -0.625Ry$,

$V(G^2 = 8) = 0.051Ry$ and $V(G^2 = 11) = 0.206Ry$ are the relative vector connecting two diamond atoms and the pseudopotential form factors, respectively. The transient occupation numbers are defined as:

$$f_{n\vec{k}}(t) = \sum_{m\in occ} \left|\left\langle u_{n\vec{k}} | u_{m\vec{k}}(t)\right\rangle\right|^2$$

and the transient electron density is

$$n_e(t) = \sum_{n\in occ}^{\infty} \int_{BZ} \frac{d^3k}{(2\pi)^3} f_{n\vec{k}}(t)$$

The instantaneous one-electron density matrix at each k is constructed from the initially occupied propagated orbitals**:**

$$f_{n\vec{k}}(0) = 1$$

$$\hat{\rho}_{\vec{k}}(t) = \sum_n f_{n\vec{k}}(0)\left|\psi_{n\vec{k}}(\vec{r},t)\right\rangle \left\langle\psi_{n\vec{k}}(\vec{r},t)\right|$$

where for fully occupied valence bands

The electronic charge-current density is:

$$\vec{J}(t) = Tr[\hat{\rho}(t)\hat{v}] = \sum_{n\in occ}\int_{BZ}\frac{d^3\mathrm{k}}{4\pi^3}\left\langle\psi_{n\vec{k}}(t)\,|\,\hat{p}+\vec{A}(t)\,|\psi_{n\vec{k}}(t)\right\rangle,\ \left(\vec{J}=d\vec{P}/dt\right)$$

where $\vec{v}(t) = \vec{p} + \vec{A}(t)$ is the velocity operator. The absorbed energy is defined as:

$$E_{abs}(t) = \int^{t} dt' E(t')\cdot J(t')$$

The profile of the laser pulse and the laser fluence are defined as follows:

$$\vec{E}_{ext}(t) = \vec{e}\exp[-\ln 4(t-t_0)^2/\tau^2]F\sin(\omega_L t),$$

$$I = F^2,\ \Phi = I\tau$$

When the propagated orbitals are expanded in the basis of the ground-state Bloch states the non-equilibrium density matrix is obtained:

$$\rho_{mn}\left(\vec{k},t\right) = \left\langle\psi_{n\vec{k}}(t)\middle|\psi_{m\vec{k}}(t)\right\rangle$$

After the laser pulse, $\vec{A}_{ext}\left(t_f\right) = 0$ and we denote the calculated density matrix of the photoexcited electron-hole plasma with $\rho_0 = \rho\left(t_f\right)$ and calculate the optical response of the excited system. The Hamiltonian is written as:

$$\hat{H}(t) = \hat{H}_0 + \hat{V}(t)$$

In velocity gauge the interaction with the self-induced vector potential is small relative to the crystal Hamiltonian $\hat{H}_0$ and is treated as a weak perturbation of the strongly non-equilibrium state generated by the pump pulse.

$$\hat{V}(t) = \vec{A}_{ind}\,.\vec{p}$$

The density matrix is written as $\rho\ (t) = \rho_0 \quad + \delta\rho\ (t)$ where ρ_0 is the excited state and $\delta\rho$ is the response to the weak field. The Liouville–von Neumann equation is solved in linear response approximation, (in the basis of eigen functions).

$$i\frac{d\delta\rho}{dt} = \left[\hat{H}_0\,,\delta\rho\right] + \left[\,\hat{V},\rho_0\right]$$

.The unperturbed density matrix contains diagonal populations $f_{n\vec{k}}$ and off-diagonal interband coherences $\omega_{nm\vec{k}}$. Because interband coherences involve rapidly oscillating phase factors $e^{-i\omega_{nm\vec{k}}}$, they average out to zero. Taking the Fourier transform of the equation of motion for $\delta\rho$

$\delta\rho_{nm,\vec{k}}(\omega) = \frac{\left(f_{m,\vec{k}}-f_{n,\vec{k}}\right)V_{nm,\vec{k}}(\omega)}{\omega-\omega_{nm,\vec{k}}}$ and the induced current is obtained from

$$\delta J(\omega) = -Tr[\delta\rho(\omega)\,,\hat{v}]$$

$$= \sum_{mn}\int_{BZ}\frac{d^3k}{4\pi^3}(p_\alpha)_{nm\vec{k}}\delta\rho_{nm,\vec{k}}(\omega) - \frac{n_0}{i\omega}E_\alpha(\omega)$$

where $(p_\alpha)_{nm\vec{k}} = \left\langle n_{n\vec{k}}\,|\hat{p}_\alpha|\,n_{m\vec{k}}\right\rangle$ is the matrix element of the momentum operator along the α Cartesian direction that measures the transition dipole moment connecting band n to band m at point $\vec{k}$ in the Brillouin zone, and determines the strength of optically induced electronic transitions along direction α. Substituting $V_{nm,\vec{k}}(\omega) = \frac{1}{i\omega}\vec{E}(\omega).\vec{p}_{nm\vec{k}} = \frac{1}{i\omega}\sum_\beta\left(p_\beta\right)_{nm\vec{k}}E_\beta(\omega)$ into eq. the relation is obtained $J_\alpha(\omega) = \sigma_{\alpha\beta}E_\beta(\omega)$ and since electric current density and electric polarization are related in the frequency the linear susceptibility tensor is determined from the relation $P_\alpha(\omega) = \chi_{\alpha\beta}(\omega)E_\beta(\omega)$ and hence the dielectric tensor is written as: $\varepsilon_{\alpha\beta} = \delta_{\alpha\beta} + 4\pi\chi_{\alpha\beta}$. Assuming weak optical anisotropy the final expression for the dielectric function becomes:

$$\varepsilon(\omega) = \frac{1}{3}tr\varepsilon(\omega) = \left(1-\frac{\omega_p^2}{\omega^2}\right) + \frac{4\pi}{3}tr\left[\frac{1}{\Omega}\sum_{nmk}\frac{f_{nk}-f_{mk}}{\omega_{nm}^2(\mathrm{k})[\omega_{mn}(\mathrm{k})-\omega]}(p_\alpha)_{nmk}(p_\beta)_{mnk}\right]$$

$$\omega_p^2 = -\frac{4\pi}{3}tr\left[-\frac{1}{\Omega}\sum_{nk}f_{nk}\left[\frac{\delta_{\alpha\beta}}{m} - \sum_{m\neq n,k}\frac{[(p_\alpha)_{nmk}(p_\beta)_{mnk}+(p_\alpha)_{mnk}(p_\beta)_{nmk}]}{\omega_{nm}^2(\mathrm{k})}\right]_{\alpha\beta}\right]$$

where Ω is volume of the unit cell. Using the real part of the dielectric function we determine the condition for plasmon polariton formation in the photoexcited diamond.

Following ref [] we define next the macroscopic stress tensor

$$\mathrm{T}_{\alpha\beta} = -\sum_{n,\mathrm{k},\mathrm{G}}|c_n(\mathrm{k}+\mathrm{G})|^2(\mathrm{k}+\mathrm{G})_\alpha(\mathrm{k}+\mathrm{G})_\beta + 2\pi\sum_{\mathrm{G}\neq 0}|n(\mathrm{G})|^2/G^2(2\mathrm{G}_\alpha\mathrm{G}_\beta/G^2-\delta_{\alpha\beta}) -$$

$$-\sum_{\mathrm{G}\neq 0}S(\mathrm{G})[\partial V_{loc}(G)/\partial G^2 2\mathrm{G}_\alpha\mathrm{G}_\beta + V_{loc}(G)\delta_{\alpha\beta}]n(-\mathrm{G}) +$$

$$+\delta_{\alpha\beta}\sum_{\mathrm{G}}[\varepsilon_{xc}^{LDA}(\mathrm{G}) - \mu_{xc}^{LDA}(\mathrm{G})]n(-\mathrm{G}) - \delta_{\alpha\beta}\Omega_{u.c.}^{-1}\alpha_1 Z + \sigma_{\alpha\beta}^{(Ewald)}$$

where $n(\vec{G}) = \sum_{n,\vec{G}',\vec{k}} f_{n\mathrm{k}}^0 c_n^*(\vec{k}+\vec{G}'-\vec{G})c_n(\mathrm{k}+\vec{G}')$ is the Fourier transform of the real-space electron density in the crystal describing how the electronic charge is distributed periodically throughout the crystal lattice and $S(\vec{\mathrm{G}})$ is the form factor . The real-space electronic charge density $\rho(\vec{r}) = \sum_{\vec{\mathrm{G}}} n(\mathrm{G})\ e^{-i\vec{G}.\vec{r}}$ is obtained via the Fourier transform of $n(\vec{G})$. The first term in eq. () is the Electronic Kinetic Stress since it represents Quantum mechanical momentum flux of the electrons. The second term is the Hartree Electrostatic Stress arising from long-range electron-electron Coulomb repulsion. The third term represents the stress generated by electron-ion electrostatics between conduction/valence electrons and atomic cores, where V_{loc} is the local component of the ionic pseudopotential in reciprocal space and the derivative of the pseudopotential with respect to momentum transfer squared captures energy changes under strain. Last two terms describe exchange-correlation stress and classical ion-ion Coulomb stress tensor computed via Ewald summation, representing interatomic repulsive forces between positive atomic nuclei in the diamond lattice. Then the pressure is defined as:

$$p = -\frac{1}{3}tr\mathrm{T} = \frac{1}{3}\sum_{\mathrm{v},\mathrm{G}}\int_{BZ}\frac{d^3\vec{k}}{4\pi^3}\left(\left|c_{\mathrm{v},\vec{\mathrm{k}}+\vec{\mathrm{G}}}\right|^2 - \left|c_{\mathrm{v},\vec{\mathrm{k}}+\vec{\mathrm{G}}}^0\right|^2\right)(\vec{\mathrm{G}}+\vec{\mathrm{k}})^2$$

3. Results and Discussion

In Fig. 1 (a) the first Brillouin zone of the face-centered cubic (FCC) diamond structure is a truncated octahedron with high-symmetry points (Γ, L, X, W, K, U) and symmetry axes (Δ along $[001]$, Λ along $[111]$, and Σ along $[110]$). In Fig. 1 (b) the electronic energy band dispersion of unperturbed crystalline diamond that provides the fundamental quantum mechanical framework for calculating optical transitions and high-intensity carrier dynamics is shown. The valence band maximum (VBM) is located at the zone center $\Gamma_{25'}$, set at 0 eV. The conduction band minimum (CBM) lies along the Δ axis (Δ_1 branch) near the X_1 boundary, yielding an indirect bandgap of $5.42eV$. Under the dipole approximation, direct interband optical transitions require conservation of quasi-momentum. The minimal direct transition

threshold occurs at the Γ point between $\Gamma_{25'}$, and $\Gamma_{2,}$, requiring a photon energy of 7 eV to create an electron-hole pair without phonon assistance.

Fig. 2 displays the calculated real-time dynamics of the transmitted electric field $\vec{E}(t)$ inside bulk diamond during and after irradiation by the laser pulse linearly polarized along the [001] direction across three distinct coupling regimes. The weak coupling regime with $\Phi = 1.2\ J/cm^2$, 2 (a), shows a symmetric, undistorted pulse envelope peaking at $\sim 0.55\ V/$Å. Because photo-induced carrier generation is low in this perturbative regime, the medium's response remains largely linear, leaving the laser field profile unperturbed without significant internal polarization screening. Therefore, we can calculate the static dielectric constant of diamond in this regime. In the transition to strong coupling regime with $\Phi = 7.2\ J/cm^2$, 2 (b), as the peak field reaches $\sim 2.0\ V/$Å, intense non-linear photoionization generates a dense conduction plasma. The induced polarization current produces a counter-directed screening field, causing a subtle temporal asymmetry in the field envelope as electronic screening begins to modify the propagating wave. Fig. 2 (c) illustrates extreme strong coupling, with $\Phi = 60\ J/cm^2$ where the field peaks near $\sim 2.5\ V/$Å early in the pulse due to rapid, carrier excitation before the pulse peak that creates a high-density plasma. The resulting large induced current $\vec{J}(t)$ strongly distorts the driving laser field, shifting the peak field forward in time and suppressing field amplitudes in the trailing edge of the. Persistent low-amplitude electric field oscillations remain after the main laser pulse passes, directly capturing coherent collective plasma oscillations (plasmons).

Fig. 3 displays the calculated real-time dynamics of the electron number density in diamond during and immediately after irradiation by a $12\ fs,\ 400\ nm$ laser pulse. Panel (a) shows excitation with linear polarization along the [001] direction, while Panel (b) shows polarization along the [111] direction. During the laser pulse, the carrier density exhibits strong intra-pulse oscillations at twice the laser frequency, reflecting non-linear sub-cycle field ionization and interband virtual excitations. In the low fluence $\Phi = 2.4 - 3.6\ J/cm^2$ regime carrier generation proceeds via perturbative multiphoton excitation, reaching a modest transient density $n_e \approx 1.5 \times 10^{22}\ cm^{-3}$. In the high fluence regime $\Phi = 6 - 12\ J/cm^2$ highly non-linear ionization rapidly elevates the conduction electron density between $n_e \approx 6 \times 10^{22}\ cm^{-3} - 8 \times 10^{22}\ cm^{-3}$. At these extreme densities, state-filling (Pauli blocking in conduction bands) and strong electronic screening lead to a saturation of net carrier generation. Following the pulse, high-frequency field oscillations die out, leaving a stable, residual electron-hole plasma $n_e > 3 \times 10^{22}\ cm^{-3}$ for $\Phi = 6\ J/cm^2$ and $n_e > 4 \times 10^{22}\ cm^{-3}$ for $\Phi = 12\ J/cm^2$. Comparing Figs. 3 (a) and (b) demonstrates subtle anisotropic excitation kinetics. For identical fluences $\Phi = 12\ J/cm^2$, polarization along [001] (a) drives steeper sub-cycle peak oscillations during the pulse envelope than along [111] (b), reflecting the orientation of $C - C$ bonds relative to the driving electric field vector. The carrier density $n_e \sim 4 \times 10^{22}\ cm^{-3}$ generated at high fluences exceeds $15\% - 17\%$ of the total valence electron density n_0, crossing the critical threshold $n_C = n_0/\epsilon_0$ required to trigger transverse acoustic phonon softening and complete lattice collapse following the simple criterion $\omega_{TA}^2(n_e) = \omega_{TA,0}^2\left(1 - \epsilon_0 \frac{n_C}{n_0}\right)$ in which $\omega_{TA}(n_e)$ is the frequency of the transverse acoustic phonon mode as a function of the photo-excited carrier density n_e, $\omega_{TA,0}$ is the ground-state transverse acoustic phonon frequency, ϵ_0 is the static bulk dielectric constant of diamond ~ 5.7 and n_0 is the total bulk valence electron density.

Fig. 4 illustrates the time-dependent instantaneous electronic excitation energy per atom $(eV/atom)$ transferred from the laser pulse into the bulk of diamond, comparing polarization along [001] (a) and [111] (b) across varying fluence. Energy absorption rises rapidly on the rising part of the laser pulse featuring high frequency oscillations corresponding to sub-cycle field interactions. After the peak of the pulse, the absorption curves flatten , indicating that energy transfer strongly decreases leaving excitation energy stored within the electronic system. For low fluence $\Phi = 6\ J/cm^2$ the absorbed energy is $(\sim 3.5 - 4.0\ eV/atom)$. For moderate fluence $\Phi = 12\ J/cm^2$ the absorbed energy is $(\sim 5.0 - 5.5\ eV/atom)$ and in the high fluence regime $\Phi = 60\ J/cm^2$ the absorption saturates for $(\sim 8.0 - 9.5\ eV/atom)$. The thermal melting energy of diamond is $0.33\ eV/atom$ and its bulk cohesive energy is $\sim 7.37\ eV/atom$. Across all shown fluences, the energy deposited into the electronic subsystem substantially exceeds the thermal melting energy and, at high fluences, surpasses the cohesive energy of the lattice. The comparison between the two laser polarization directions reveals that for polarization along the [001] direction – Fig. 4 (a), drives higher net energy absorption at each fluence level, reaching $\sim 4.0\ eV/atom$ at $6\ J/cm^2$, $\sim 5.5\ eV/atom$ at $12\ J/cm^2$ and $\sim 9.5\ eV/atom$ at $60\ J/cm^2$. Polarization along the [111] direction Fig. 4 (b), exhibits slightly reduced absorption efficiency ($\sim 3.3\ eV/atom$ at $6\ J/cm^2$, $\sim 4.5\ eV/atom$ at $12\ J/cm^2$ and $\sim 7.8\ eV/atom$ at $60\ J/cm^2$, reflecting laser polarization anisotropy in the energy absorption.

Fig. 5 presents the laser fluence dependence of the generated conduction electron density n_e and the absorbed energy per carbon atom E_{abs} $(eV/atom)$ on logarithmic scales. Fig. 5 (a) and Fig. 5 (b) correspond to linear polarization along [001], while panels Fig. 5 (c) and Fig. 5 (d) correspond to polarization along [111]. At low fluences below $\sim 3.5\ J/cm^2$, the carrier density grows rapidly according to $n_e \propto \Phi^3$ for both polarizations. This cubic power law indicates a non-linear multiphoton excitation mechanism dominating the initial band-to-band transitions. Near $\Phi \sim 4.0\ J/cm^2$, n_e undergoes an abrupt vertical jump spanning nearly an order of magnitude (crossing $10^{22}\ cm^{-3}$). This step marks the optical breakdown threshold.
Above $\Phi \sim 25\ J/cm^2$, carrier generation severely slows down, following a sub-linear power law $n_e \propto \Phi^{1/3}$. This sub-linear scaling reflects strong conduction-band state filling (Pauli blocking) and high-density plasma screening that suppresses further ionization.

In Fig. 5 (b) and Fig. 5 (d), the absorbed energy per atom at high fluences scales as $E_{abs} \propto \Phi^{1/2}$ which directly reflects the heating dynamics of the degenerate photo-excited plasma. Melting Threshold: The horizontal dashed line in (b) and (d) mark the thermal melting energy of diamond 0.33 $eV/atom$. For fluences exceeding $\Phi \sim 2.5\ J/cm^2$, the absorbed electronic energy significantly exceeds this baseline, driving the system into the non-thermal phase transition regime.

Comparing Fig. 5 (a, b) with Fig. 5 (c, d) shows that the power-law exponents $v = 3, v = 0.33$, $v = 0.5$ are polarization-independent. However, polarization along [111] (Fig. 5 c, d) exhibits a slightly lower breakdown threshold fluence than along [001], demonstrating direction-dependent non-linear absorption coefficients.

Fig. 6 displays the calculated energy distribution of occupied conduction electronic states $\rho(\varepsilon, \Phi)$ per unit cell for two laser pulse durations $12\ fs$ and $30\ fs$ across low (Fig. 6 a, b) and high (Fig. 6 c, d) fluence regimes. At lower fluence, photo-induced carriers predominantly occupy low-lying conduction states $(\varepsilon < 4\ eV)$, producing distinct peaks around $0.5\ eV$ and $2.0\ eV$. Comparing results for $12\ fs$ (a) to $30\ fs$ (b) shows progressive population accumulation in higher states up to $14\ eV$ as multiphoton absorption and conduction band energy absorption proceed. In the regime of strong coupling, conduction states are filled across a broad energy window stretching beyond $25\ eV$, displaying major peaks near $3\ eV$ and $7\ eV$. As the lower conduction band states become fully populated, state-filling severely restricts further transition matrix elements from the valence band. This Pauli blocking mechanism causes the saturation of photo-ionization seen at high fluences, forcing newly promoted carriers into higher kinetic

energy states $(\varepsilon > 10\,eV)$ and driving the sub-linear scaling laws $n_e \propto \Phi^{1/3}$, and $E_{abs} \propto \Phi^{1/2}$.

In Fig. 7 the modification of the dielectric constant in photoexcited diamond following the irradiation by a $30\,fs$, $400\,nm$ is presented. In Fig. 8 left panel (a) and (b) the intensity-dependent dielectric response for laser polarization along [001] direction is shown. In Fig. 8 left panel (a) $Re[\epsilon(\omega)]$ exhibits characteristic dielectric behavior with positive values in the sub-bandgap region $(\omega < 3\,eV)$ at low excitation intensity (solid black curve). As the laser intensity increases (progressing from red dashed to blue and green dotted curves), a sharp Drude-like metallic crossover emerges: $Re[\epsilon(\omega)]$ becomes strongly negative below $\sim 2\,eV$, dropping down to -25 at $1\,eV$. This negative divergence directly is a signature of free-carrier plasma formation and non-thermal metallization of the diamond crystal.

Surface plasmon polariton (SPP) excitation at the interface between the photo-induced metallic surface layer and vacuum $(\epsilon = 1)$ requires the real part of the frequency-dependent complex dielectric function $\epsilon\,(\omega_L) = Re\,[\epsilon\,(\omega_L)] + iIm\,[\epsilon\,(\omega_L)]$ to satisfy the condition $Re\,[\epsilon\,(\omega_L)] < -1$. The spatial period of the resulting low-spatial frequency laser-induced periodic surface structures Λ_{LIPSS} is governed by the SPP dispersion relation $\Lambda_{LIPSS} = \lambda_L / Re\left[\sqrt{\epsilon\,(\omega_L)/(\epsilon\,(\omega_L)+1)}\right]$, where λ_L is the incident laser wavelength and $\epsilon\,(\omega_L)$ is evaluated directly from the calculated dielectric spectrum at the driving photon energy. For our laser wavelength $400\,nm$, $\omega_L = 3.1\,eV$ taking from Fig. 7 $Re\,[\epsilon\,(\omega_L)] \sim -8$ and $Im\,[\epsilon\,(\omega_L)] \sim 1$ gives an SPP factor of ~ 1.07, resulting in a calculated period of $\Lambda_{LIPSS} \sim 374\,nm$ or $\sim 0.94\,\lambda_L$.

In Fig. 7 left panel (b) $Im\,[\epsilon(\omega)]$ is plotted. The ground-state fundamental interband absorption edge remains prominent near $\omega \approx 4.2\,eV$. With increasing laser intensity, the peak absorption amplitude diminishes due to state-filling (Pauli blocking in valence states), while substantial spectral weight transfers into the low-energy Drude absorption tail $(\omega < 3\,eV)$, indicating efficient intraband absorption by photo-excited free carriers.

In Fig. 7 - right panel (a) and (b) - the intensity -dependent dielectric response for laser polarization along [001] and [111] directions is shown to demonstrate polarization anisotropy. In Fig. 8, right panel (a) $Re[\epsilon(\omega)]$ is exhibited. Comparing the response along the [001] direction (solid black curve) and [111] direction (red dashed curve) highlights a strong optical anisotropy. Excitation along the [111] axis causes a significantly faster breakdown of dielectric screening, with $Re[\epsilon(\omega)]$ crossing zero at higher photon energy $\sim 1.5\,eV$ and diving steeper into negative values ≈ -20 at $0.8\,eV$. This indicates that alignment along the $C-C$ bonding direction enhances photoionization and free-carrier production.

In Fig. 7 right panel (b) $Im[\epsilon(\omega)]$ is exhibited. The [111] orientation (red dashed curve) exhibits greater low-energy intraband absorption $(\omega < 3\,eV)$ compared to [001], while suppressing the primary interband absorption peak at $\omega \approx 4.2\,eV$ more effectively. This confirms a higher depletion of bonding valence electrons along the [111] $C-C$ bond axis, leading to stronger electronic screening and faster non-thermal bond softening.

In fig. 8 shows the spatial distribution of valence charge in unperturbed diamond that provides the baseline for understanding ultra-fast photo-excitation and non-thermal bond softening. The contour plot displays the ground-state electron number density ρ_0 mapped in the 110 crystallographic plane. High-density regions (intense red contours exceeding $0.4\,a.u.$ are localized directly along the $C-C$ bond axes at the midpoints between carbon nuclei, demonstrating the strong covalent sp^3 bonding character. Under a local pseudopotential formulation, the mid-bond charge displays closed, elliptic density contour lines whose major (long) axes orient perpendicular to the primary bonding direction. This structural topology reflects the spatial symmetry of the overlapping valence orbitals in the diamond lattice. Because ground-state stability relies on these concentrated mid-bond charge distribution, any subsequent laser-induced photoionization that depletes ρ_0 from these regions by transferring electrons into non-bonding or anti-bonding interstitial sites (green background, $\rho_0 \sim 0.1\,a.u.$) directly scales down the effective bond charge Z_b that screens nuclear repulsion and destabilizes the lattice. Here $Z_b(n_e) = Z_{b,0}\left(1 - \epsilon_0 \frac{n_e}{n_0}\right)$ where $Z_{b,0}$ is the ground-state effective bond charge of the unperturbed lattice. Ground-state bond charge is $Z_{b,0} = 2/\epsilon_0$.

In the dielectric screening model of photo-excited covalent crystals, both the transverse acoustic phonon frequency $\omega_{TA}^2(n_e)$ and the effective bond charge $Z_b(n_e)$ depend directly on the screening of covalent bonds by the photo-generated carrier gas (expression for $\omega_{TA}^2(n_e)$ was given in the discussion of Fig. 3). Because the transverse restoring forces in sp^3 covalent crystals originate directly from the localized bond charge Z_b in the mid-bond region, the square of the phonon frequency scales with the effective bond charge:

$$\omega_{TA}^2(n_e) \propto Z_b(n_e)$$

When n_e reaches the critical threshold $n_e^{crit} = n_0/\epsilon_0$ the effective bond charge $Z_b(n_e)$ vanishes $Z_b \to 0$, representing complete electronic depletion of the directional bonding nodes. The restoring force for transverse shear modes vanishes simultaneously $\omega_{TA}^2(n_e) \leq 0$, causing complete mode softening and non-thermal lattice collapse.

Fig. 9 maps the spatial electron density difference $\Delta\rho(\vec{r}) = \rho(\vec{r}) - \rho_0(\vec{r})$ in the 110 plane following the irradiation by a $12\,fs, 400\,nm$ laser pulse linearly polarized along the 001 direction. The charge depletion at $C-C$ mid-bonds is clearly seen: deep blue regions centered along the horizontal bonding chain correspond to negative difference contours ($\Delta\rho(\vec{r}) < 0$, dotted lines down to -0.02 a.u.). This confirms that intense photoionization directly strips valence electrons out of the localized sp^3covalent mid-bond sites. The interstitial accumulation is observed as well: yellow-green background areas represent positive difference contours ($\Delta\rho(\vec{r}) > 0$, solid lines). Promoted electrons transfer into non-bonding and interstitial anti-bonding regions surrounding the $C-C$ bonds, generating an uncompensated electronic pressure. Intensity scaling is provided in the two panels of Fig. 10. In Fig. 10 (a) the laser intensity is $6 \times 10^{14}\ W/cm^2$ and moderate charge depletion localized primarily at the bond midpoints (blue pockets reaching $\approx -0.015\,a.u.$ is exhibited. In Fig. 10 (b) for the higher intensity $10^{15}\ W/cm^2$,the blue depletion nodes expand radially and deepen (surpassing $-0.02\,a.u$). This stronger depletion weakens the directional restoring forces of the $C-C$ bonds, driving the transverse acoustic (TA) phonon frequency toward zero ($\omega_{TA}^2 < 0$) and setting off non-thermal lattice collapse.

Fig. 10 presents the calculated laser intensity I dependence of the photo-induced pressure p (in $kbar$) in crystalline diamond following irradiation by a $12\,fs, 400\,nm$ laser pulse linearly polarized along the [001] direction. For laser intensities below $4 \times 10^{14}\ W/cm^2$, the photo-induced pressure remains low $(p < kbar)$, indicating a low electron-hole pair excitation density in the perturbative ionization regime. At $I \approx 4 \times 10^{14}\ W/cm^2$, an abrupt step-like increase of the pressure occurs, with pressure $p > 400\,kbar$. This rapid rise marks the optical breakdown threshold, where strong non-linear photoionization promotes a dense plasma of carriers into conduction states.

For above-threshold intensities ($I \approx 4 \times 10^{14}\ W/cm^2$) , the pressure increases sub-linearly with intensity, closely following the scaling law $p \propto\approx I^{5/9}$ and reaching values over $600\,kbar$ at $I \approx 1 \times 10^{15}\ W/cm^2$. Because carrier density in the breakdown regime scales sub-linearly as $n_c \propto\approx I^{1/3}$ due to state filling and Pauli blocking, combining the two scaling laws we have obtained from our calculation - $n_c \propto\approx I^{1/3}$ with $p \propto\approx I^{5/9}$ yields the standard Fermi pressure scaling law for a degenerate electron gas:

$p \propto\approx I^{5/3}$. Over 80% of this photo-induced pressure stems from the kinetic energy of the hot electron subsystem. At pressures approaching $600\,kbar$ $(60\,GPa)$, this uncompensated outward Fermi pressure exceeds the elastic yield strength of the diamond crystal, driving shear destabilization and non-thermal lattice collapse on sub-picosecond timescales.

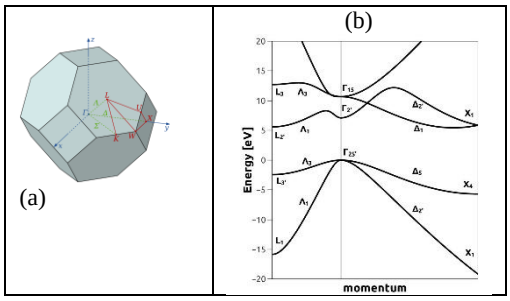

Fig. 1 *(a) Brillouin zone of diamond lattice (b) Electronic energy bands of diamond along Δ and Λ symmetry lines.*

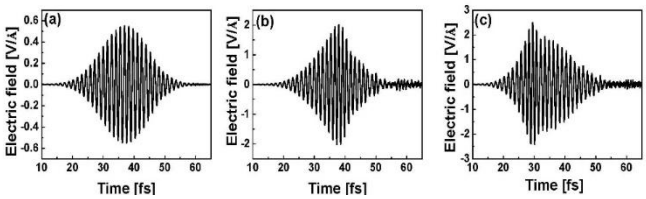

Fig. 2. *Time evolution of the electric field in bulk diamond irradiated by pulsed laser with pulse width 12 fs and wavelength 400 nm.The laser is linearly polarized along the [001] direction. The laser fluence is (a) 1.2 J/cm^2, (b) 7.2 J/cm^2, (b) 60 J/cm^2*

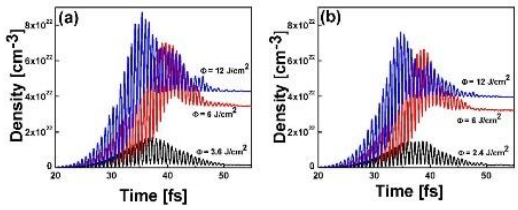

Fig. 3. *Time evolution of the electron number density (12fs, 400 nm) , the laser fluence is indicated in the figures. Figure 3 (a) the laser is polarized in [001] direction. Figure 3(b) the laser is polarized in [111] direction.*

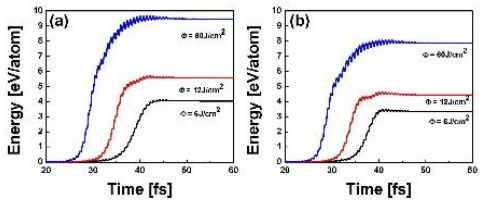

Fig. 4. *Instantaneous electronic excitation energy (12fs, 400 nm), the laser fluence is indicated in the figures. Figure 4 (a) the laser is polarized in [001] direction. Figure 4 (b) the laser is polarized in [111] direction. The melting energy of diamond is 0.33 eV/atom. The cohesive energy of diamond is 7.37 eV/atom.*

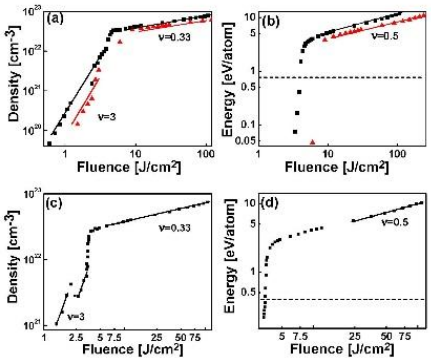

Fig. 5. *Fluence dependence of the conduction electron density (in cm^{-3}) (a) , (c) and the absorbed energy per carbon atom (in eV) (a) , (c) in bulk diamond irradiated by a pulsed laser with wavelength of 800 nm and duration 12fs. The laser is linearly polarized along the [001] direction in (a), (b) and along [111] direction in (c), (d). The dashed lines in (b), (d) indicate the melting energy of diamond.*

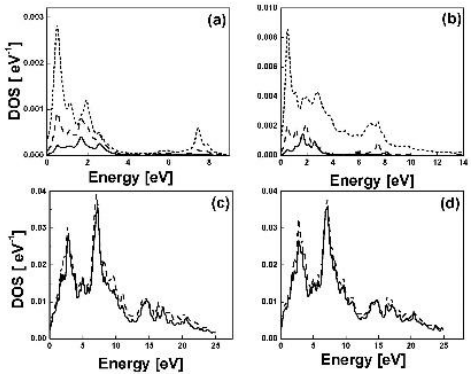

Fig. 6. *Density of conduction states (per unit cell) for two different coupling regimes*

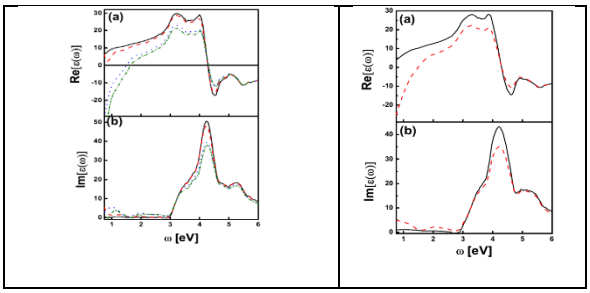

Fig. 7. *Intensity-Dependent Dielectric Response of diamond for increasing laser intensity - left panel (a) and (b): laser polarization along [001] direction and right panel (a) and (b): laser polarization along [111] direction*

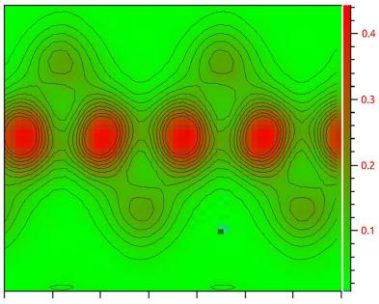

Fig. 8. Contour plot of the electron number density in the (110) plane in diamond ground state. The contour interval is 0.01 a.u. The laser is linearly polarized along the [001] direction

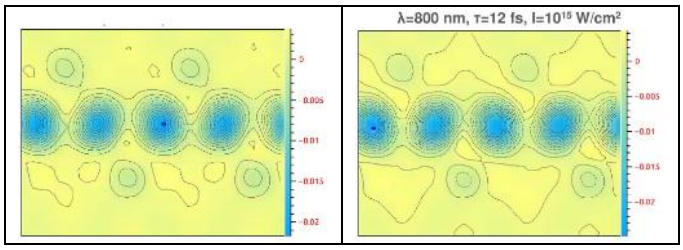

Fig. 9. Local density difference map $\rho(\vec{r}) - \rho_0(\vec{r})$ after irradiation of diamond with laser pulse of duration is 12 fs, and wavelength 400 nm. The laser intensity is $6 \times 10^{14}\ W/cm^2$ (a) and $10^{15}\ W/cm^2$ (b). The laser is linearly polarized along the [001] direction. Negative contours associated with depletion of charge are indicated by dotted lines and positive contours associated with charge accumulation are indicated by solid lines. The contour interval is 0.005 a.u. C-C bonds are softened

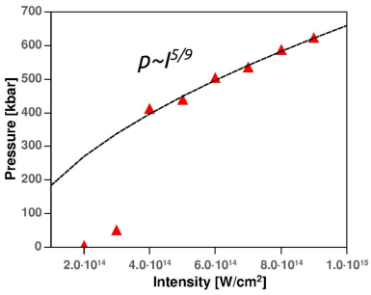

Fig. 10. Laser intensity dependence of the photo-induced pressure (in kbar) The laser is linearly polarized along the [001] direction.

4. Conclusions

In conclusion, our real-time simulations provide a unified physical framework describing the non-equilibrium response of diamond subjected to high-intensity femtosecond laser pulses. The optical breakdown threshold of crystalline diamond is obtained as a function of the laser energy fluence and polarization direction. The occurrence of breakdown is associated with high electronic excitation, plasma formation and highly efficient free-carrier absorption. We demonstrated that optical breakdown converts diamond into a transient metallic state, where high-density conduction state occupation induces strong Pauli blocking that saturates photo-ionization. The resulting metallic plasma drives the real part of the dielectric function strongly negative, enabling surface plasmon polariton modes that lead to the formation of low-spatial-frequency LIPSS with sub-wavelength spatial periods. The electron density difference distribution shows the effect of softening of C-C bonds: the charge density in the binding region is not sufficient to balance the nuclear repulsion forces, resulting in instability of the diamond lattice.

In this regime of high electronic excitation, an unbalanced photo-induced degeneracy pressure results in mechanical instability of the lattice, which may be considered as a precursor to ultrafast melting and ablation of diamond.

We have demonstrated that a single physical driver photo-induced electronic bond charge depletion naturally accounts for both solid-to-solid non-thermal phase transitions and macroscopic SPP-driven surface nanostructuring.

Acknowledgements: Support from KP-06-COST/26 (BNSF) and CA21128 are acknowledged.

References

[1] J. Bonse, S. Höhm, S. V. Kirner, A. Rosenfeld, and J. Krüger, "Laser-induced periodic surface structures—a concise review," IEEE Journal of Selected Topics in Quantum Electronics, 23, pp. 1–12, 2017.

[2] A. M. Zaitsev, Optical Properties of Diamond: A Data Handbook, Springer Science & Business Media, 2001.

[3] T. V. Kononenko, V. V. Kononenko, and V. I. Konov, "Femtosecond laser structuring of diamond surface," Physics of Wave Phenomena, vol. 26, no. 3, pp. 195–203, 2018.

[4] S. K. Sundaram and E. Mazur, "Inducing and probing non-thermal transitions in semiconductors using femtosecond laser pulses," Nature Materials, vol. 1, no. 4, pp. 217–224, 2002.

[5] L. V. Keldysh, "Ionization in the field of a strong electromagnetic wave," Soviet Physics JETP, vol. 20, no. 5, pp. 1307–1314, 1965.

[6] N. Medvedev and B. Rethfeld, "Transients in the dielectric function of semiconductor irradiated by an ultrashort laser pulse," Journal of Applied Physics, vol. 108, no. 10, p. 103112, 2010.

[7] S. M. Pimenov, V. V. Kononenko, and V. I. Konov, "Modification of Diamond Surface by Femtosecond Laser Pulses," Photonics, vol. 10, no. 10, p. 1077, 2023.

[8] J. Reif, F. Costache, M. Henyk, and S. P. Banerjee, "Ripples revisited: non-linear multiple-pulse dielectric ablation," Applied Surface Science, vol. 197, pp. 891–895, 2002.

[9] P. Stampfli and K. H. Bennemann, "Theory for the instability of the diamond structure of Si, Ge, and C induced by a dense electron-hole plasma," Physical Review B, vol. 42, no. 11, p. 7163, 1990.

[10] R. M. Martin, "Relation between elastic moduli of I-VII, II-VI, and III-V compounds," Physical Review B, vol. 1, no. 10, p. 4005, 1970.

[11] V. Heine and J. A. Van Vechten, "Alternative theory of pressure-induced phase transitions in III-V and II-VI compounds," Physical Review B, vol. 11, no. 10, p. 3779, 1975.

[12] R. Biswas and V. Ambegaokar, "Phonon frequencies and lattice stability of a plasma-created semiconductor phase," Physical Review B, vol. 26, no. 4, p. 1980, 1982.

[13] T. Apostolova, B. Obreshkov, and I. Gnilitskyi, "Ultrafast energy absorption and photoexcitation of bulk plasmon in crystalline silicon subjected to intense near-infrared ultrashort las

Influence of microstructural modification of cement-based composites on transport processes and long-term reliability

Veis Šerifi[1,*], Nazim Manić[1], Emir Maslak[1] and Vesnera Šerifi[2]
[1]State University of Novi Pazar, Department of Technical and Technological Sciences, Faculty of Civil Engineering, Novi Pazar, Serbia
[2]University of Pristina, Faculty of Technical Sciences, Architecture, Kosovska Mitrovica
email: serifiveis@np.ac.rs

Abstract. *The long-term durability of cement-based composites is strongly influenced by their microstructural characteristics and resistance to the transport of water and aggressive ionic species. This study presents a parametric numerical investigation of the influence of binder modification on transport-related properties and predicted chloride penetration in cement-based composites. Four representative compositions were analysed: a reference Portland cement composite (REF), a mixture containing 10% silica fume (SF10), a mixture containing 15% metakaolin (MK15), and a hybrid mixture incorporating 5% silica fume and 10% metakaolin (HYB). The comparative assessment included accessible porosity, initial sorptivity, chloride migration coefficient and a proposed dimensionless Transport Resistance Index (TRI). Long-term chloride penetration was additionally evaluated using a simplified one-dimensional Fickian transport model for exposure periods of up to 50 years. Within the adopted parametric scenario, the HYB composition exhibited the most favourable overall performance, with reductions of approximately 28.3% in accessible porosity, 51.0% in initial sorptivity and 69.0% in chloride migration coefficient compared with the reference composite. The predicted comparative chloride penetration depth after 50 years decreased from approximately 134.5 mm for REF to 74.8 mm for HYB. The time required to reach a comparative penetration depth of 50 mm increased from approximately 6.9 years for REF to 22.3 years for HYB. Strong descriptive correlations were observed between accessible porosity, sorptivity and chloride transport. The results indicate that optimised binder modification may significantly improve resistance to transport processes and delay chloride penetration. However, the presented results should be interpreted as a comparative parametric analysis requiring subsequent experimental validation before application to quantitative structural service-life prediction.*

KEYWORDS: *CEMENT-BASED COMPOSITES; MICROSTRUCTURE; SILICA FUME; METAKAOLIN; POROSITY; SORPTIVITY; CHLORIDE TRANSPORT; DURABILITY.*

1 Introduction

Cement-based composites are among the most widely used construction materials because of their mechanical performance, technological adaptability and comparatively high durability. Their long-term behaviour, however, is strongly controlled by the ability of the cementitious matrix to resist the penetration of water, gases and aggressive ions through its pore system. Chloride ingress is particularly important for reinforced concrete structures exposed to marine environments, de-icing salts and other chloride-containing media, because accumulation of chlorides near reinforcement may initiate corrosion and progressively reduce structural reliability and service life [1,6].

Transport processes in cementitious materials are closely related to microstructural characteristics such as total and accessible porosity, pore-size distribution, connectivity, tortuosity and the properties of the interfacial transition zone. Total porosity alone does not fully determine permeability or ionic transport. Experimental studies have shown that larger interconnected capillary pores and the topology of the transport-active pore network may be more relevant to chloride migration than total porosity considered independently [5,13].

Partial replacement of Portland cement with supplementary cementitious materials is a widely investigated approach for modifying the microstructure of cement-based composites. Silica fume and metakaolin can alter hydration processes, refine the pore network and modify both transport resistance and chloride-binding behaviour. Their influence is not governed exclusively by a physical reduction in porosity; chemical composition and the resulting hydration products may also affect chloride interactions within the hardened binder [2,11].

Moisture condition further complicates ionic transport. Unsaturated ion diffusion depends on degree of saturation, pore solution characteristics and binder composition. Consequently, durability assessment based on a single material parameter is generally insufficient for reliable interpretation of long-term performance [3]. Diffusion-based approaches derived from Fick's laws are frequently used for simplified chloride penetration modelling, but the effective transport coefficient is not a universal constant and may vary with hydration, ageing, temperature, moisture and exposure conditions [4,6,12].

The objective of this study is to examine, within a clearly defined parametric numerical framework, how microstructural modification may influence accessible porosity, capillary water absorption, chloride transport and predicted long-term chloride penetration. The study compares a reference Portland cement composite with silica-fume, metakaolin and hybrid modifications, introduces a dimensionless Transport Resistance Index (TRI), and evaluates descriptive correlations among the principal transport-related parameters. The intention is not to present fabricated experimental measurements, but to establish a transparent, reproducible modelling framework that can subsequently be validated using laboratory data.

2 Materials and Research Methodology

2.1 Research design and composition of cement-based composites

Four representative mixtures were considered: a reference Portland cement mixture (REF), a mixture containing 10% silica fume (SF10), a mixture containing 15% metakaolin (MK15), and a hybrid mixture containing 5% silica fume and 10% metakaolin (HYB). The replacement percentages were defined by mass of total binder. The water-to-binder ratio was maintained at 0.40 and the total binder content at 450 kg/m³ in all mixtures. Fine and coarse aggregate contents were kept constant in order to isolate the influence of binder modification as far as possible. The proposed mixture proportions are presented in Table 1.

Table 1. Proposed composition of cement-based composites

Mixture	Portland cement (kg/m³)	Silica fume (kg/m³)	Metakaolin (kg/m³)	Water (kg/m³)	Fine aggregate (kg/m³)	Coarse aggregate (kg/m³)	w/b
REF	450.0	0	0	180	720	1020	0.40
SF10	405.0	45.0	0	180	720	1020	0.40
MK15	382.5	0	67.5	180	720	1020	0.40
HYB	382.5	22.5	45.0	180	720	1020	0.40

The selected mixtures represent different approaches to microstructural modification while maintaining an identical total binder content and water-to-binder ratio. This experimental configuration enables a direct comparison of transport-related properties and provides a basis for identifying possible synergistic effects associated with hybrid binder modification.

2.2 Specimen preparation and curing framework

For future experimental validation, all constituents should be mixed under identical laboratory conditions, cast using the same compaction procedure and cured under controlled conditions. A principal test age of 28 days is proposed, together with additional testing at 90 days to capture continued hydration and microstructural development. For each mixture and investigated property, at least three replicate specimens should be used, with results expressed as arithmetic mean, standard deviation and coefficient of variation.

2.3 Accessible porosity

Accessible pore volume is represented using the density, absorption and permeable-void concept of ASTM C642-21 [7]. The volume of permeable voids can be expressed as:

$$P = [(B - A)/(B - C)] \times 100 \quad (1)$$

where P is the volume of permeable voids (%), A is the oven-dry mass, B is the saturated mass in air, and C is the apparent mass of the immersed saturated specimen. Relative change in accessible porosity is evaluated as:

$$\Delta P_i = [(P_i - P_{REF})/P_{REF}] \times 100 \quad (2)$$

where P_i represents the porosity of the modified mixture and P_{REF} represents the corresponding value of the reference composite. A negative value of ΔPi indicates a reduction in accessible porosity relative to the reference mixture.

2.4 Capillary water absorption

Capillary water absorption is represented through initial sorptivity, consistent with the conceptual framework of ASTM C1585-20 [8]. Cumulative water absorption per unit exposed area is expressed as:

$$I(t) = m/(A\rho_w) \quad (3)$$

and initial sorptivity is obtained from the slope of the approximately linear relationship:

$$I = S_i\sqrt{t} + b \quad (4)$$

Lower values of initial sorptivity indicate reduced capillary intake and, generally, a more discontinuous or tortuous transport pathway for liquid water.

2.5 Chloride migration resistance

Chloride transport resistance is represented by a non-steady-state migration coefficient consistent with the comparative role of NT BUILD 492 [9]. Because migration-derived coefficients are not automatically identical to natural diffusion coefficients, they are used here as comparative transport indicators rather than intrinsic material constants [10]. The relative reduction is calculated as:

$$R_D = [1 - (D_i/D_{REF})] \times 100 \quad (5)$$

2.6 Long-term chloride transport model

Long-term chloride penetration is modelled using the simplified one-dimensional form of Fick's second law. For the parametric analysis, the adopted transport coefficient is denoted D* to emphasise its comparative, apparent character:

$$\partial C/\partial t = D^* \cdot \partial^2 C/\partial x^2 \quad (6)$$

Under the assumptions of a semi-infinite medium, constant surface chloride concentration and constant apparent transport coefficient, the normalised concentration profile is:

$$C(x,t)/C_s = 1 - erf[x/(2\sqrt{(D^*t)})] \quad (7)$$

A comparative penetration depth $x_{0.5}$ is defined as the depth at which $C(x,t)/C_s = 0.50$. This gives:

$$x_{0.5} = 0.9539\sqrt{(D^*t)} \quad (8)$$

The criterion is used only for relative comparison among mixtures. It does not represent a corrosion-initiation threshold or a complete service-life prediction.

2.7 Integrated Transport Resistance Index

A dimensionless Transport Resistance Index (TRI) is proposed to integrate the three principal comparative indicators: accessible porosity, initial sorptivity and chloride transport coefficient:

$$TRI_i = (1/3)[P_i/P_{REF} + S_i/S_{REF} + D_i/D_{REF}] \quad (9)$$

For the reference mixture TRI_REF = 1.00. Values below 1.00 indicate improved combined transport resistance relative to REF. TRI is introduced as a study-specific comparative index and is not intended to replace standard durability parameters or direct service-life calculations.

2.8 Statistical analysis

The relationships between accessible porosity, sorptivity and chloride transport are evaluated using Pearson's correlation coefficient and simple linear regression. Because the dataset contains only four parametrically defined compositions, the coefficients are interpreted descriptively and are not used as evidence of general statistical significance.

3 Results and Discussion

3.1 Comparative transport-related properties

The adopted parametric dataset is presented in Table 2. These values are model inputs selected to enable a systematic comparison of plausible transport-response trends; they are not reported as laboratory measurements.

Table 2. Parametric values of transport-related properties

Mixture	Accessible porosity P (%)	Initial sorptivity S (mm/min$^{0.5}$)	Chloride migration coefficient D ($\times 10^{-12}$ m²/s)	TRI
REF	13.8	0.145	12.6	1.000
SF10	10.7	0.082	4.8	0.574
MK15	11.2	0.091	5.6	0.628
HYB	9.9	0.071	3.9	0.506

Relative to REF, SF10 showed reductions of approximately 22.5% in accessible porosity, 43.4% in initial sorptivity and 61.9% in chloride transport coefficient. MK15 showed corresponding reductions of 18.8%, 37.2% and 55.6%. The most pronounced

combined improvement was obtained for HYB, with reductions of 28.3%, 51.0% and 69.0%, respectively (figure 1). The direction of these changes is consistent with experimental literature reporting improved pore characteristics and chloride resistance in concretes containing metakaolin and silica fume [11].

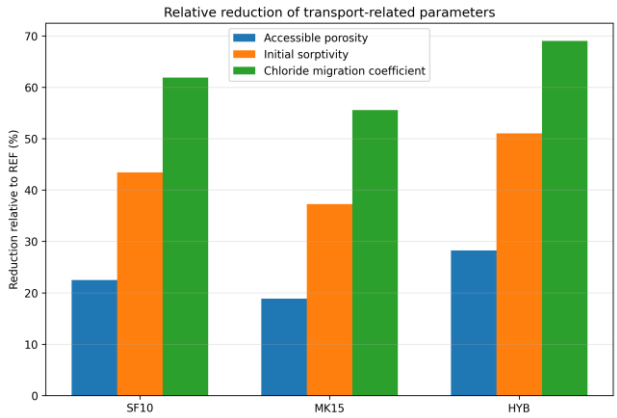

Figure 1. *Relative reduction of transport-related parameters compared with the reference mixture.*

3.2 Long-term prediction of chloride penetration

Using the simplified Fickian model and the adopted apparent transport coefficients, comparative chloride penetration was calculated for exposure periods of 1, 5, 10, 25 and 50 years. The results are presented in Table 3. The ranking HYB < SF10 < MK15 < REF remained unchanged throughout the analysed period.

Table 3. *Predicted comparative chloride penetration depth $x_{0.5}$*

Exposure period	REF (mm)	SF10 (mm)	MK15 (mm)	HYB (mm)
1 year	19.0	11.7	12.7	10.6
5 years	42.5	26.3	28.4	23.7
10 years	60.1	37.1	40.1	33.5
25 years	95.1	58.7	63.4	52.9
50 years	134.5	83.0	89.7	74.8

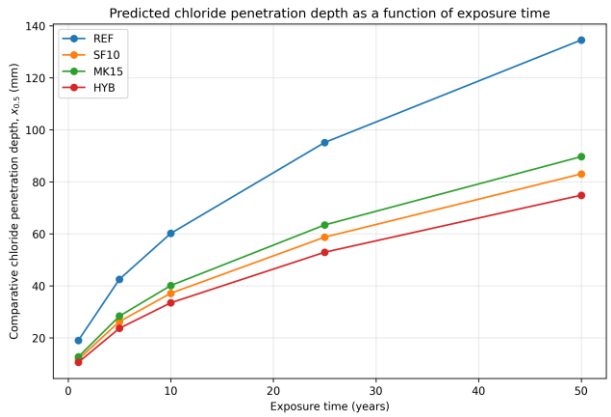

Figure 2. *Predicted comparative chloride penetration depth as a function of exposure time.*

After 10 years, the predicted comparative penetration depth was approximately 60.1 mm for REF and 33.5 mm for HYB. After 50 years, the corresponding values were 134.5 mm and 74.8 mm (figure 2). These differences demonstrate the sensitivity of long-term penetration depth to the assumed apparent transport coefficient. Because migration coefficients evolve with concrete age and exposure, absolute service-life prediction requires time-dependent experimentally calibrated parameters [12].

3.3 Normalised chloride concentration at a depth of 50 mm

A second comparison was made at a fixed depth of 50 mm. The calculated values are expressed as the normalised concentration $C_r = C(50\ mm,t)/C_s$.

Table 4. *Predicted normalised chloride concentration at 50 mm depth*

Exposure period	REF	SF10	MK15	HYB
1 year	0.076	0.004	0.008	0.001
5 years	0.428	0.199	0.234	0.154
10 years	0.575	0.364	0.400	0.314
25 years	0.723	0.566	0.595	0.524
50 years	0.802	0.685	0.707	0.652

At five years, the normalised chloride concentration at 50 mm was 0.428 for REF and 0.154 for HYB. At ten years, the corresponding values were 0.575 and 0.314 (table 4). Although continued exposure progressively increases chloride penetration in all mixtures, the modified binders delay the development of concentration at a given depth within the adopted modelling assumptions.

3.4 Time required to reach a comparative penetration depth of 50 mm

Table 5. *Predicted time to reach $x_{0.5}$ = 50 mm*

Mixture	Time (years)	Relative increase compared with REF
REF	6.9	–
MK15	15.5	+125%
SF10	18.1	+163%
HYB	22.3	+223%

The simplified model indicates that HYB requires approximately 22.3 years to reach the comparative depth criterion, compared with 6.9 years for REF. The ratio t_HYB/t_REF is approximately 3.23 (table 5). This is a comparative modelling result and must not be interpreted directly as reinforcement corrosion-initiation time, which additionally depends on surface chloride concentration, critical chloride threshold, cover depth, moisture, temperature, ageing and chloride binding.

3.5 Integrated transport resistance

The proposed TRI provides a compact ranking of combined transport resistance. The values were 1.000 for REF, 0.628 for MK15, 0.574 for SF10 and 0.506 for HYB. Lower values indicate improved performance relative to the reference mixture.

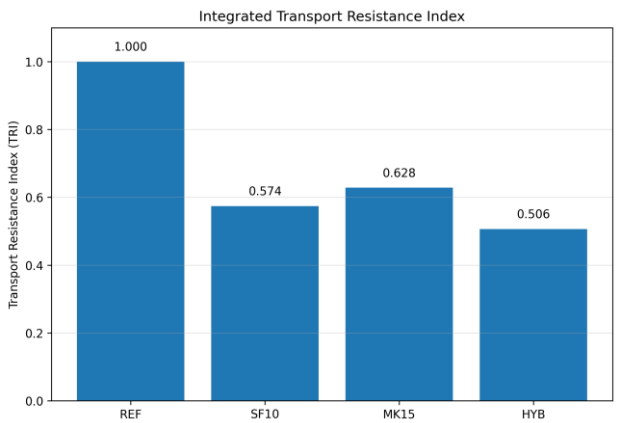

Figure 3. *Integrated Transport Resistance Index for the investigated mixtures.*

The combined ranking was therefore REF < MK15 < SF10 < HYB in terms of increasing transport resistance (figure 3). The result suggests a potentially beneficial hybrid effect, but because the underlying values are parametric, the ranking should be treated as a model-based hypothesis requiring experimental verification.

3.6 Correlation analysis

Descriptive Pearson correlation coefficients were calculated for the four-point dataset (table 6). Strong positive associations were obtained among all three transport-related parameters.

Table 6. *Descriptive correlations between transport-related parameters*

Parameters	Pearson r	R^2
Accessible porosity – Sorptivity	0.997	0.994
Accessible porosity – Chloride migration coefficient	0.989	0.978
Sorptivity – Chloride migration coefficient	0.997	0.994

The corresponding regression relationships were $S = 0.01943P - 0.12421$, $D = 2.331P - 19.853$, and $D = 120.674S - 5.011$. These very high coefficients reflect the internally consistent construction of the parametric dataset and must not be interpreted as universal empirical laws. Experimental research indicates that chloride transport is controlled by a combination of porosity, pore connectivity, pore-size distribution, pore-solution conductivity and physicochemical interactions [5,13].

3.7 Limitations and implications

The principal limitation of the present study is that the numerical values were defined parametrically rather than measured experimentally. Accordingly, the analysis should be regarded as a transparent hypothesis-generating framework. The simplified Fickian model further assumes constant boundary conditions and a time-independent apparent transport coefficient, whereas real chloride ingress is influenced by ageing, moisture, temperature, binding and exposure history. Nevertheless, the framework is useful for demonstrating how alternative binder modifications can be compared consistently and for defining the experimental programme required for future validation.

4 Conclusions

1. Within the adopted parametric scenario, all modified mixtures exhibited lower accessible porosity, lower initial sorptivity and lower chloride transport coefficients than the reference mixture.
2. The HYB mixture showed the most favourable combined performance, with reductions of approximately 28.3% in accessible porosity, 51.0% in initial sorptivity and 69.0% in the chloride transport coefficient relative to REF.
3. The reduction in predicted chloride transport was substantially greater than the reduction in accessible porosity, supporting the interpretation that pore connectivity, tortuosity and microstructural refinement are critical in addition to total accessible pore volume.
4. The proposed TRI ranked the mixtures consistently as REF < MK15 < SF10 < HYB in terms of increasing transport resistance.
5. Using the simplified long-term model, the predicted comparative penetration depth after 50 years decreased from approximately 134.5 mm for REF to 74.8 mm for HYB.
6. The time required to reach $x_{0.5}$ = 50 mm increased from approximately 6.9 years for REF to 22.3 years for HYB under identical simplified boundary conditions.
7. Strong descriptive correlations were obtained among accessible porosity, sorptivity and chloride transport, but the four-point parametric dataset is too limited for statistically generalisable conclusions.
8. The proposed approach provides a coherent framework linking binder composition, transport indicators and long-term chloride penetration, but experimental validation is essential before quantitative structural service-life predictions are made.

Future research should experimentally determine porosity, sorptivity and chloride migration for the proposed mixture series, extend testing to multiple curing ages, characterise pore-size distribution and chloride binding, and calibrate a time-dependent transport model. Such validation would enable the parametric framework to evolve into a quantitative durability and service-life assessment tool.

References

1. Jensen, O. M., Hansen, P. F., Coats, A. M., & Glasser, F. P. (1999). Chloride ingress in cement paste and mortar. Cement and Concrete Research, 29(9), 1497–1504. https://doi.org/10.1016/S0008-8846(99)00131-3.
2. Thomas, M. D. A., Hooton, R. D., Scott, A., & Zibara, H. (2012). The effect of supplementary cementitious materials on chloride binding in hardened cement paste. Cement and Concrete Research, 42(1), 1–7. https://doi.org/10.1016/j.cemconres.2011.01.001.
3. Olsson, N., Lothenbach, B., Baroghel-Bouny, V., & Nilsson, L.-O. (2018). Unsaturated ion diffusion in cementitious materials – The effect of slag and silica fume. Cement and Concrete Research, 108, 31–37. https://doi.org/10.1016/j.cemconres.2018.03.007.
4. Shafikhani, M., & Chidiac, S. E. (2020). A holistic model for cement paste and concrete chloride diffusion coefficient. Cement and Concrete Research, 133, 106049. https://doi.org/10.1016/j.cemconres.2020.106049.
5. Chen, R., Mu, S., & Liu, J. (2022). Relationship between chloride migration coefficient and pore structures of long-term water curing concrete. Construction and Building Materials, 341, 127741. https://doi.org/10.1016/j.conbuildmat.2022.127741.
6. Oh, B. H., & Jang, S. Y. (2007). Effects of material and environmental parameters on chloride penetration profiles in concrete structures. Cement and Concrete Research, 37(1), 47–53. https://doi.org/10.1016/j.cemconres.2006.09.005.
7. ASTM International. (2021). ASTM C642-21: Standard Test Method for Density, Absorption, and Voids in Hardened Concrete. ASTM International, West Conshohocken, PA.
8. ASTM International. (2020). ASTM C1585-20: Standard Test Method for Measurement of Rate of

Absorption of Water by Hydraulic-Cement Concretes. ASTM International, West Conshohocken, PA.
9. NORDTEST. (1999). NT BUILD 492: Concrete, Mortar and Cement-Based Repair Materials: Chloride Migration Coefficient from Non-Steady-State Migration Experiments. NORDTEST.
10. Andrade, C. (2005). Concepts on the chloride diffusion coefficient. In: Third RILEM Workshop on Testing and Modelling the Chloride Ingress into Concrete. RILEM Publications.
11. Poon, C. S., Kou, S. C., & Lam, L. (2006). Compressive strength, chloride diffusivity and pore structure of high performance metakaolin and silica fume concrete. Construction and Building Materials, 20(10), 858–865. https://doi.org/10.1016/j.conbuildmat.2005.07.001.
12. Audenaert, K., Yuan, Q., & De Schutter, G. (2010). On the time dependency of the chloride migration coefficient in concrete. Construction and Building Materials, 24(3), 396–402. https://doi.org/10.1016/j.conbuildmat.2009.07.003.
13. Wilson, W., Georget, F., & Scrivener, K. (2021). Unravelling chloride transport/microstructure relationships for blended-cement pastes with the mini-migration method. Cement and Concrete Research, 140, 106264. https://doi.org/10.1016/j.cemconres.2020.106264.
14.

Hot deformation processing of Ti–Zr–Nb biomedical alloys

Denys Oryshych[1*], Oleksandr Stasiuk[1], Dmytro Savvakin[1]
G. V. Kurdyumov Institute for Metal Physics of the N.A.S. of Ukraine[1]
den.oryshych@gmail.com

Abstract: *Hot deformation is a promising approach for modification the microstructure of metallic materials, as it combines the simultaneous action of elevated temperature and mechanical loading. Under these conditions, intense plastic flow increases the density of crystal lattice defects and promotes dynamic recrystallization, resulting in grain refinement and a corresponding increase in the grain boundary density. Since grain boundaries serve as effective vacancy sinks, the formation of such deformed and recrystallized microstructures enhances vacancy diffusion and activates pore elimination, thereby promoting densification and the formation of low-porosity or nearly fully dense materials.*
Keywords*: TITANIUM ALLOY, POWDER METALURGY, HOT DEFORMATION*

1. Introduction

Ti-Nb-Zr alloys have attracted considerable attention for biomedical applications, including orthodontic archwires, bone fixation plates, and vascular stents, owing to their excellent corrosion resistance, high strength, and favorable elastic properties [1-3]. The addition of zirconium to titanium enhances the mechanical performance of these alloys while maintaining excellent corrosion resistance and biocompatibility [4, 5]. A key requirement for metallic implant materials is a low Young's modulus, ideally approaching that of human cortical bone (approximately 30 GPa), in order to minimize the stress shielding effect and promote long-term implant performance [6-7]. Previous studies have demonstrated that alloying Ti-Zr alloys with a sufficient amount of the β-stabilizing element niobium significantly reduces the Young's modulus to approximately 50-60 GPa. This reduction is primarily attributed to the formation and stabilization of the β body-centered cubic (BCC) Ti-Zr-Nb phase [8-10].

It is well known that in powder metallurgy production pore elimination gradually slows during the final stage of sintering and eventually ceases because pore coalescence becomes the prevailing process without reducing the total pore volume. This behavior is explained by the Slyozov mechanism [20]. According to this mechanism, the vacancy flux from the pore system to vacancy sinks is redirected from smaller to larger pores within the same grain. As a result, larger pores grow at the expense of smaller ones, leading to pore coarsening rather than further densification. Therefore, enhancing pore elimination requires increasing the density of effective vacancy sinks, such as grain boundaries and dislocations, which promote vacancy migration and facilitate continued densification.

Thermomechanical processing is one of the most effective approaches for tailoring the microstructure of metallic materials and enhancing their mechanical and physical properties. This approach is also applicable to alloys produced by the powder metallurgy route employed in the present study. Accordingly, additional deformation processing at room and elevated temperatures offers a promising strategy for reducing the residual porosity of the synthesized Ti-Zr-Nb alloys while improving their mechanical performance. Therefore, this section examines the effect of cold and hot deformation on the microstructural evolution, densification, and resulting mechanical properties of the synthesized alloys.

2. Materials and methods

Due to promising mechanical properties there were investigated two biomedical materials: 59Zr-19Ti-22Nb and 35Zr-39,5Ti-25,5Nb. They were manufactured using powder metallurgy methods. The starting materials were zirconium hydride powders ZrH_2 and titanium TiH_2 with a size of less than 100 microns and niobium metal powder with a size of less than 63 microns. The mixing process of the corresponding elements took place for six hours. The compaction of the mixtures was carried out by cold pressing in steel molds. The pressing pressure was 650 MPa. The resulting compacts were sintered at a temperature of 1250°C with a subsequent holding time of 4 hours, after which they were cooled together with the furnace.

There were used sintered samples of parallelepiped shape with a length of ~ 60 mm, a width of ~ 20 mm and a thickness of ~ 9 mm for hot pressing. Pressing was carried out at a temperature of 900°C and a pressure of 780 MPa.

3. Results

The microstructure shown in Fig. 1 indicates that the investigated materials are characterized by a significant level of porosity. Therefore, hot deformation was employed as an additional processing method to modify the microstructure and reduce the residual porosity of the materials. The material is simultaneously exposed to mechanical stresses and high temperature with intense metal flow and an increase in the defectivity of its crystal structure, which causes the development of recrystallization processes with a decrease in grain size and a corresponding increase in the density of grain boundaries. Since grain boundaries are sinks for vacancies, the creation of such deformed and recrystallized structural states activates the processes of pore healing, contributing to the achievement of low-porosity or practically non-porous structures.

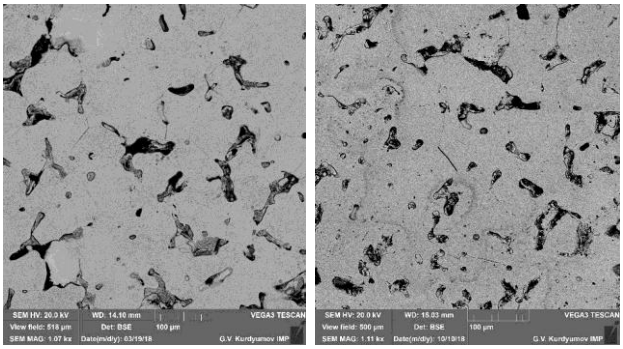

a *b*

Fig.1. *As-sintered microstructures of 59Zr-19Ti-22Nb (a) and 35Zr-39.5Ti-25.5Nb (b) alloys.*

For these alloys, deformation values of the order of 55-65% can be achieved in one cycle of heating to 900 °C with a load. Fig.2 shows that already at deformation levels of about 30%, porosity is significantly reduced, individual, significantly deformed grains are visible in the microstructure and signs of recrystallization processes appear. Thus, along with relatively large grains (of the order of 100-140 μm), which were formed during the synthesis of alloys, there are smaller grains (40-50 μm), formed as a result of recrystallization. In addition, it was recorded that, in addition to a decrease in the volume fraction of pores (up to 2%), their size also decreases (up to 10-20 μm).

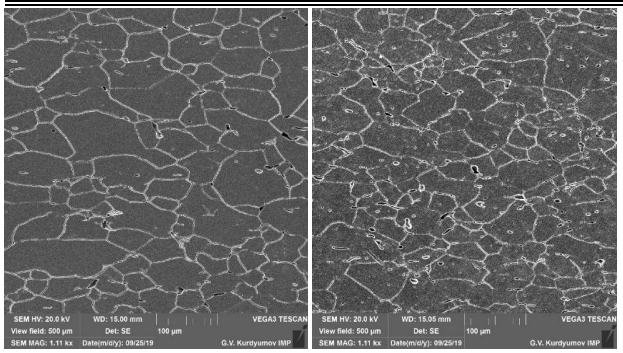

a *b*

Fig.2 *Microstructures of the 59Zr–19Ti–22Nb (a) and 35Zr–39.5Ti–25.5Nb (b) alloys after hot pressing at 900 °C with a deformation degree of 30%.*

At deformation levels of 40–55% (fig.3), the volume fraction of pores decreases to approximately 1–1.5%. At the same time, a substantial increase in the fraction of recrystallized grains is observed compared with deformation levels of up to 30% (fig.2). It should be noted that the evolution of deformation and recrystallization processes is strongly dependent on the chemical composition of the alloys. Consequently, the investigated alloys exhibit some differences in both the residual pore fraction and the proportion of recrystallized grains.

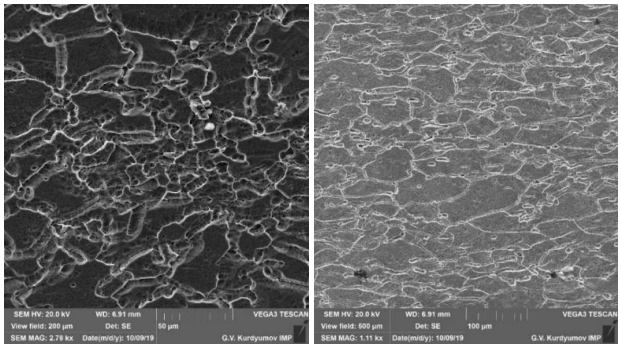

a *b*

Fig.3 *Microstructures of the 59Zr–19Ti–22Nb (a) and 35Zr–39.5Ti–25.5Nb (b) alloys after hot pressing at 900 °C with a deformation degree of 40-45%.*

When alloy deformation degrees of about 60% are reached (fig.4), a practically non-porous recrystallized structure is observed, which is anisotropic due to the elongated shape of the grains.

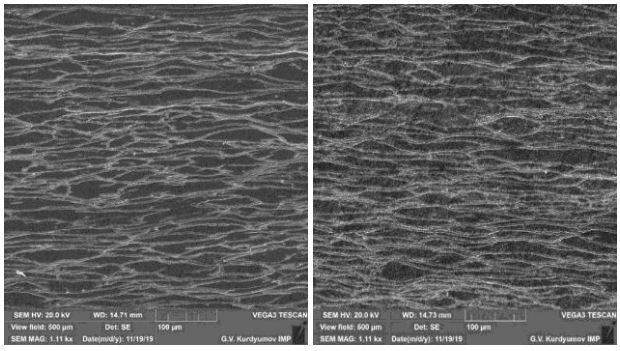

a *b*

Fig.4 *Microstructures of the 59Zr–19Ti–22Nb (a) and 35Zr–39.5Ti–25.5Nb (b) alloys after hot pressing at 900 °C with a deformation degree of 60%.*

To evaluate the influence of microstructural changes obtained under the action of hot pressing on the mechanical characteristics of alloys of the Zr-Ti-Nb system, their hardness and Young's modulus were measured. Given the difference in the shape and size of the samples required for conducting different types of mechanical tests, materials hot pressed with a deformation value of up to 60% were investigated to measure hardness, and 40-45% to measure Young's modulus. The results are given in Table 1.

Table 1: *The effect of hot deformation on changes in hardness and Young's modulus.*

Alloy composition	Hot-deformed state		Hot-deformed state	
	Young's modulus, GPa	Hardness HV	Модуль Юнга, ГПа (deform. 40-45%)	Hardness HV (deform. 60%)
59Zr-19Ti-22Nb	56.3	185	71.3	298
35Zr-39.5Ti-25.5Nb	55	159	62.6	291

X-ray diffraction analysis performed for the 39Zr–36.1Ti–24.9Nb alloy revealed no changes in the phase composition following deformation. The material retained its single-phase β-BCC structure (fig.5), indicating that the applied deformation treatment does not induce phase transformations. The preservation of the β phase is particularly beneficial for the intended biomedical application, as stabilization of the β-BCC structure is essential for achieving a reduced Young's modulus and, consequently, improving the mechanical compatibility of the alloy with bone tissue.

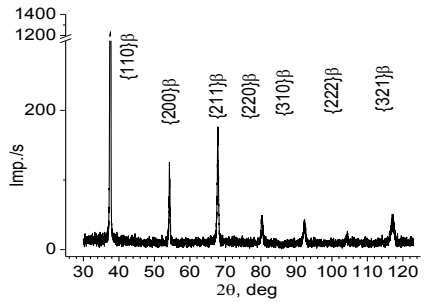

Fig.5 *X-ray diffraction analysis of39Zr–36.1Ti–24.9Nb alloy*

As shown in Table 1, hot pressing with deformation levels of up to 60%, resulting in a practically pore-free microstructure, leads to an increase in the hardness of all investigated Zr–Ti–Nb alloys. It is also noteworthy that deformation substantially reduces the differences in hardness among the studied compositions. This behavior can be attributed to the initially different porosity levels of the synthesized alloys, which means that their hardness is governed by two main factors: the pore volume fraction and the chemical composition of the β-BCC phase. Following deformation, the formation of a nearly pore-free structure eliminates the contribution of porosity to the measured hardness, making the effect of the β-phase composition the dominant factor determining the hardness of the alloys.

Considering the critical importance of Young's modulus for biomedical alloys, its value was measured for the 59Zr–19Ti–22Nb and 35Zr–39.5Ti–25.5Nb alloys in both the as-synthesized and deformed states to evaluate the effect of hot pressing. In the as-synthesized state, both compositions exhibited relatively low Young's modulus values of 55–56 GPa (Table 1). As expected, deformation treatment resulted in an increase in Young's modulus, which reached 63–71 GPa in the nearly pore-free states (Table 1). According to [21], this increase can be attributed to the approximately linear dependence of Young's modulus on the porosity of the material. Thus, the substantial reduction in the pore

volume fraction during hot pressing leads to a corresponding increase in the effective elastic modulus (Fig. 6).

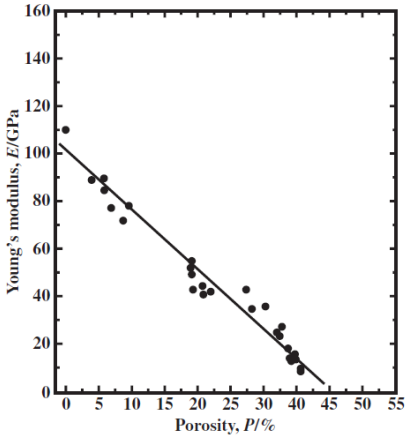

Fig.6. *Young's modulus dependence on the titanium alloys porosity [21].*

4. Conclusions

Hot pressing effectively reduced the residual porosity of the synthesized alloys. At deformation levels of 40–55%, the pore fraction decreased to 1–1.5%, while deformation up to 60% resulted in nearly pore-free structures. Increasing deformation also promoted recrystallization.

The Young's modulus of the investigated alloys increased from 55–56 GPa in the as-synthesized state to 63–71 GPa after hot deformation. This increase is mainly attributed to pore elimination, as the effective elastic modulus of porous materials strongly depends on their porosity.

Hot deformation is an effective way to influence the microstructure of synthesized Zr-Ti-Nb alloys. The hot-pressing method achieved practically pore-free states, which made it possible to significantly regulate the complex of physical and mechanical characteristics of the material, which was confirmed by an increase in the values of their hardness and Young's modulus.

References

1. Duerig TW, Albrecht J, Richter D, Fischer P. Acta Metall 1982;30:2161–72.
2. Grosdidier T, Philippe MJ. Mater Sci Eng A 2000;291:218–23.
3. Takahashi E, Sakurai T, Watanabe S, Masahashi N, Hanada S. Mater Trans 2002;43:2978–83.
4. Y. Zhentao, Z. Lian, Mater. Sci. Eng. A 438–440 (2006) 391–394.
5. A. Inoue, Acta Mater. 48 (2000) 279–306.
6. Song Y Theoretical study of the effects of alloying elements on the strength and modulus of β-type bio-titanium alloys / Song Y, Xu DS, Yang R // Materials Science and Engineering: A. — 1999. — pp 269–274.
7. Yu Xiang Ni Decyl bis phosphonate–protein surface modification of Ti–6Al–4V via a layer-by-layer technique / Yu Xiang Ni, Bo Feng, Jianxin Wang, Xiong Lu, Shuxin Qu, Jie Weng // Journal of Materials Science. — 2009. — pp 4031-4039.
8. M. Long, H.J. Rack, Biomaterials 19 (1998) 1621–1639
9. Takahashi M, Kobayashi E, Doi H, Yoneyama T, Hamanaka H. Phase stability and mechanical properties of biomedical B type titanium–zirconium based alloys containing niobium. J. Jpn Inst Met, 2000;64:1120–6.
10. Yang GJ, Zhang T. Phase transformation and mechanical properties of the Ti50Zr30Nb10Ta10 alloy with low modulus and biocompatible. J. Alloy Compounds, 2005;392: 291–4.
11. Ivasishin O.M.. Markovskiy P.E.. Popov A.A.. Karasevskaya O.P.. Mordyuk B.N.. Skiba I.A.. Illarionov A. G. Obrazovaniye nanostrukturnoy □-fazy v deformirovannykh metastabilnykh β-splavakh na osnove Ti i Zr. Metallofizika I noveyshiye tekhnologii2011, t.33, №5, p. 673-685. (in Russian)
12. S. V. Grib. A. G. Illarionov. A. A. Popov. O.M.Ivasishin. Razrabotka i issledovaniye struktury. fiziko-mekhanicheskikh svoystv nizkomodulnykh splavov sistemy Ti–Zr–Nb. Fizika metallov i metallovedeniye. 2014. t 115. No 6. p. 638–647 (in Russian)
13. A.N.Timoshevskii, S.Yablonovskyy, O.M.Ivasishin. First- principles calculations atomic structure and elastic properties of Ti- Nb alloys. // Functional Materials. - 2012. - 19, № 2. - p. 266-271.
14. D.G.Savvakin. N.M.Gumenyak. Sintez splavov na osnove binarnoy sistemy tsirkoniy-titan s ispolzovaniyem dispergirovannogo gidrida tsirkoniya // Metallofizika i noveyshiye tekhnologii. 2013. t.35. №3. p.349-358. (in Russian)
15. O.M. Ivasishin, D.H.Savvakin. Syntez splaviv na osnovi tsyrkoniiu i tytanu z vykorystanniam yikh hidrydiv. FKhMM, 2015, t.51, №4, p.27-35. (in Ukrainian) F.H.Froes, D.Eylon. Powder metallurgy of titanium alloys, Inter. Mater. Rev.-1990. -v.35, No. 3. - p.162-182.
16. Ivasishin O.M., Savvakin D.G. The Impact of Diffusion on Synthesis of High-Strength Titanium Alloys from Elemental Powder Blends. Key Engineering Materials. – 2010. -vol. 436. - p. 113-121.
17. D.V.Oryshych, D.G.Savvakin, O.O.Stasiuk, B.Ya.Melamed Solid state synthesis of Zr-Ti-Nb alloys using multicomponent powder blends. Metallophysics and Advanced Technologies.2019, vol. 41, No. 2, pp. 213–226.
18. O.M.Ivasishin, D.G.Savvakin, D.V.Oryshych, O.O.Stasiuk, Li Yuanyuan, Hydride Approach in Blended Elemental Powder Metallurgy of Beta Titanium Alloys, Presented at 14th World Conference on Titanium Ti-2019 (10-14 June 2019), Nantes, France; will be published in the proceedings
19. O. M. Ivasishin, O. P. Karasevska, D. G. Savvakin, M. M. Humenyak, Ya. I. Melnyk, and O. O. Stasiuk. Metallophysics and Advanced Technologies. 2016, vol. 38, pp. 1527-1540 (in Ukrainian)
20. Slezov, V. and Sagalovich, V., 1987. Diffusive decomposition of solid solutions. Uspekhi Fizicheskih Nauk, 151(1), p.67
21. M.Niinomi. Biologically and mechanically compatible titanium alloys. Material Transactions, vol.49, No 10, 2008, p 2170-2178.

Effect of refining time on porosity and mechanical preperties of low-ressure casting made of $ALSI_7MG$ alloy

Jaroslaw Piatkowski[1], Tomasz Matula[1], Marco A. Reyna[2]

[1] Silesian University of Technology, Katowice, Poland

[2] Superior Industries Parque Industrial Chihuahua Sur, 31090 Chihuahua, Mexico

E-mail: jaroslaw.piatkowski@polsl.pl, tomasz.matula@polsl.pl, mreyna@supind.com

Abstract: *The study determines the effect of gas-bubbling refining time on porosity and mechanical properties of low-pressure AlSi7Mg alloy castings under industrial conditions. Refining was performed with an NH_2 mixture (90% N + 10% H_2) for 5.0–9.0 min. Porosity, density index, HB hardness, tensile strength R_m, 0.2% proof stress $R_{p0.2}$ and elongation A were evaluated. The optimum refining time was 7 min, giving minimum porosity and mechanical properties meeting customer requirements. Longer refining increased porosity and reduced selected mechanical properties.*

KEYWORDS: *ALUMINIUM ALLOYS, POROSITY, LOW-PRESSURE CASTING, MECHANICAL PROPERTIES.*

1. Introduction

The mechanical properties of aluminium alloys depend, among other factors, on structural heterogeneity resulting from the manufacturing process. The course of this process affects the morphology and size of constituents such as α(Al) solid-solution dendrites, silicon crystals in the α(Al)+β(Si) eutectic, and intermetallic phases such as Mg_2Si. Individual production stages also influence casting defects, including shrinkage and gas porosity [1–4]. This is particularly important because, in many foundries, porosity is a major product-quality criterion that must meet customer requirements. This is because porosity adversely affects many service properties, especially the strength and ductility of castings.

The porosity of aluminium-alloy castings is affected by numerous technological, material and process-related factors. The most important include [5–10]:

1. hydrogen content – an excessive amount of hydrogen dissolved in liquid aluminium leads to gas porosity. During solidification, hydrogen is released in the form of gas bubbles,
2. hydrogen sources – e.g. moisture in the furnace atmosphere, wet tools and alloy contamination,
3. presence of oxides and inclusions – Al_2O_3 particles and other contaminants may initiate pore formation. Inclusions disturb solidification and facilitate hydrogen entrapment,
4. refining process – improper refining fails to remove hydrogen and oxides. A process that is too short or too intensive may be ineffective or even detrimental,
5. chemical composition of the alloy – some alloying additions increase susceptibility to porosity; for example, a high magnesium content increases the tendency towards oxidation and hydrogen absorption.

It follows from the above that most factors affecting porosity are related to the refining process; therefore, investigations were undertaken in this area.

2. Prerequisites and means for solving the problem

As already mentioned, for manufacturers of many cast products, porosity is the most common criterion for compliance with customer specifications and therefore determines whether a product can be sold. On the one hand, foundries should reduce the defect rate; on the other hand, because of corporate constraints, they cannot directly modify the technology or the type of casting alloy. Such changes require customer approval each time and involve costly pre-production tests. Therefore, solutions that improve profitability, are inexpensive, easy to implement and do not require customer approval are preferred. One such measure is optimisation of the AlSi7Mg alloy refining parameters towards reducing the process duration, since the customer also specifies the type of refining.

3. Solution of the examined problem

The aim of the study was to determine the shortest possible refining time for the AlSi7Mg alloy. The porosity fraction and mechanical properties were adopted as evaluation criteria. Importantly, the effect of changes in refining time on selected output characteristics was investigated under industrial conditions. The scope of the study included:

1. gas-bubbling refining at different times followed by casting of test specimens,
2. microstructural examination with respect to porosity fraction,
3. measurement of the density index,
4. HB hardness and mechanical-property testing (R_m, $R_{p0.2}$, A).

3.1. Material and research methodology

AlSi7Mg alloy (chemical composition according to EN 1706:2020) was selected for the investigations. It is a standard alloy used for the production of automotive wheels by low-pressure casting (approximately 0.2 MPa, i.e. 2 bar). Refining tests, according to the experimental plan shown in Fig. 1, were carried out in a holding ladle with a capacity of 1.8 Mg (1.6 Mg of liquid metal). An NH_2 mixture (90% N + 10% H_2) was used for refining at a flow rate of approximately 18.5–19.5 $L \cdot min^{-1}$. After refining, samples were taken from the central part of the ladle for metallographic examination, density-index measurement and mechanical-property testing. The previously used refining time was 9 min.

Microstructural images of the samples were acquired using an Olympus GX-51 optical microscope in bright-field mode at 50× magnification. Metallographic specimens prepared according to the recommendations of the Buehler expert system were polished and not etched. For quantitative assessment of porosity, 15 images were acquired in randomly selected fields of view, giving a total analysed area of approximately 70.5 mm². Image binarisation was performed using Otsu's method. Porosity was measured by quantitative metallography using ImageJ image-analysis software. The number and size of pores were determined. The density index was measured hydrostatically (Archimedes' principle) using a laboratory balance by weighing the specimen in air and in distilled water.

HB hardness was measured in accordance with PN-EN ISO 6506-1 using a Zwick ZHF hardness tester under a load of 187.5 kg, with a 2.5 mm diameter steel ball and a test duration of 35 s.

Mechanical properties were determined from a static tensile test at 20°C in accordance with PN-EN ISO 6892-1 using an Instron 3382 testing machine, with a 20:1 ratio and a constant crosshead speed of 4 $mm \cdot min^{-1}$. Eight measurements were performed; the two extreme values were rejected, and the arithmetic mean of the remaining results was calculated and rounded to the nearest integer. The results obtained were compared with the customer requirements.

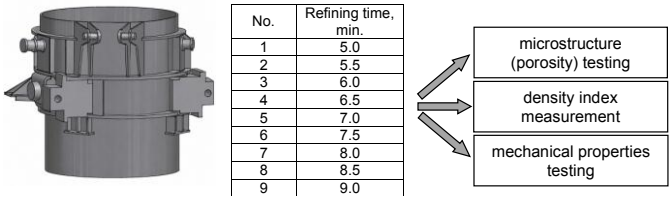

Fig. 1. Test stand and experimental scheme.

4. Results and discussion

4.1. Effect of refining time on porosity and density index of the AlSi7Mg alloy

Microstructural examination showed that samples 1, 6, 7, 8 and 9 were characterised by a high porosity fraction and are therefore not shown. The effect of different refining times on the AlSi7Mg microstructure with respect to porosity for the remaining samples is presented in Fig. 2. Selected quantitative metallography measurements of porosity parameters are shown in Table 1.

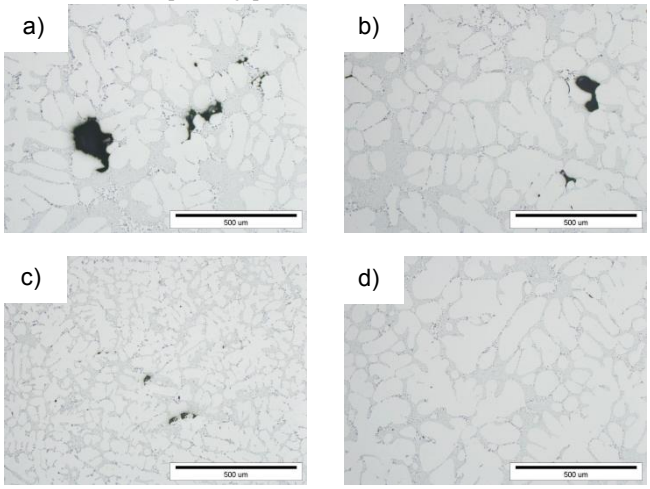

Fig. 2. Microstructure of the AlSi7Mg alloy after different refining times: (a) 5.5 min (sample 2); (b) 6.0 min (sample 3); (c) 6.5 min (sample 4); (d) 7.0 min (sample 5).

Table 1. Results of quantitative metallographic measurements of porosity parameters in the AlSi7Mg alloy.

Sample No.	NH_2 mixture refining time, min.	Number of pores		Pore size	
		Volume fraction of pores, VV, %	Number of pores per 1 mm², NA, mm⁻²	Mean area of planar pore cross-section A, µm²	Mean Feret diameter of planar pore cross-section D, µm
1	5.0	1.230	4.97	3630	73
2	5.5	0.910	2.91	3162	52
3	6.0	0.512	2.14	1476	48
4	6.5	0.132	0.26	2378	42
5	7.0	0.002	0.04	466	30
6	7.5	0.873	1.02	2648	53
7	8.0	2.112	2.89	7681	71
8	8.5	3.160	2.96	11123	95
9	9.0	5.478	4.16	16433	110

Analysis of the quantitative metallography results presented in Table 1 shows that reducing the NH_2-mixture dosing time during refining of the AlSi7Mg alloy to approximately 7 min decreases the porosity fraction. For sample No. 5, the volumetric fraction of pores falls within the range of 0.002–0.132%. The number of pores per 1 mm² ranges from approximately 0.04 to 0.26 mm⁻ ², while the mean diameter of the planar pore cross-section is approximately 30–35 µm. When the refining time exceeds 7 min, the trend begins to reverse and porosity increases, both quantitatively and qualitatively. Taking the above into account, it can be concluded that refining approximately 1.6 Mg of AlSi7Mg alloy should last 7 min. Exceeding this value may increase porosity and consequently the proportion of casting defects in finished products. This is probably caused by the increasing hydrogen content in the alloy (10% H_2), which reduces alloy density [11]. This is consistent with the results reported in [12–14]; however, confirmation of this assumption requires additional investigations.

The results of the density-index measurements for the AlSi7Mg alloy are presented in Fig. 3.

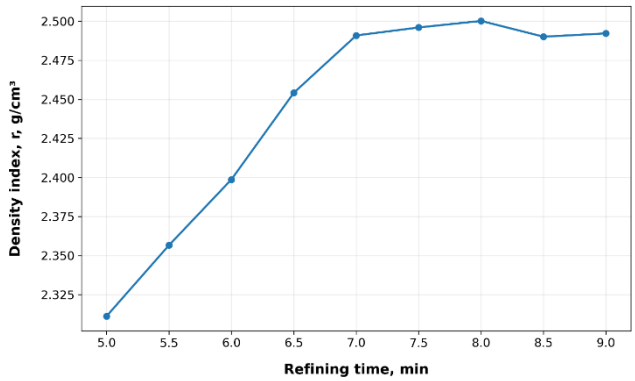

Fig. 3. Density index (ρ) of the AlSi7Mg alloy as a function of refining time.

In addition to porosity and density index, which are key quality criteria determining whether a product is approved for sale, hardness and mechanical properties (R_m, $R_{p0.2}$, A) are also important. Therefore, further investigations focused on the effect of NH_2-mixture dosing time on strength characteristics determined from the static tensile test.

4.2. Effect of refining time on the mechanical properties of the AlSi7Mg alloy

The effect of refining time with the NH2 mixture on hardness and selected mechanical properties of the AlSi7Mg alloy is presented in Fig. 4.

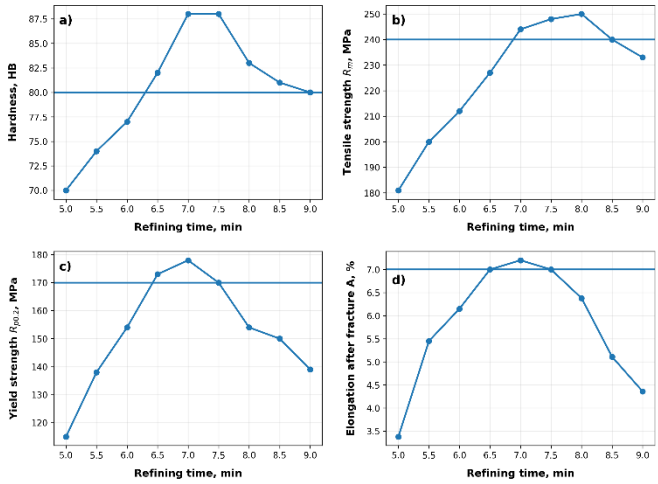

Fig. 4. Effect of NH_2-mixture refining time on: (a) HB hardness; (b) tensile strength R_m; (c) 0.2% proof stress $R_{p0.2}$; (d) elongation after fracture A (the solid line indicates the minimum strength-property values specified by the customer).

The results presented in Fig. 4 show that both hardness and the mechanical properties (R_m, $R_{p0.2}$, A) change in a similar manner. The highest values are observed for samples No. 5 and 6 (NH_2-mixture dosing time of 7–7.5 min). It is worth noting that this refining time results in:

- hardness of approximately 88 HB (minimum required level: 80 HB),
- tensile strength R_m of 244–250 MPa (required level: 240 MPa),
- 0.2% proof stress Rp0.2 of approximately 178 MPa (required level: 170 MPa),
- elongation after fracture A of approximately 7% (meeting the required level).

At shorter refining times, or when the NH_2-mixture dosing time exceeds 7 min, hardness and mechanical properties decrease. It should also be noted that the hardness and mechanical-property results are consistent with the porosity results (Table 1) and the density index (Fig. 3).

5. Conclusion

Although many studies have already been conducted on the effect of refining on selected mechanical properties of aluminium alloys, the subject remains relevant. This is mainly because individual stages of aluminium-alloy melting and casting technologies, particularly pressure casting processes, continue to change, as do the requirements concerning the metallurgical cleanliness of castings, measured for example by the permissible porosity fraction.

The literature also reports numerous studies on the effect of microstructure on specific mechanical properties of aluminium alloys [11]. However, there is still no unequivocal answer as to whether the phase composition, stoichiometry and morphology of structural constituents, or the fraction of gaseous impurities removed by refining, plays the more significant role in determining specific mechanical properties of aluminium alloys.

Regardless of whether views on this issue differ [10–14], refining remains one of the main stages in preparing liquid alloy both for pressure casting and for gravity casting of other non-ferrous metal alloys [15].

Among the parameters of gas-bubbling refining, the density of the AlSi7Mg alloy is influenced mainly by the duration of introduction of the NH_2 mixture (90% N + 10% H_2). Therefore, the effect of refining time on porosity and mechanical properties was investigated for AlSi7Mg alloy used for automotive-wheel castings. It was found that the optimum refining time for AlSi7Mg alloy in a ladle with a capacity of approximately 1.8 Mg (1.6 Mg of liquid metal), with respect to limiting porosity and maintaining mechanical properties, is 7 min. Exceeding this value results in deterioration of porosity, both qualitatively and quantitatively, as well as hardness and selected mechanical properties (R_m, $R_{p0.2}$, A).

Acknowledgements

The authors would like to express their sincere gratitude to the management, in particular Mr Leszek Chowaniec, Director of Superior Industries Production Poland sp. z o.o. in Stalowa Wola, for enabling the research to be carried out and for all assistance in analysing the results.

6. References

1. Agnes S., Yasser Z., Herbert D., Songmene V., Fawzy S., Review Study on the Main Sources of Porosity in Al-Si Cast Alloys. Materials Science and Engineering 22, 2021, https://doi.org/10.1155/2021/1921603.
2. Tiedj N.S., Taylor J.A., Easton M.A., Feeding and distribution of porosity in cast Al-Si alloys as function of alloy composition and modification. Metallurgical and Materials Transactions A43, 2012, 4846-4858, https://doi.org.10.1007/s11661-012-1308-0.
3. Monroe R., Porosity in Castings. AFS Transactions,205, no.4, 2012, 205-245.
4. Elwin L., Rooy E., Mechanisms of porosity formation in aluminum. Modern Casting 82, 1992, 34-36.
5. Samavedam S., Sakri S.B., Hanumantha D.R., Sundarrajan S., Estimation of porosity and shrinkage in a cast eutectic Al-Si alloy. Canadian Metallurgical Quarterly 53, no.1, 2014, 55-64, https://doi.org.10.1179/1879139513Y.0000000097.
6. Tiryakioglu M., Solubility of hydrogen in liquid aluminium: reanalysis of available data. International Journal of Cast Metals Research 32, no.2, 2020, 1-4.
7. Ludvig T., Di Sabatino M., Arnberg L., Influence of oxide additions on the porosity development and mechanical properties of A356 aluminium alloy castings. International Journal of Metalcasting 2012, 41-50.
8. Magnusson T., Arnberg L., Density and solidification shrinkage of hypoeutectic aluminium-silicon alloys. Metallurgical and Materials Transactions A 32, 2001, 2605-13.
9. Santhi S., Sakri S.B., Hanumantha Rao D., Sundarrajan S., Estimation of shrinkage porosity of a cast aluminium alloy. Journal o Mechanical Engineering 2, 2012, 18-24.
10. Samavedam S., Sundarrajan S., Al-Si and Al-Si-Mg Cast Alloys Shrinkage Porosity Estimation. Archives of Foundry Engineering 16(1), 2016, 61-68.
11. Campbell J., Complete Casting Handbook. 2nd Edition. Metal Casting Processes, Metallurgy, Techniques and Design. Elsevier, 2015, www.sciencedirect.com.
12. Anilchandra R., Adamane L.A., Fiorese E., Timelli G., Bonollo F., Influence of injection parameters on the porosity and tensile properties of high-pressure die cast Al-Si alloys: A review. International Journal of Metalcasting 9(1), 2015, 43-53.
13. Awano Y., Morimoto K., Shrinkage morphology of Al-Si casting alloys. Int. Journal Cast Metals Research 17, 2013, 107-114, https://doi.org.10.1179/136404604225014846.
14. Yijie Z., Lordon E., Kun Duo, Shihao W., Zhongyun F., Influence of porosity characteristics on the variability in mechanical properties of high pressure die casting (HPDC) AlSi7MgMn alloys. Journal of Manufacturing Processes 56, 2020, 500-509.
15. Piątkowski J., Crystallization of cast aluminum alloys. Archives of Foundry Engineering Publishing House, Katowice-Gliwice, 2021.